The laser is expensive –
but the electrons are free.

A High Brightness Electron Beam for Free Electron Lasers

Van Oerle, Bartholomeus Mathias

ISBN 90 365 0949 1

NCLR
Nederlands Centrum
voor Laser Research

The research that is described in this thesis was carried out at the Nederlands Centrum voor Laser Research, in close collaboration with the University of Twente in Enschede.

The cover illustration shows the wavelength spectrum of the Twente free-electron laser. The spectrum shows three prominent peaks, that are spaced approximately 9 μm apart. This effect is attributed to the differences in phase velocity between the modes in the waveguide (see section 5.4 and further).

A HIGH BRIGHTNESS ELECTRON BEAM FOR FREE ELECTRON LASERS

PROEFSCHRIFT

ter verkrijging van
de graad van doctor aan de Universiteit Twente,
op gezag van de rector magnificus,
Prof. Dr. F.A. van Vught,
volgens besluit van het College voor Promoties
in het openbaar te verdedigen op
donderdag 19 juni 1997 te 15.00 uur.

door

Bartholomeus Mathias van Oerle
geboren op 22 september 1969
te Leeuwarden

Dit proefschrift is goedgekeurd door de promotor,
Prof. Dr. Ir. W.J. Witteman.

Voor mijn vader,
Bart van Oerle,
volgens zijn eigen onderzoek
de achtentwintigste drager van die naam.

Contents

1. Introduction

The principles of free electron laser (FEL) operation are reviewed. Some differences and similarities between free electron lasers and regular lasers are explored. One-dimensional FEL theory is treated, and it is used to find the electron beam requirements for FEL operation. The contents of this work is presented.

1.1 A bird's eye view of free electron lasers

At the 1993 Free Electron Laser Conference in The Hague, The Netherlands[†] a proposal was presented that discussed the merits of using a high power laser to beam power to artificial satellites in orbit around Earth [1.1]. The authors conclude that, given sufficient power at the correct wavelength, the beaming of laser power is feasible and of tremendous economic interest. The laser in question is a free electron laser (FEL).

In an FEL the kinetic energy of an electron beam is converted into coherent radiation. This radiation is created when electrons move between energy levels in the vacuum. Because these energy levels are quasi-continuous, the FEL radiation is tuneable over virtually the entire electromagnetic spectrum. This property gives FELs a distinct advantage over "regular" lasers, that exploit transitions between discrete electron energy levels in atoms or molecules and usually cannot be tuned over a wide range.

The FEL was conceived by Motz [1.2] in 1951, and thereafter an operational device was constructed by Phillips [1.3]. This first FEL was called a "ubitron" and emitted

[†] A conference that, incidentally, witnessed the introduction of the author of this thesis to the field of free electron lasers.

radiation in the microwave region of the spectrum. Interest in this device was renewed following an analysis by Madey [1.4] and experiments by Elias *et al* [1.5]. Today, FELs have been operated from the microwave region to the deep ultraviolet part of the spectrum [1.6], and there are plans to extend this even further into the X-ray region [1.7].

The coherent radiation in an FEL is generated by letting a relativistic electron beam propagate between two arrays of magnets, spaced a few millimeters apart. Such a device is called an undulator or a wiggler. The magnets in the wiggler are oriented in such a way that the resulting magnetic field is a periodically varying function of position. When the electrons travel through the wiggler, they experience an oscillating Lorentz force which causes them to wiggle around the axis of propagation. Due to this wiggling motion, the electrons emit radiation. In essence, the FEL radiation is Bremsstrahlung created by the acceleration of electrons in the magnetic field of the wiggler [1.4, 1.8].

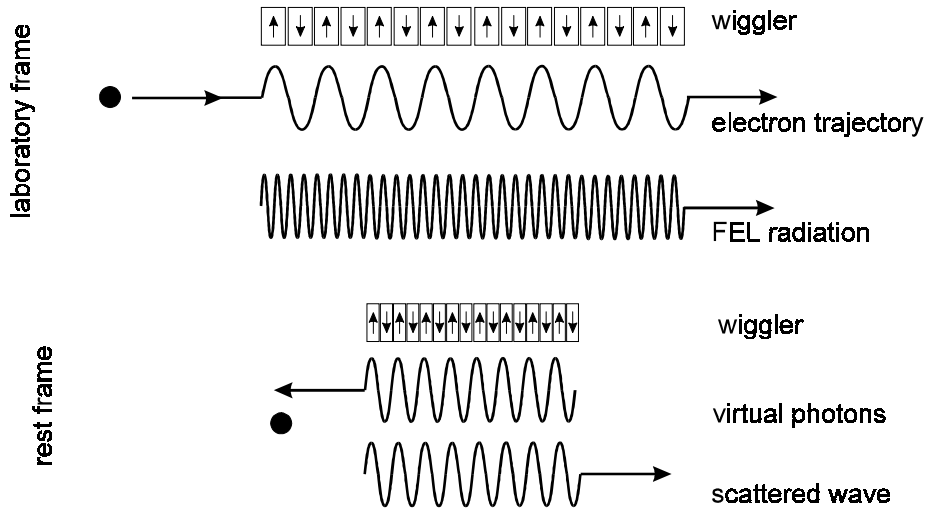

Figure 1.1: Thomson scattering of virtual photons off an electron beam. Top: as seen in the laboratory frame. Bottom: as seen in the electron rest frame.

The FEL radiation wavelength depends on the construction of the wiggler, and on the speed v_z with which the electrons travel through the wiggler. Consider an electron in its rest frame, as shown in Figure 1.1. In this frame, the field of the wiggler is an electromagnetic wave travelling towards the electrons. This causes the electron to oscillate at the frequency

$$\omega_e = \gamma\, k_w v_z \tag{1.1}$$

where we have accounted for the Lorentz contraction of the wiggler wavelength $\lambda_w = 2\pi/k_w$. As usual, γ is the relativistic energy of the electron in terms of its rest mass. The frequency of the FEL radiation ω_r is found by calculating the electron quiver frequency as it appears in the laboratory frame. This involves a relativistic Doppler shift of the quiver frequency:

$$\omega_e = \gamma\left(\omega_r - k_r v_z\right) = \gamma\omega_r\left(1-\frac{v_z}{c}\right) \approx \gamma\omega_r \frac{1}{2\gamma^2} \tag{1.2}$$

Combining this with (1.1) yields the following expression for the FEL radiation wavelength:

$$\lambda_r \approx \frac{\lambda_w}{2\gamma^2} \tag{1.3}$$

The transverse oscillation of the electrons causes a decrease in the longitudinal electron velocity, which leads to longer FEL radiation wavelengths. If we take this effect into account, the expression becomes more accurately:

$$\lambda_r \approx \frac{\lambda_w}{2\gamma^2}\left(1+K^2\right) \tag{1.4}$$

This equation is called the FEL resonance condition. K is called the wiggler parameter and is given by

$$K = \frac{eB_w\lambda_w}{2\pi mc} \tag{1.5}$$

where B_w is the root mean square (r.m.s.) value of the wiggler field. The wiggler parameter[†] is usually $K \approx 1$. In Figure 1.1 the FEL interaction is pictured as the Thomson scattering of a flux of virtual photons off the electron beam. We use the term "virtual photons" because there are obviously no photons associated with the static wiggler field. In the electron rest frame, the energy of the scattered photons is equal to that of the incident photons; but in the laboratory frame, the scattered photons have a much larger energy than the incident photons. This increase in energy is on the expense of the electron energy. Hence the electron beam is the source of energy in an FEL. The Thomson scattering process is highly anisotropic. The scattered radiation is confined to a cone with angle $\theta \approx 1/\gamma^2$ around the propagation direction of the electrons.

The equation (1.4) shows the fundamental tunability of an FEL. For example: electrons with energy $E = 6$ MeV have $\gamma = 12.7$. When these electrons propagate through a wiggler with $K = 1$ and $\lambda_w = 25$ mm, the created laser radiation has a wavelength $\lambda_r = 154$ μm. By changing the electron energy from 6 MeV to 3 MeV, the laser wavelength can be increased to 531 μm. An FEL is tuned by changing either the

[†] Some authors use the wiggler parameter to distinguish between an undulator and a wiggler. According to [1.10], an undulator is a wiggler with $K \leq 1$. Based on this definition, our wiggler is an undulator, but since this definition does not seem to be generally accepted we will just use the general term "wiggler".

energy of the electron beam, or by changing the value of the wiggler parameter K. The latter is usually accomplished by changing the value of the magnetic field B_w.

Another advantage of FELs over conventional lasers is their potential scalability to high power. In general, laser systems are not very efficient and only a fraction of the pumping power is converted into coherent radiation. The rest is dissipated as heat in the laser medium. The medium must therefore be cooled to avoid thermal damage. In conventional systems this is accomplished by either flowing or water-cooling the medium. FELs do not have this problem, since the waste energy of the electrons is carried away at almost the speed of light. Moreover, experiments [1.9] have shown that up to 70 % of this waste energy can be recovered. These properties make FELs ideal instruments for non-linear spectroscopy, material research, medicine, fusion research and many other fields.

1.2 One-dimensional FEL theory

In this section, some results from one-dimensional FEL theory will be reviewed. The treatment here is intended to give the reader some feel for the FEL physics, and it is therefore not rigorous. More in-depth analyses can be found in e.g. [1.10], [1.11] or [1.12]. Let us start by examining the electron motion in a planar wiggler. The behaviour of an electron in a vector potential $\vec{A}$ is governed by the relativistic Newton-Lorentz force equations:

$$\frac{d\left(\gamma\vec{\beta}\right)}{dt} = -\frac{e}{m}\left(\frac{1}{c}\frac{\partial\vec{A}}{\partial t} - \vec{\beta}\times\vec{\nabla}\times\vec{A}\right) = \frac{e}{mc}\left(\vec{E} + \vec{v}\times\vec{B}\right) \tag{1.6}$$

$$\frac{\partial\gamma}{\partial t} = -\frac{e}{mc}\vec{\beta}\cdot\frac{\partial\vec{A}}{\partial t} = \frac{e}{mc^2}\vec{v}\cdot\vec{E} \tag{1.7}$$

where as usual $\vec{\beta}$ is the relativistic vector parameter $\vec{\beta} = \vec{v}/c$. The vector potential is a combination of the wiggler and the radiation vector potentials: $\vec{A} = \vec{A}_w + \vec{A}_r$. In most practical situations, the amplitude of the wiggler field is much larger than that of the radiation field, such that to zeroth order the electron motion is determined by the wiggler vector potential. In an ideal, planar wiggler this vector potential is given by:

$$\vec{A}_w = \hat{\mathbf{x}}\sqrt{2}A_w\sin\left(k_w z\right) \tag{1.8}$$

The wiggler field causes the electrons to oscillate in a plane perpendicular to the wiggler magnetic field. The transverse velocity of the electrons in these oscillations is small compared to the longitudinal velocity.

Since the wiggler field does not depend on time, the expression (1.7) yields zero. Thus in the absence of a radiation field, the electron energy remains constant. This is what one would expect, since there can be no energy transfer between an electron and the

static magnetic field of the wiggler. However, because there is energy conservation, the modulation of the transverse electron velocity leads to a modulation of the longitudinal velocity. In a reference frame moving with the centre of mass of the electron motion, the electron moves in a figure of eight around the wiggler axis.

Due to the oscillatory motion of the electron around the wiggler axis, a co-propagating radiation wave is generated. Since every electron injected into the wiggler generates such a wave, the radiation created by a randomly distributed ensemble of electrons is incoherent. This radiation is analogous to the spontaneous emission in regular laser systems. The homogeneous linewidth of the FEL spontaneous emission depends on the number of periods in the wiggler N_w:

$$\left(\frac{\delta\omega}{\omega}\right)_{\text{hom}} = \frac{1}{2N_w} \tag{1.9}$$

Let us now consider the dynamics of a single electron in the combined wiggler and radiation waves. The vector potential of the radiation wave is polarised in the direction of the wiggler vector potential:

$$\vec{A}_r = \hat{\mathbf{x}}\sqrt{2}A_r \cos\left(k_r z - \omega_r t + \varphi_r\right) \tag{1.10}$$

The combined wave travels at a lower velocity than the radiation wave, and is therefore called the ponderomotive wave. The phase of the electron in the ponderomotive wave is called the ponderomotive phase. It is given by

$$\zeta = k_w z + k_r z - \omega_r t + \varphi_r \tag{1.11}$$

When the velocity of the electron exactly matches that of the ponderomotive wave, the ponderomotive phase is constant and the electron experiences a constant ponderomotive potential. In that case, the interaction between the electron and the radiation field can be very strong. The condition for constant ponderomotive phase is found by setting the time derivative of (1.11) equal to zero. This yields

$$\frac{\lambda_w}{v_z} = \frac{\lambda_w + \lambda_r}{c} \tag{1.12}$$

Using the relation $\beta_z \approx K/\gamma$ and under the assumption that $\beta \approx 1$, the above expression is equivalent to the FEL resonance condition (1.4). By substituting the ponderomotive potential $\vec{A} = \vec{A}_w + \vec{A}_r$ in (1.7) and integrating it over a wiggler period, we find [1.10]:

$$\frac{d\gamma}{dt} = -\frac{eK}{\gamma mc} E\left[J_0(\xi) - J_1(\xi)\right]\sin(\zeta) \tag{1.13}$$

where E is the electric field component of the FEL radiation, J_0 and J_1 are the Bessel functions of the zeroth and first order, and

$$\xi = \frac{K^2}{2\left(1+K^2\right)} \tag{1.14}$$

Due to the interaction between the electrons and the radiation field, the electron energy is no longer constant. The interaction depends on the ponderomotive phase of the electron. If the phase $\pi < \zeta < 2\pi$, the electron gains energy on the expense of the radiation wave; if however the phase $0 < \zeta < \pi$ then the electron loses energy and the radiation wave is amplified.

Consider again a randomly distributed ensemble of electrons, propagating down the wiggler. Half of the electrons have $\pi < \zeta < 2\pi$ and attenuate the radiation wave, the other half has $0 < \zeta < \pi$ and amplifies the wave. The net result is that initially the amplitude of the radiation wave is unaffected. However, as a result of the electron acceleration and deceleration, the electrons tend to concentrate in certain regions of the ponderomotive wave. If the radiation wave would be constant, the electrons would bunch at a position $\zeta = \pi$; but since the phase of the radiation wave also evolves, the result of the interaction is a bunching of the electrons at a phase $\zeta < \pi$ where they continue to amplify the radiation wave in a coherent way.

The evolution of the phase can be understood as follows. As any other laser, an FEL starts from noise that is generated by spontaneous emission. Since this noise is incoherent, an electron moves in a collection of random-phased ponderomotive waves. The phase of an electron in any particular ponderomotive wave depends on the phase of the radiation wave. Only those waves for which the ponderomotive phase $\zeta < \pi$ will be amplified; the other waves will either pass unaffected (if $\zeta = \pi$) or they will be attenuated and disappear. Thus we see that in the surviving ponderomotive potential, the electrons are bunched at a phase $\zeta < \pi$.

An important parameter in a laser system is the small signal gain. The FEL small signal gain is calculated by integrating the expression (1.13) over the length of the wiggler, and averaging it over the electrons. This yields [1.10]:

$$G = 2\pi \frac{K^2 e L_w^2 N_w}{\varepsilon_0 \gamma^3 m c^3} \frac{J_e}{A_o} \left[J_0\left(\xi\right) - J_1\left(\xi\right) \right] g(\alpha) \tag{1.15}$$

where L_w is the length of the wiggler, A_o the area of the optical beam and J_e the electron beam current. The parameter α is called the detuning parameter and is a measure of the radiation wavelength relative to the resonance wavelength, as given by (1.4). It is defined as:

$$\alpha = 2\pi N_w \left(\frac{k_r - k}{k_r} \right) \tag{1.16}$$

The function $g(\alpha)$ is the gain function, defined by the formula:

$$g(\alpha) = -2 \frac{d}{d\alpha} \left(\frac{\sin(\alpha/2)}{\alpha} \right)^2 = \frac{2 - 2\cos(\alpha) + 2\alpha \sin(\alpha)}{\alpha^3} \tag{1.17}$$

The FEL gain curve is odd symmetric, as is seen in Figure 1.2. A radiation wave with exactly the resonant wavelength $\lambda = \lambda_r$ passes unaffected through the wiggler. If the wavelength λ is slightly smaller than the resonant wavelength λ_r the wave is attenuated, and it is amplified only when λ is slightly larger than λ_r. The gain is a maximum when the detuning parameter $\alpha_{max} = 2.6$. This corresponds to a wavelength

$$\lambda = \frac{2.6 + 2\pi N_w}{2\pi N_W} \lambda_r \tag{1.18}$$

In a 50-period wiggler, the wavelength at which there is maximum gain is 0.8 % larger than the resonant wavelength.

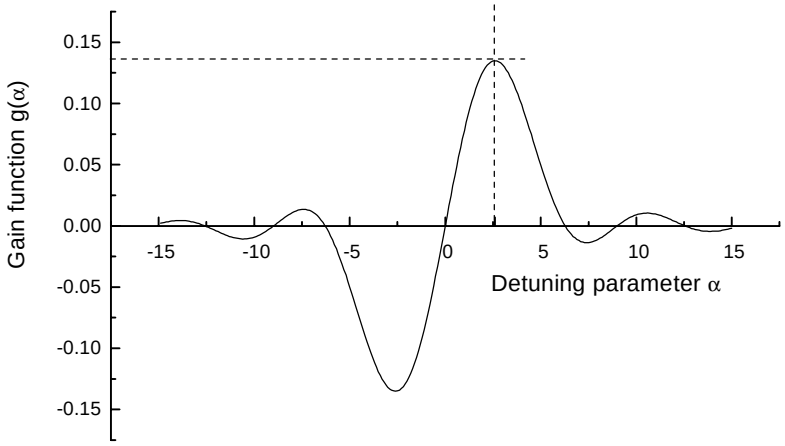

Figure 1.2: The small signal gain function. The dotted lines indicate the maximum value at $\alpha_{max} = 2.6$, for which $g(\alpha) = 0.135$.

1.3 Effect of the electron beam quality

1.3.1 Energy spread, emittance and peak current

The efficiency of the FEL interaction depends, among other things, on the quality of the electron beam. The most important electron beam parameters are the energy spread,

the emittance and the peak current. To obtain sufficient gain, the inhomogeneous line broadening caused by the energy spread of the electron beam should be smaller than the homogeneous line broadening determined by the number of wiggler periods. In theory there is also a contribution to the inhomogeneous line broadening due to the transverse electron velocity distribution, but in practice this contribution can be neglected. From the resonance condition (1.4) follows for the inhomogeneous line broadening:

$$\left(\frac{\delta\omega}{\omega}\right)_{inh} \approx 2\frac{\delta\gamma}{\gamma} \tag{1.19}$$

The homogeneous line broadening is given by (1.9). By comparing (1.9) with (1.19) we find the requirement for the energy spread:

$$\frac{\delta\gamma}{\gamma} < \frac{1}{4N_w} \tag{1.20}$$

For a wiggler with 50 periods this implies an energy spread $\delta\gamma/\gamma < 0.5$ %.

The interaction between the electron beam and the laser radiation is most profitable if the optical beam is a Gaussian-Hermite mode with a more or less constant diameter inside the wiggler. This is accomplished by choosing the wiggler length L_w equal to twice the confocal length of the optical beam. Then the 1/e radius of the optical beam waist in the resonator is:

$$w_o = \sqrt{\frac{\lambda_r L_w}{2\pi}} = \sqrt{\frac{\lambda_r N_w \lambda_w}{2\pi}} \tag{1.21}$$

The size of the electron beam in the wiggler depends on the normalised emittance ε_n of the beam. The emittance is a measure of the electron beam quality and is analogous to the M^2- number used to measure the quality of a Gaussian-Hermite optical beam (as will be explained in Chapter 4). In the wiggler, the 1/e radius of the electron beam is given by [1.10]:

$$w_e = \frac{1}{2\pi}\frac{1}{2\sqrt{\ln 2}}\sqrt{\varepsilon_n \lambda_w} \tag{1.22}$$

For sufficient small wavelength, the radius of the optical beam becomes smaller than that of the electron beam, and only a part of the electron beam current is used. Since this decreases the small signal gain of the FEL, this situation should be avoided and the emittance should be small enough to allow sufficient focusing of the electron beam in the wiggler. The required emittance is found by solving the equation $w_e < w_o$ for ε_n:

$$\varepsilon_n < 8\pi \ln(2) N_w \lambda_r \tag{1.23}$$

To achieve laser operation, the small signal gain must be larger than the round-trip losses in the cavity. Solving (1.15) for J_e and using the resonance condition (1.4), we find for the required beam current density:

$$J_{req} = \frac{G_{\min}}{G_0 N_w^3 \lambda_r^{3/2} \lambda_w^{1/2}} \tag{1.24}$$

where $G_{\min}$ is the minimum gain required to achieve lasing and

$$G_0 = \frac{2\pi K^2 e}{\varepsilon_0 m c^3} \left(\frac{1+K^2}{2} \right)^{3/2} \frac{1}{\left(J_0(\xi) - J_1(\xi) \right)^2 g(\alpha_{\max})} \tag{1.25}$$

As long as the radius of the electron beam is smaller than the radius of the optical beam, the total required beam current is $I_{\text{req}} = \pi w_o^2 J_{req}$. However, as soon as condition (1.23) is invalid, i.e. when $w_e > w_o$, the required beam current increases to $I_{\text{req}} = \pi w_e^2 J_{req}$. Consider for example a situation in which $G_{\min} = 0.5$, $\lambda_w = 25$ mm, $K = 1$ and $N_w = 50$. The minimum required current is plotted in Figure 1.3 as a function of resonant wavelength. The figure shows that the required current increases with decreasing wavelength; moreover, the increase is most dramatic for an electron beam with a large emittance.

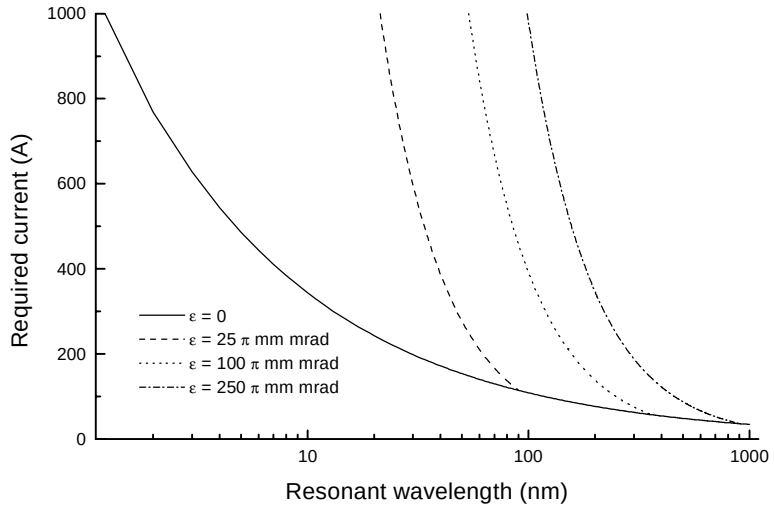

Figure 1.3: The minimum current requirement as a function of resonant wavelength, for several values of the electron beam emittance.

The significance of Figure 1.3 is that in order to construct a short wavelength FEL, an electron beam with a low emittance and a high current is a requirement [1.13].

However, the emittance of the electron beam is largely determined by the Coulomb interaction between the electrons in the beam; in other words: an electron beam with a higher peak current will tend to have a higher emittance. Thus the emittance requirement (1.23) dictates strict requirements for the electron source. For FELs operating in the (far) infrared the emittance requirement is not that strict. However, a high current is still desirable since the small signal gain is proportional to the electron beam current.

An important parameter describing a high current, low emittance electron beam is the normalised brightness, which is defined as

$$B_n = \frac{2I}{\varepsilon_n^2} \tag{1.26}$$

where I is the electron beam peak current and ε_n the normalised emittance.

1.3.2 Choice of the electron source

The most frequently used method to create an electron beam is by means of a thermionic cathode. This consists of a material (for instance LaB_6) that is heated up to a high temperature ($T_{cat} \approx 1100\ ^oC$). At that temperature the kinetic energy of electrons in the material has increased to a point where they can escape from the material. The thermionic cathode is a very simple and reliable electron source, with an average operational lifetime well over 10,000 hours.

The main disadvantages of the thermionic cathode are the relative low current and the long electron pulse length. The beam current is typically $I \approx 1$ A during 10 μs. To circumvent these problems, a thermionic electron source is often used in combination with a buncher. This is a device that compresses the length of the electron pulse while keeping the charge in the pulse constant, thus increasing the peak current of the electron beam. Unfortunately, a buncher usually decreases the transverse quality of the electron beam.

Gun type	*I (A)*	*ε_n (π mm mrad)*	*B_n (10^{10} A/ m^2 rad^2)*
RF + PC [1.14]	130	18	8.13
DC + PC [1.15, 1.16]	100	54	0.69
DC + TC [1.17]	12	30	0.27
DC + TC + buncher [1.18]	75	80	0.23

Table 1.1: Electron beam parameters for some types of electron guns. RF: radio-frequency linear accelerator; DC: electrostatic accelerator, PC: photo cathode; TC: thermionic cathode.

An electron beam with a high peak current can be created directly by illuminating a photo cathode with a high intensity laser pulse. Down to a picosecond time scale, the

shape of the electron pulse is equal to the shape of the laser pulse[†] . However, due to the Coulomb interaction between the electrons, such a high density electron bunch will soon increase in both length and transverse width, leading to an increase in emittance and a decrease in peak current. It is therefore essential to accelerate the short electron bunches as fast as possible. For this purpose, an electrostatic accelerator is not suitable due to its limited acceleration field. However, in a radio-frequency linear accelerator an electron can be accelerated more rapidly.

In Table 1.1 some typical values for I, ε_n and B_n are given for several electron beam sources. This table clearly indicates that the electron beam with the lowest emittance, highest peak current and lowest energy spread to date, is created by a photo cathode driven linear accelerator.

1.4 Scope of the present work

This thesis describes work done at the free electron laser TEU-FEL, a collaboration between Twente University, Eindhoven University and the Nederlands Centrum voor Laser Research. In the first stage of the TEU-FEL project, the FEL is driven by a 6 MeV electron beam, which is created in a radio-frequency linear accelerator by illuminating a photo cathode with either the second or fourth harmonic of a Nd:YLF drive laser.

Chapter 2 describes the laser system that is used to illuminate the photo cathode. In particular, attention is focused on the amplification of the drive laser pulses and the frequency doubling and quadrupling schemes that have been designed. Measurements of the laser pulse length at the fundamental wavelength, and at the second harmonic have been performed.

The performance of the photo cathodes in the vacuum of the accelerator is of great importance to the prolonged performance of the FEL. The ideal photo cathode would have a high efficiency and an infinite lifetime under operating conditions. Unfortunately, most high-efficient photo cathode materials tend to degrade when they are used in a linear accelerator. Several types of photo cathodes, each with characteristic behaviour under operating conditions and a specific spectral sensitivity, have been prepared and used in our linear accelerator. As part of this research, we have discovered two new photo cathode materials with very interesting properties. Our experiences with the photo cathodes are described in Chapter 3.

The strength of the FEL interaction depends on the current and the quality of the electron beam. In Chapter 4, the emittance is defined as a measure of the electron beam quality and several methods to measure this parameter are explained and demonstrated. The results from different techniques are compared and combined with current measurements to give a value for the brightness of the electron beam. These results are compared to those obtained with other high brightness electron beam sources.

[†] The cathode has a small response time in which the photoexcited electrons travel from the bulk material to the surface, an effect that will be clarified in Chapter 3. The response time is on the order of picoseconds for semiconducting photo cathodes, and femtoseconds for metals.

The final chapter is devoted to a number of FEL experiments that have been performed at TEU-FEL. The first lasing experiments will be treated, and the effect of the laser resonator modes on the FEL wavelength will be explained. These modes cause a shift in the resonant wavelength, as is demonstrated experimentally with measurements of the FEL radiation wavelength.

1.5 References

1.1 H.E. Bennet, J.D.G. Rather, E.E. Montgomery IV, "Free-electron laser power beaming to satellites at China Lake, California", Nucl. Instr. and Meth. A **341** (1994) pp124 – 131.

1.2 H. Motz, "Applications of the radiation from fast electron beams", J. Appl. Phys. **22**, p527 (1951).

1.3 R.M. Phillips, "The ubitron, a high-power travelling-wave tube based on a periodic beam interaction in unloaded waveguide", IRE Trans. Electron. Dev. **7**, p231 (1960).

1.4 J.M.J. Madey, "Stimulated emission of Bremsstrahlung in a periodic magnetic field", J. Appl. Phys, **42**, 5 (1971) pp1906 – 1913.

1.5 L.R. Elias, W.M. Fairbank, J.M.J. Madey, H.A. Schwettman and T.I. Smith, "Observation of stimulated emission of radiation by relativistic electrons in a spatially periodic transverse magnetic field", Phys. Rev. Letters **36**, p717 (1976).

1.6 P.G. O'Shea *et al*, "Demonstration of ultraviolet lasing with a low energy electron beam", Nucl. Instr. and Meth. A **341** (1994) pp7 – 11.

1.7 K.J. Kim, "UV/X-ray free electron lasers through high gain single pass amplifiers: basic principles and key issues", Nucl. Instr. and Meth. A **358** (1995) pp31 – 35.

1.8 T.C. Marshall, *Free-Electron Lasers*, MacMillan Publishing Company, New York (1985), ISBN 0-02-948620-3.

1.9 D.W. Feldman, "Recent results from the Los Alamos Free Electron Laser", IEEE J. Quant. Electron. **QE-23**, p1476 (1987)

1.10 C.E. Brau, *Free-Electron Lasers*, Academic Press, Inc, San Diego (1990), ISBN 0-12-126000-3.

1.11 R. Bonifacio, F. Casagrande, G. Cerchioni, L. De Salvo Souza, P. Pierini, "One-dimensional theory of a free-electron laser amplifier: steady state and superradiance", in *High gain, high power Free-Electron Lasers*, Ed. R. Bonifacio, L. De Salvo Souza and C. Pellegrini, North Holland, Amsterdam (1989), ISBN 0-444-87395-3.

1.12 E.H. Haselhoff, *Aspects of a Compton Free-Electron Laser*, thesis, Universiteit Twente (1993), ISBN 90-9006096-0.

1.13 W.J. Witteman, G.J. Ernst, J.W.J. Verschuur, B.M. van Oerle, D. Bisero, "Free-electron laser with high brightness photo-injector", Laser Physics **7**, 1 (1997) pp150 – 154.

1.14 R.L. Sheffield, E.R. Gray, J.S. Fraser, "The Los Alamos photoinjector program", Nucl. Instr. and Meth. A **272** (1988) pp222 – 226.

1.15 C. Travier, “CANDELA photoinjector status”, Proc. VIIIth Symp. on High Current Photoemission, Milan 19-20 September (1996).
1.16 C. Travier, G. Devanz, B. Leblond, B. Mouton, “Experimental characterization of Candela photoinjector”, submitted to Nucl. Instr. and Meth. A.
1.17 M. Caplan, M. Valentini, C. van der Geer, W. Urbanus, “Design and characterization of the DC acceleration and transport system required for the 1 MW free electron maser experiment”, Nucl. Instr. and Meth A **375** (1995) pp91 – 94.
1.18 R. Chaput *et al*, “Operation of the CLIO accelerator”, Nucl. Instr. and Meth. A **331** (1993) pp267 – 271.

2. Drive Laser Requirements

The set-up of the TEU-FEL drive laser is described. Special attention is focused on the amplification of the macropulse in two double-pass and one single-pass amplifiers. The experimental results are compared with the results of a numerical model. The basic principles of second and fourth harmonic generation processes, and their effect on the laser pulse length are discussed. Autocorrelation and streak camera measurements of the latter are presented.

2.1 Overview of the drive laser system

The drive laser is used to illuminate a photo cathode in the first cell of the linear accelerator. This creates a short electron bunch, that is accelerated and used in the FEL experiment. The properties of the drive laser are crucial for the FEL performance: The length of the laser pulse influences the electron bunch length, the energy of the pulse affects the maximum charge of the bunch and the stability of the laser power determines the stability of the FEL output.

A complete schematic of the drive laser [2.1, 2.2] is shown in Figure 2.1. At the heart of the drive laser set-up for TEU-FEL is a mode-locked Nd:YLF laser, that emits a train of pulses at a wavelength of 1053 nm. These pulses have a duration of 60 ps at a repetition rate of 81.25 MHz. The individual pulses will from now on be called micropulses. The average power of the laser beam is 3 W, which yields 50 nJ per micropulse.

For free electron laser experiments, a shorter duration of the micropulse is preferred. Also, the spectral sensitivity of the photo cathode materials must be considered. Most photo cathode materials are more sensitive in the visible and ultraviolet region of the spectrum (see also Chapter 3). Some kind of frequency conversion process is required

to change the colour of the laser beam, but due to the limited efficiency of such a process this will decrease the energy available to illuminate the cathode.

In a nutshell: the pulses of the mode-locked Nd:YLF laser are too long, have the wrong colour and have not enough energy. Therefore, they will be compressed, amplified and frequency-doubled or quadrupled.

First, the laser beam is injected into a fibre-grating pulse compressor, which compresses the micropulses to a duration of 20 ps [2.3]. The pulse compression depends on the length of the fibre. The entrance surface of the fibre is very susceptible to thermal damage. This limits the average power on the fibre to 500 mW, yielding an intensity of 266 MW/cm^2 at the entrance of the fibre. The overall transmission of the pulse compressor in our set-up is approximately 40 %, leaving an energy of 2.7 nJ per micropulse at the exit. The micropulse duration at the exit can be measured using an autocorrelator.

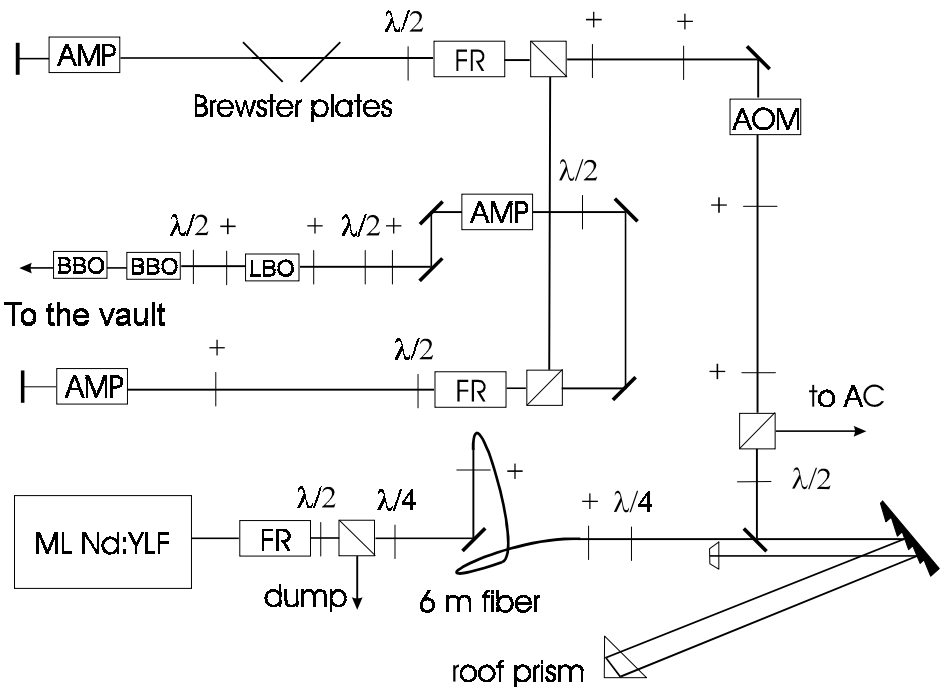

Figure 2.1: A schematic of the TEU-FEL drive laser system. FR - Faraday rotator; AC - autocorrelator; AMP - Nd:YLF amplifier. After frequency quadrupling, the beam is transported over 40 m to the vault, where the photo injector is positioned.

The laser beam is then focused into a travelling-wave acousto-optic modulator (AOM). This is a $LiNbO_3$ crystal, in which an acoustic wave is generated by applying a radio-frequent voltage over the crystal. The acoustic wave is a grating by which the laser beam is deflected. By changing the modulation depth of the grating (i.e., by changing the power of the applied radio-frequent signal), the intensity of the deflected beam can be varied. In this type of modulator, a maximum of 65 % of the energy of the incident beam can be deflected into the first order. The AOM is used to slice out a 15 μs long pulse train, called the macropulse. We require a maximum repetition rate of the

macropulses of 10 Hz. At this point, the energy in a micropulse is 1.7 nJ; the maximum energy in a macropulse is 2.0 μJ. The macropulse is amplified in two double pass, and one single pass flash lamp pumped Nd:YLF amplifiers. Faraday rotators and cube polarisers are used to separate the incoming from the returning beam in the double pass amplifiers. After amplification, the energy of a micropulse is maximum 30 μJ. The pulses are frequency doubled in a non-critically phase matched lithium triborate (LBO) crystal. The crystal is kept in an oven at 134 °C. The second frequency doubling process, from 527 nm to 263 nm, takes place in two β-barium borate (BBO) crystals.

After this step, the laser beam is transported to the vault, some 40 m away, where the free electron laser is positioned. The beam is apodized by an iris, after which it is imaged onto the photo cathode using a 1000 mm biconvex lens and a $3 \times 3 \times 5$ mm right angle prism. The beam size on the photo cathode can be varied between 1.0 mm and 10.0 mm.

2.2 Amplification of the macropulse

When amplifying a laser macropulse, the output pulse shape will generally not be identical to the input pulse shape, due to depletion of the gain medium [2.4, 2.5, 2.6]. However, for the free electron laser application an amplified macropulse with a flat temporal shape and the highest possible output power is preferred.

A frequently used method to obtain a flat output pulse is to choose the timing of the macropulse with respect to the flash lamp pump pulse, in such a way that the depletion of the inversion caused by the passage of a micropulse is equal to the production of inversion in between two micropulses. Then the inversion is constant during the macropulse, and each micropulse experiences the same gain. Hence a flat input macropulse yields a flat output macropulse. This scheme will be referred to as flat-in-flat-out (FIFO). In this scenario, the macropulse must be injected into the gain medium at a time when the inversion is not yet at its maximum, which means we are not using the maximum available power in the amplifiers.

This means that the FIFO method is not very efficient. We have experimented with a more efficient method, in which the macropulse is injected into the gain medium at the time when the inversion is at its maximum. However, due to the depletion of the inversion by the earlier micropulses, the micropulses at the end of the pulse will experience less gain, resulting in a non-flat output pulse. This can be circumvented by decreasing the energy of the micropulses towards the beginning of the macropulse so that more inversion is available for the last part of the macropulse. Proper shaping of the incoming pulse results in a flat output macropulse. This scheme will be referred to as pulse shaping (PS).

The efficiency of both amplification schemes is limited by the amount of energy available in the unamplified macropulse. In a FIFO experiment, the efficiency will be maximum if the macropulse is injected when the pump pulse is at its maximum. Whether this timing coincides with the timing required to get a flat output pulse, depends on the initial energy of the macropulse. In our case, we need to inject the macropulse after the maximum in the pump pulse, which decreases the efficiency of

the amplifier. In contrast, in a PS experiment the injection time of the macropulse is fixed. The amplifier efficiency will increase with increasing energy in the macropulse which is limited experimentally to 1.7 nJ per micropulse.

2.2.1 Aspects of pulse amplification

The effective area A_{eff} for amplification of the beam is

$$A_{eff} = \frac{\pi w^2}{2}. \tag{2.1}$$

The energy density of the *i*-th micropulse will be denoted by E_{in}^{i}. If the depletion of the amplifying medium during the transit of a micropulse is assumed to be small, the output energy of the pulse is given by

$$E_{out}^{i} = G^{i} E_{in}^{i} \tag{2.2}$$

where G^{i} is the small signal gain experienced by the *i*-th micropulse. The small signal gain depends exponentially on the inversion N^{i} and the interaction cross section σ:

$$G^{i} = e^{\sigma N^{i}}. \tag{2.3}$$

The inversion in an amplifier can be calculated iteratively by using:

$$N^{i+1} - N^{i} = -\frac{\left(E_{out}^{i} - E_{in}^{i}\right)}{h\nu} + \left(P(t) - \frac{N^{i}}{\tau}\right)\delta t, \tag{2.4}$$

where $h\nu$ is the energy of a photon and τ the relaxation time constant of the medium. The first term on the right hand side takes into account the gain depletion caused by the transit of the micropulse. It is followed by the contribution of the pump pulse and a spontaneous decay term. The time δt is the time between two micropulses. The initial inversion in the amplifier depends on the injection time of the macropulse, and is calculated by integrating

$$\frac{dN}{dt} = P(t) - \frac{N}{\tau} \tag{2.5}$$

from the start of the pump pulse to the injection time of the macropulse. The pump pulse $P(t)$ is proportional to the power dissipated in the flash lamp, which is given by the product of the current pulse through, and the voltage pulse over the flash lamp. Both pulses are shown in Figure 2.2.

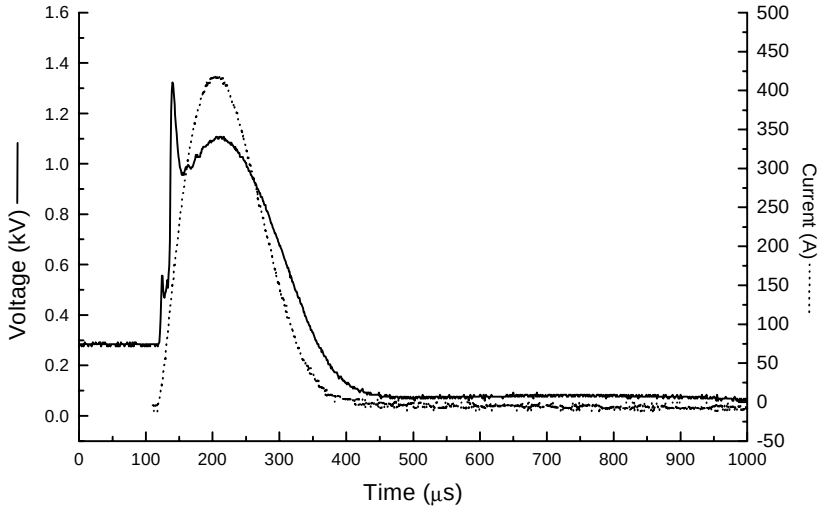

Figure 2.2: The current through the flash lamp and the voltage over the flash lamp as a function of time.

In our experimental situation, the spatial distance between the micropulses is approximately 3.7 meters. This means that in a double-pass amplifier a micropulse can propagate back and forth through the amplifying medium, before the next micropulse arrives. Due to the transit of a micropulse, the inversion in the medium will changes by the amount $\left(E_{in}^{i} - E_{out}^{i}\right)/h\nu$. If the effect of the pump pulse and the spontaneous emission are neglected, the gain for the second pass of the micropulse is $G^{i} e^{\left(1-G^{i}\right)E_{in}^{i}/E_{s}}$. Here $E_s = h\nu/\sigma$ is called the saturation energy fluence. After two passes through the medium, the energy of the pulse is given by:

$$E_{out}^{i} = E_{in}^{i}\left(G^{i}\right)^{2} e^{\left(1-G^{i}\right)E_{in}^{i}/E_{s}} \tag{2.6}$$

Equation (2.6) shows that the gain of a double pass amplifier will decrease with increasing pulse energy, a mechanism that is known as gain saturation. The output energy of a micropulse E_{out}^{i} is calculated from E_{in}^{i} using equation (2.2) for a single pass amplifier, and equation (2.6) for a double pass amplifier.

A number of experimentally determined parameters enter into the model: first of all the small signal gain of each amplifier, second the transport losses from one amplifier to the other, third the 1/e diameter of the laser beam at the entrance of the amplifiers, and finally the relaxation time constant of the inversion. Table 2.1 gives an overview of these parameters and their values.

Since the inversion is depleted by the transit of the macropulse, the amplification of a single micropulse depends on the energy of the preceding micropulses. In a system consisting of three amplifiers, the analytical expressions describing the amplification

of a macropulse can become very complex. Also, due to the exponential gain of the unsaturated laser pulse, one can expect a large sensitivity to the experimentally determined parameters. This will decrease the reliability of the theoretical model. For that reason, it is therefore worthwhile to investigate experimentally the required conditions for the pulse amplification scheme that is described above.

amplifier	*small signal gain*	*transport loss (%)*	*beam size (mm)*	*relaxation time (μs)*
first	20	40	0.7	400
second	10	40	0.8	480
third	10	10	1.1	480

Table 2.1: Experimentally determined system parameters.

2.2.2 Feed forward loop to control the output macropulse shape

To control the shape of the macropulse after amplification, a feed forward loop is constructed (see Figure 2.3). This loop checks the output macropulse shape against a reference pulse shape and changes the input macropulse shape accordingly. This process is repeated until the desired macropulse shape has been reached.

The shape of the input macropulse is controlled by an arbitrary waveform generator (AWG), that accepts waveforms from the computer control program. A reflected part of the output signal is monitored by a FND-100Q photo diode. This signal is displayed on a Tektronix TDS640 oscilloscope, which can be read using a personal computer. A LabView program is used to read the successive waveforms, and calculate the steering waveforms for the AWG.

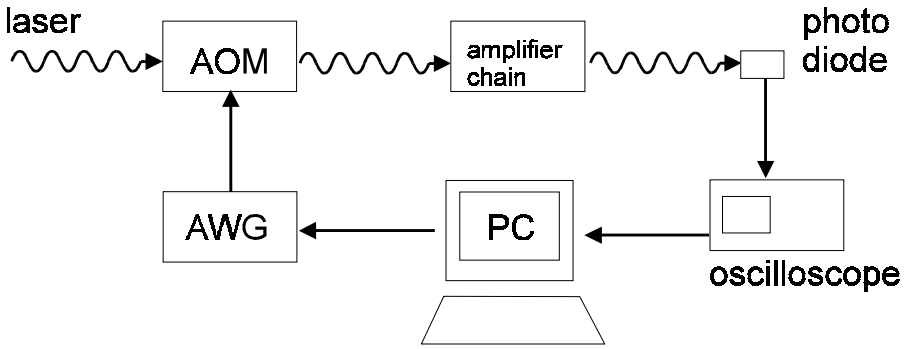

Figure 2.3: A schematic of the feed forward loop used to control the shape of the output pulse.

A flat output pulse is obtained within 30 iterations, which in total requires about 1 minute operating time. The results are shown in Figure 2.4 where also the FIFO experiments are displayed. These experiments were performed using three amplifiers at maximal gain. The amplitude jitter on the output macropulse is 1.5 %, which is within the experimental error equal to the amplitude jitter on the unamplified micropulses.

The total output energy is 70 % higher than was obtained with a flat input pulse, and yet the corresponding total input energy is 50 % lower.

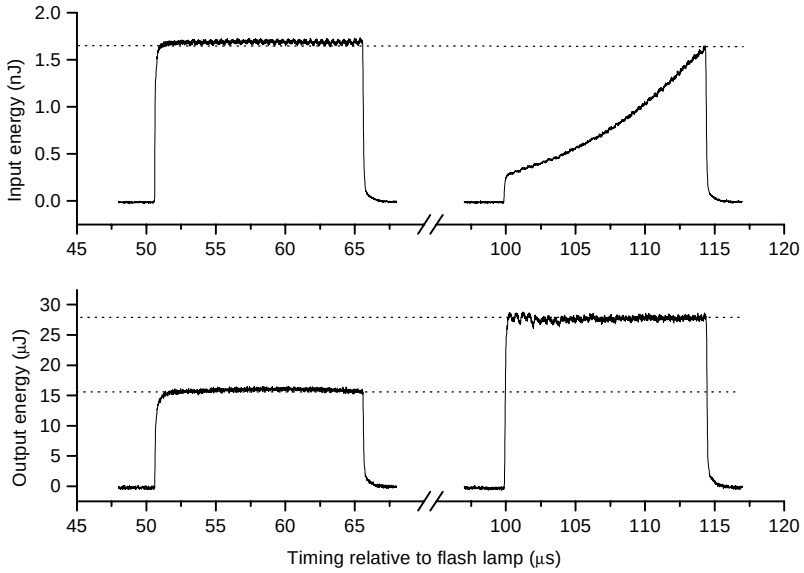

Figure 2.4: Results of the feed forward control loop after 30 iterations are shown on the right. For comparison, the results of the FIFO experiments are shown on the left. The top two graphs indicate input pulse shapes, the bottom two graphs represent output pulse shapes.

Figure 2.5 compares the output energy of a macropulse that was calculated according to the computational model, with values that were found experimentally. In this case, a flat input pulse 15 μs long with 1.5 nJ energy per micropulse was injected into the amplifier chain, and the timing of this pulse with respect to the amplifier pump pulse was varied. Only the energy of the amplified macropulse was measured; the shape of the macropulse was disregarded. To test the validity of the model, two situations were considered: one in which only two double pass amplifiers were used, and one in which also the third (single pass) amplifier was used. The dashed line corresponds to the first case, and the dotted curve to the latter case.

Let us now look at the shape of the macropulse. Consider first the amplification of a macropulse in two double pass amplifiers (Figure 2.6). The solid line in the left graph is a polynomial fit to the experimentally found pulse shape, that yields a flat macropulse after amplification. The solid line in the right graph is a linear fit to the experimentally found, flat macropulse. We can now use our model to make a prediction of the output macropulse shape, given the experimentally found input pulse shape. The result is the dashed graph on the right. This macropulse has a peak-to-peak amplitude fluctuation of 5 %, and an average energy per micropulse of 5.9 μJ. In the experiment, a value of 6.1 μJ per micropulse was measured. It is also possible to do the reverse, i.e. calculate the input macropulse shape that is required to yield a flat

output macropulse with a given energy. The result of this calculation is the dashed graph on the left in Figure 2.6.

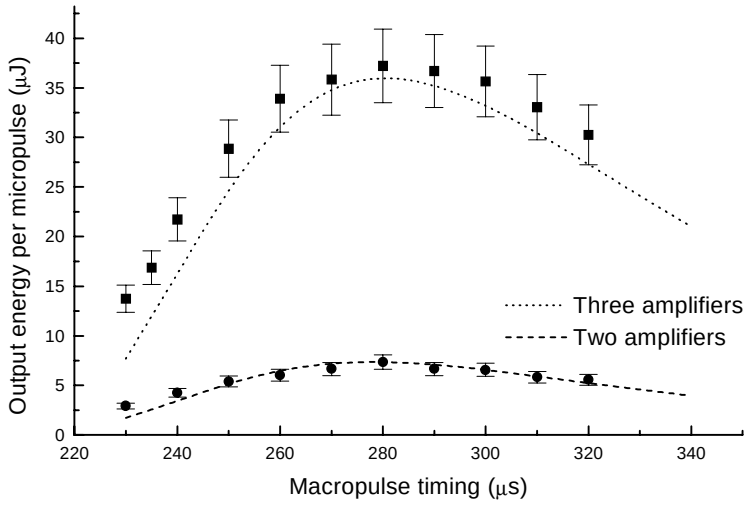

Figure 2.5: Measurements of the energy of an amplified flat input pulse, as a function of the time relative to the pump pulse. Results obtained with two amplifiers (circles) and three amplifiers (squares) are shown. The curves represent calculations done with the rate equation model.

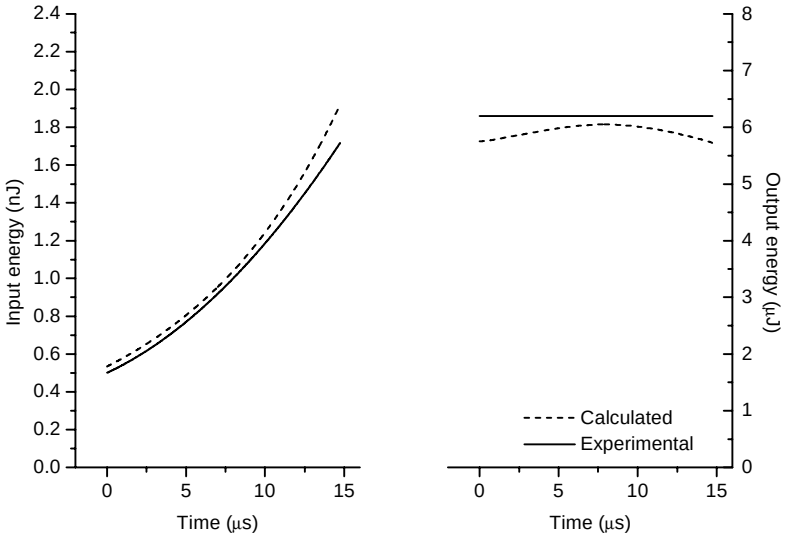

Figure 2.6: The shape of the macropulse in an experiment using only two double pass amplifiers. The solid lines represent the experiment, the dashed lines simulated pulse shapes.

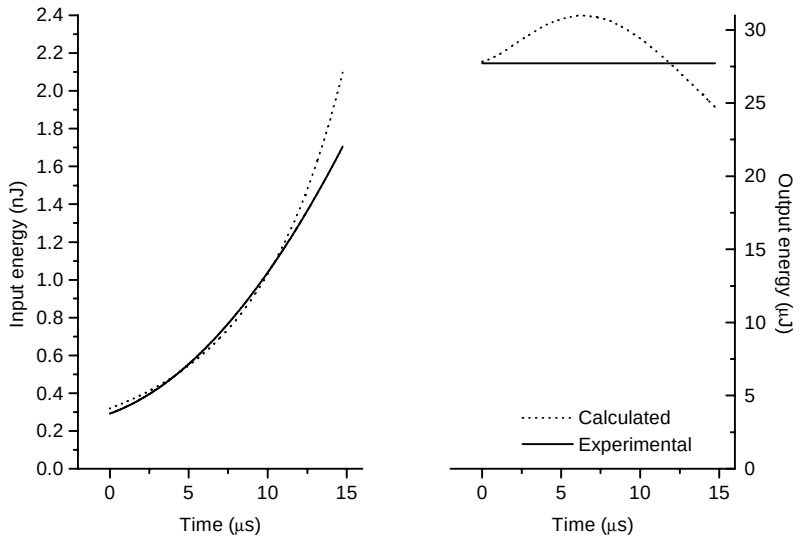

Figure 2.7: The shape of the macropulse when using two double pass and one single pass amplifiers at maximal gain. The solid curves represent experimental data; the dotted curves represent the simulations.

Now the third (single pass) amplifier will be included into the model.. The result is the dotted graph on the right in Figure 2.7. This macropulse shape has an average energy per micropulse of 29 μJ, and a peak-to-peak amplitude fluctuation of 20 %. The dotted curve on the left is obtained in a similar way, demanding a flat output pulse after amplification in three amplifiers.

2.3 Second and fourth harmonic generation

2.3.1 Physical origin of harmonic generation

To explain some of the physics of second harmonic generation (SHG), the arguments of Boyd [2.8] will be followed. In a non-linear optical crystal, the dielectric polarization of the medium is a non-linear function of the electric field *E*:

$$\begin{aligned}\tilde{P}(t) &= \chi^{(1)}\tilde{E}(t) + \chi^{(2)}\tilde{E}^{2}(t) + \chi^{(3)}\tilde{E}^{3}(t) + \ldots \\ &= \tilde{P}^{(1)}(t) + \tilde{P}^{(2)}(t) + \tilde{P}^{(3)}(t) + \ldots\end{aligned} \tag{2.7}$$

The coefficients $\chi^{(i)}$ are called the (non-)linear susceptibilities of the medium. Consider a laser field that is present in such a medium. The field can be described as:

$$\tilde{E}(t) = Ee^{-i\omega t} + c.c. \tag{2.8}$$

Then the second order non-linear polarization will be

$$\tilde{P}^{(2)}(t) = 2\chi^{(2)} EE^{*} + (\chi^{(2)} E^{2} e^{-2i\omega t} + c.c.) \tag{2.9}$$

which generates a laser beam with a double frequency in the medium. This beam will co-propagate with the beam at the fundamental frequency.

Since the second order polarization is proportional to the square of the incident electric field, the intensity of the second harmonic scales with the square of the intensity of the fundamental, and consequently the efficiency of the SHG process scales linear with the intensity of the fundamental beam. A side-effect is the temporal narrowing of laser pulses. Consider a gaussian laser pulse at the fundamental frequency ω, and a duration τ:

$$\tilde{E}(t) = E_{\max} e^{-t^2/2\tau^2} e^{i\omega t} \tag{2.10}$$

which in a non-linear medium will generate a second order polarization:

$$\tilde{P}^{(2)}(t) \propto \chi^{(2)} E_{\max}^{2} e^{-t^2/\tau^2} e^{2i\omega t} \tag{2.11}$$

Because the intensity of the gaussian laser pulse is higher in the centre of the pulse, the conversion efficiency at that point will be higher than on the wings. This results in a second harmonic pulse that is a factor of $\sqrt{2}$ shorter than the fundamental pulse.

Most media are dispersive, which means that the phase velocity of the second harmonic beam is in general different from the phase velocity of the fundamental beam. This leads to a back-conversion of the second harmonic power to the fundamental power. This is the reason that the first SHG experiments, carried out in the late 1960s, were not very efficient.

2.3.2 Birefringence, walk-off and phase matching

In many crystals, the phase velocity of an optical beam depends on the polarization of its electric field. The physical origin of this effect is the structural anisotropy of the crystal, that expresses itself in the direction dependence of the dielectric constant. As a result, the magnitude of the displaced electric field depends on the direction of the incident field:

$$\begin{aligned} D_x &= \varepsilon_x E_x; \\ D_y &= \varepsilon_y E_y; \\ D_z &= \varepsilon_z E_z; \end{aligned} \tag{2.12}$$

The axes *x*, *y* and *z* are called principle axes, and the vector $\varepsilon = (\varepsilon_x, \varepsilon_y, \varepsilon_z)$ is called the principle dielectric vector. In general, the dielectric vector depends on the frequency.

Suppose an optical beam propagates along the principle axis *z*. When its electric field is in the *x* direction, this will experience a dielectric constant ε_x. Therefore, the phase velocity of the wave will be $\sqrt{\mu\varepsilon_x}$. Likewise, if the electric field is in the *y* direction, the phase velocity will be $\sqrt{\mu\varepsilon_y}$. This effect is called birefringence, and the crystal is said to be birefringent. Judging by their dielectric vectors, crystals can be divided into three groups:

1. $\varepsilon_x = \varepsilon_y = \varepsilon_z$. The isotropic crystals. These crystals are centrosymmetric and cannot be used for harmonic generation.
2. $\varepsilon_x = \varepsilon_y \neq \varepsilon_z$. Uniaxial crystals. Examples are: potassium dihydrogen phosphate (KDP), β-barium borate (BBO), and lithium iodate ($LiIO_3$).
3. $\varepsilon_x \neq \varepsilon_y \neq \varepsilon_z$. Biaxial crystals. Examples are lithium triborate (LBO) and potassium titanyl phosphate (KTP).

The dielectric constant defines a surface in *x*, *y*, *z* space, called the index ellipsoid:

$$\frac{x^2}{n_x^2} + \frac{y^2}{n_y^2} + \frac{z^2}{n_z^2} = 1 \tag{2.13}$$

where $n_i = 1/\sqrt{\varepsilon_i}$. For biaxial crystals, this surface is a true ellipsoid. For uniaxial crystals, it degenerates into a spheroid (or ellipsoid of revolution) and for isotropic crystals it degenerates further into a sphere. An ellipsoid has two circular sections passing through its centre. An optical beam propagating perpendicular to such a section, will experience the same refractive index for both polarizations of the electric field. The directions normal to the circular sections are called the optical axes. In uniaxial crystals, the circular sections overlap and hence these crystals have only one optical axis.

In uniaxial crystals, an ordinary beam is an optical beam with its electric field perpendicular to the plane formed by the propagation direction and the optical axis. An extraordinary beam has its electric field in the same plane as the propagation vector and the optical axis. If an optical beam propagates along an optical axis, the extraordinary and ordinary beam are interchangeable.

Due to the tensor character of the dielectric constant, the displaced electric field is in general not in the same direction as the electric field. As a result, the wavevector $\vec{k} = \vec{D} \times \vec{H}$ will usually not be in the same direction as the Poynting vector $\vec{S} = \vec{E} \times \vec{H}$. In words, the energy of the beam will propagate at an angle to the propagation direction of the wavefront. This effect is called walk-off. It can be shown [2.9] that the Poynting vector is always perpendicular to the surface of the index ellipsoid, at the point where it is intersected by the wave vector. Figure 2.8 gives an example of walk-off in a uniaxial crystal. The walk-off angle depends on the propagation direction of the wavefront.

The walk-off effect was already described by Christiaan Huygens in 1690, who observed a beam of sunlight passing through what he called Islandic crystal ($CaCO_3$) [2.10]. Even though the incident beam was perpendicular to the crystal surface, Huygens observed that it split in two beams that propagated at an angle of 6.6°. One beam was called the ordinary ray, and the other was called the extraordinary ray since it did not seem to obey Snell's law of refraction.

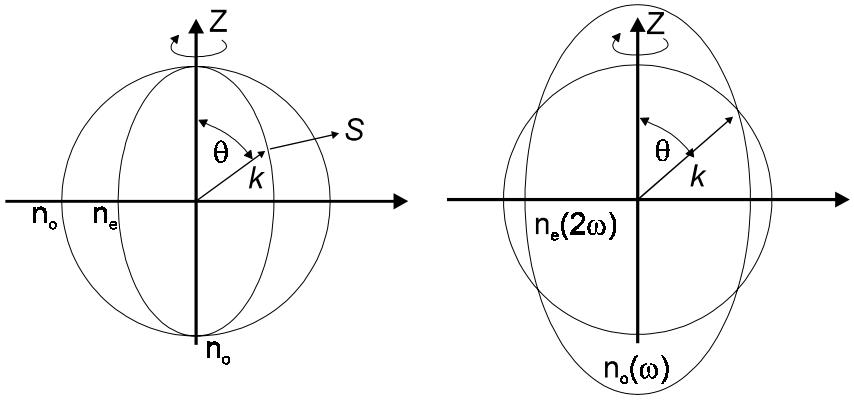

Figure 2.8 : Example of walk-off (on the left) and angle tuning phase matching (on the right) in negative uniaxial crystals.

The birefringence of non-linear optical crystals can be used to obtain a higher efficiency of the second harmonic generation. The crystal is orientated such, that the refractive index of the extraordinary beam at the fundamental wavelength $n_e(2\omega)$, is equal to the refractive index of the ordinary beam at the second harmonic wavelength $n_o(\omega)$. Thus the wavevectors of the fundamental and second harmonic are equal, resulting in a constant phase between the beams. This method is called phase matching angle tuning. In practice, perfect phase matching is never obtained and in long crystals backconversion from the second harmonic to the fundamental is observed.

A special case arises when the angle between the propagation direction and the optical axis is exactly 0° or 90°. Then, the wavevector and Poynting vector are parallel, eliminating walk-off. This situation is called non-critical phase matching (NCPM). In for example LBO, temperature tuning is used to match the refractive index of the ordinary wave on the refractive index of the extraordinary wave.

2.3.3 Walk-off compensation

In long birefringent crystals that cannot be non-critically phase-matched, the walk-off between the fundamental and the harmonic beam will effectively stop the conversion process. For instance, in a BBO crystal cut for frequency-doubling at 527 nm, the angle between the second harmonic and the fundamental Poynting vector is 4.9°. In a crystal with a length of 7 mm, the fundamental and second harmonic beams will have diverged a distance of 0.6 mm at the end of the crystal.

Although the Poynting vectors of ordinary and extraordinary rays are not parallel, the wave vectors of the fundamental and second harmonic beams are. Thus the beams,

having passed through the non-linear optical crystal, will propagate parallel in free space. This allows for the possibility of walk-off compensation. We can position a second BBO crystal immediately after the first one, which is rotated 180° on the propagation axis with respect to the first crystal. The walk-off in this crystal is now such that the second harmonic beam moves back towards the fundamental beam, thus increasing the spatial overlap of the beams and the efficiency of the conversion process (see Figure 2.9). The crystals will be called "crossed" since the optical axes are not parallel.

If the second crystal is aligned in the same way as the first one, that is with the same orientation of the principle axes, then the fundamental and second harmonic beam will diverge even further in the second crystal. The two crystals will be called "parallel" since the optical axes are parallel.

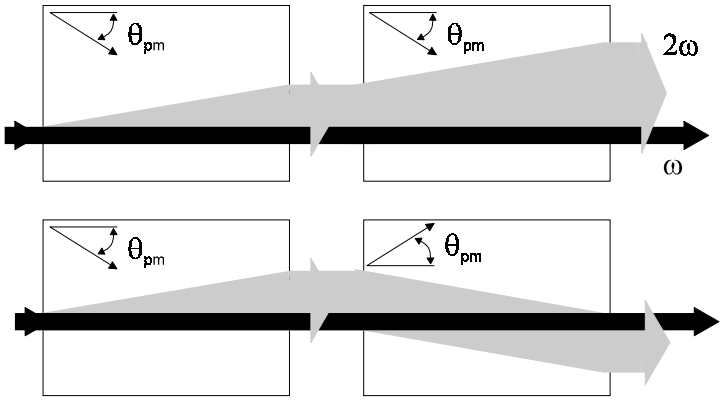

Figure 2.9: Walk-off compensation in negative uniaxial crystals. Top: parallel crystals; below: crossed crystals. The angle θ_{pm} is the phase matching angle..

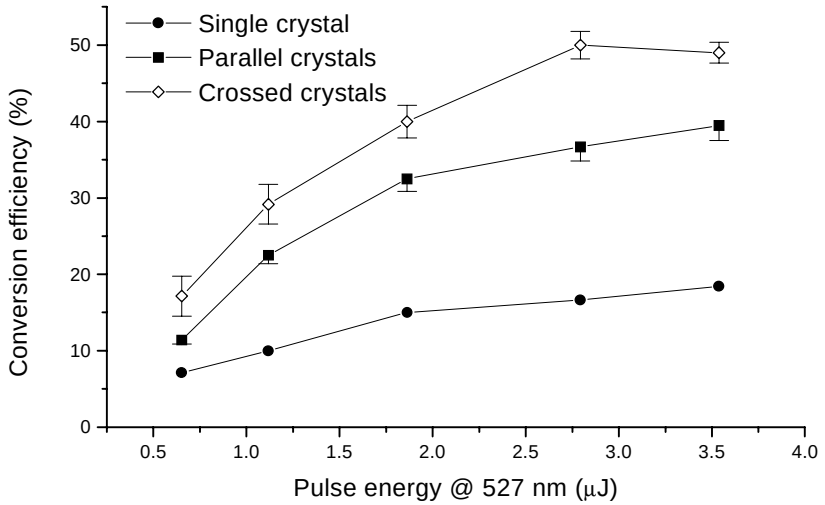

Figure 2.10: The efficiency of the fourth harmonic generation for three different BBO configurations.

The efficiency of the fourth harmonic generation process as a function of the pulse energy in the visible is given in Figure 2.10. A conversion efficiency of 20 % from the second to the fourth harmonic has been obtained, using a single BBO crystal. Two parallel BBO crystals yield a maximum conversion efficiency of 40 %. When the crystals are crossed, the maximum conversion efficiency is 50 %, which is more than twice the efficiency obtained in a single crystal.

An additional bonus of the walk-off compensation scheme is an improved beam quality in the ultraviolet. Figure 2.11 shows the beam profiles of the fourth harmonic beam in the far field. The left figure shows the profile when only one crystal is used in the conversion. When two crystals in parallel are used, the resulting beam profile consists of two spots that overlap partially, as one would expect from Figure 2.9. When the BBO crystals are crossed, the resulting beam profile is much better than was obtained with parallel crystals.

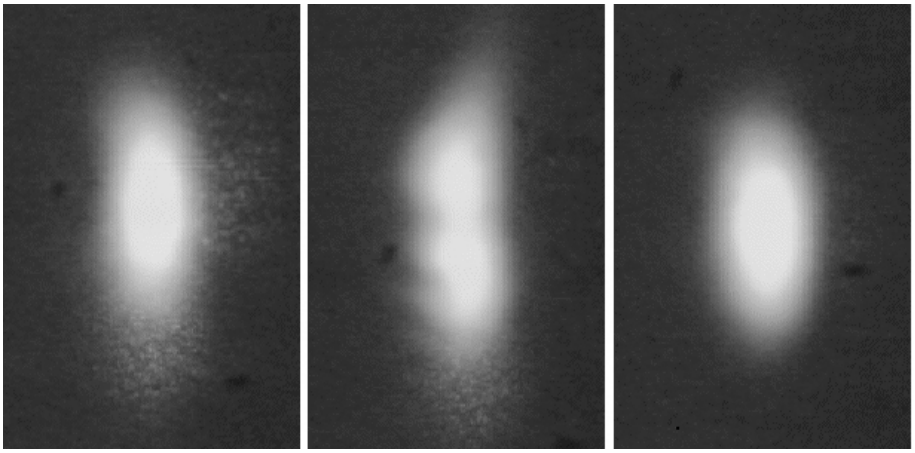

Figure 2.11: Beam profiles corresponding to three BBO configurations. Left: single BBO; centre: parallel BBOs; right: crossed BBOs.

2.4 The length of the micropulse

2.4.1 Autocorrelation measurements

We will now set out to determine experimentally the duration of the drive laser pulses at different places in the system [2.12]. The duration of the micropulses before the AOM, thus before the macropulses are formed, has been measured with a commercially available autocorrelator (Inrad model 514B). The operating principle of this autocorrelator is as follows: The incoming beam is split into two equal parts, each following a different path in the autocorrelator. The two parts are recombined in a $LiIO_3$ crystal, where they generate the autocorrelation signal (see also Figure 2.12).

In each optical path a rotating block is present. In the equilibrium position the optical lengths of both paths are equal. For a certain angular deviation from the equilibrium position, a delay respectively advance of $\tau/2$ is introduced into each path. Because of the relatively low rotation frequency of the delay blocks (15 Hz) it takes about 2 ms to

vary the delay over 20 ps, which means that each measurement requires at least a 2 ms long train of pulses.

The above mentioned technique can not be used directly to measure the pulse duration after the amplifiers or after frequency doubling, because the macropulses are only 15 μs long, which is about 2 orders of magnitude too short. On the other hand, a single pulse autocorrelation-technique as originally developed by Wyatt and Marinero [2.13] also cannot be used because a much larger energy per micropulse (at least 50 μJ per micropulse) is required to obtain a reasonable signal to noise ratio.

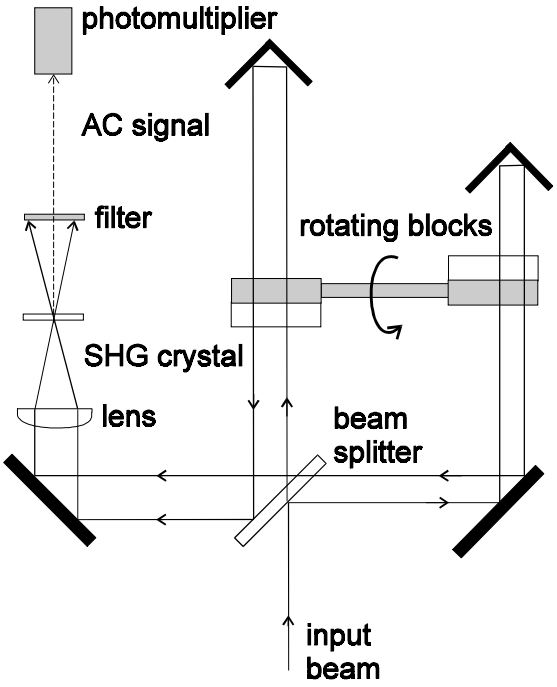

Figure 2.12: The set-up of the Inrad autocorrelator. This autocorrelator is used to measure the pulse length of the infrared and visible micropulses.

A usual technique to measure autocorrelation traces of bursts of pulses is to vary the delay between the two pulses manually and then doing an autocorrelation measurement while keeping the delay fixed in time. However, if the bursts of pulses come regularly with a fixed repetition frequency f_b a very simple autocorrelation technique can be used with the help of the Inrad autocorrelator. In this autocorrelator an autocorrelation measurement is performed at each rotation of the delay blocks. A trigger pulse is generated at the start of the autocorrelation trace.

Suppose the rotation frequency of the blocks is f_{rot} . The phase ϕ between the rotation frequency and the macropulse repetition frequency is given by:

$$\phi = \left(f_{rot} - n f_b \right) t \tag{2.14}$$

where t is the time at which the phase is determined. Suppose the rotation frequency f_{rot} equals f_b or is the n-th subharmonic of f_b, then each autocorrelation measurement is

done at the same phase difference ϕ between the two frequencies, and thus at the same optical delay time. However, if f_b is not exactly equal to f_{rot} or a subharmonic of f_{rot}, then each measurement is performed at a different phase ϕ, and thus at different optical delay time between the two pulses.

Each micropulse will yield one point in the autocorrelation trace. A macropulse consists of 1200 micropulses, and will therefore yield 1200 points in the trace. These points are indistinguishable due to the finite bandwidth of the photomultiplier and the electronics. The resulting point in the autocorrelation trace is an average over one macropulse. Using a storage oscilloscope, a complete autocorrelation trace can be measured. As can be seen from equation (2.14), $d\phi/dt$ can be adjusted by changing f_b. Hence the time required to measure a complete autocorrelation trace can be chosen by changing f_b. In our experiment f_{rot} is a fixed frequency and equals 15 Hz, and f_b can be set to a value close to 7.5 Hz.

The pulse duration has been measured at three positions in the beam line: Once before slicing out the macropulse, once again after amplification of the macropulse and finally after frequency-doubling the macropulse. To measure the autocorrelation pulse duration in the visible, the $LiIO_3$-crystal was replaced by a 1 mm BBO-crystal.

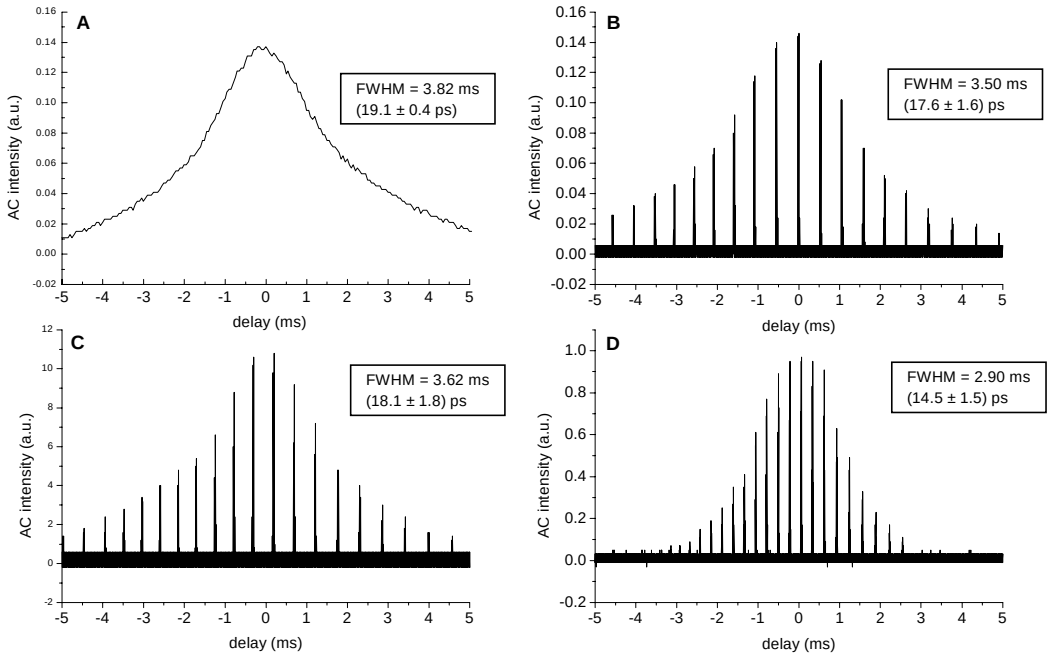

Figure 2.13: Autocorrelation measurements on the visible and infrared micropulses. A) AC trace from an infinitely long pulse train, measured before the macropulse was sliced out. B) AC trace measured after the macropulses have been sliced out. C) AC trace measured after the macropulses have been amplified. D) AC trace of the pulses after the amplified macropulses have been frequency-doubled.

The results of these measurements can be found in Figure 2.13. These autocorrelation traces are Lorentzian curves, which are deconvolved into Lorentzian pulse shapes. The conventional autocorrelation trace (Figure 2.13a) yields a pulse FWHM of (19.1 ± 0.4) ps. This may be compared to the trace in Figure 2.13b, which was measured after the macropulse had been sliced out. The FWHM of these pulses were (17.6 ± 1.6) ps, which is within the margin of error equal to the result obtained with the conventional autocorrelation method. Further measurements yield FWHM = (18.1 ± 1.8) ps after the macropulse has been sliced out and amplified (Figure 2.13c), and FWHM = (14.5 ± 1.5) ps after frequency-doubling the amplified macropulse (Figure 2.13d).

The trace in Figure 2.13a, measured before the macropulse was sliced out of the continuous pulse train, appears to be a continuous trace. This is because the bandwidth of the electronics behind the photomultiplier is too small to resolve the individual micropulses. The peaks that are shown in the other traces in Figure 2.13 originate from the 15 μs long macropulses. The delay difference between these macropulses can be adjusted by changing $d\phi/dt$ according to equation (2.14). Since the autocorrelation curve is composed of several macropulses, it is essential that the fluctuation in the amplitude of these macropulses is small. In our case this fluctuation is less than 1 %.

The autocorrelation traces shown in Figure 2.13 were not measured simultaneously. Because the autocorrelation curves have been measured at several positions in the beam line, the autocorrelator had to be repositioned and realigned between measurements. It is possible that during this realignment, the duration of the Nd:YLF laser pulse has changed, due to cavity detuning caused by temperature effects. This may account for the observed variations in the pulse duration.

2.4.2 Streak camera measurements

A major disadvantage of the autocorrelation function as a measure of the micropulse duration, is that the autocorrelation function does not give any information on the shape of the micropulse. Furthermore, the autocorrelation measurements presented in this chapter are multi-shot measurements, which implies that from the presented data we can not draw any conclusions regarding the pulse-to-pulse fluctuations in the pulse duration.

To increase our confidence in the pulse length measurements, the length of the micropulse was also measured using a Hamamatsu streak camera (model C1587-01). The operating principle of a streak camera is as follows: A laser pulse is incident on a photo cathode, where it creates a short electron bunch that is accelerated in a static electric field. The electron bunch then travels between two deflection plates, on which an alternating voltage is applied. The deflection angle of the electrons depends on the arrival time of the electrons between the plates. Thus the temporal profile of the electron bunch is converted to a spatial profile, which is made visible on a phosphorous screen.

In Figure 2.14 the streak profile of an uncompressed infrared micropulse is shown, together with the streak profile of a frequency-doubled pulse. The infrared pulse has a

duration of 60.0 ps and the frequency-doubled pulse a duration of 42.2 ps. Once more the ratio of these durations is $\sqrt{2}$. For comparison, the autocorrelation trace of the uncompressed infrared pulse is shown on the left; this also yields a pulse duration of 60.0 ps.

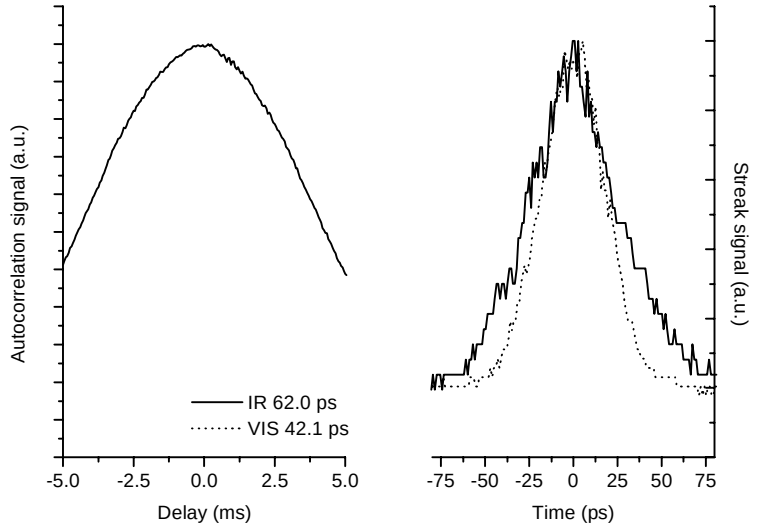

Figure 2.14: Streak camera measurements of the infrared and visible micropulse are shown in the right graph. The left graph shows the corresponding autocorrelation trace of the infrared micropulse.

2.5 Conclusions

The amplifier chain can be modelled using a rate-equation approach, including saturation, pump pulse and relaxation effects. Both the calculated energy, and the shape of the macropulse after amplification in two double pass amplifiers are in good agreement with the experimentally obtained results.

We have successfully constructed and operated a feed forward loop that controls the shape of a macropulse after amplification in a Nd:YLF amplifier chain. We were able to obtain a flat macropulse with an amplitude jitter of 1.5 % in 15 μs. The control loop routinely yields a flat output pulse after 30 iterations, which is equal to one minute operating time. The macropulse output energy obtained in this way is 70 % more than was obtained in a FIFO amplification scheme, even though the macropulse input energy was 50 % less.

A technique to measure the autocorrelation traces of bursts of picosecond pulses has been successfully demonstrated. This technique has been used to measure the duration of pulses in short pulse trains, of intermediate energy (in the order of 1 μJ per micropulse). The results acquired by this method are comparable to those obtained by more conventional techniques.

According to the autocorrelation measurements presented in this chapter, the pulses that are generated by our MOPA system are of the correct duration to be used in an FEL experiment. The predicted increase in pulse duration due to the amplification of the macropulse was well within the experimental margin of error, and hence it was not observed. There is good agreement between the autocorrelation measurements and the measurements with the streak camera.

2.6 References

2.1 R.F.X.A.M. Mols and G.J. Ernst, "Performance of a MOPA laser system for photo cathode research", Nucl. Instr. and Meth. A. **341** (1994) pp481 – 483.

2.2 B.M. van Oerle, D. Bisero, G.J. Ernst, J.W.J. Verschuur and W.J. Witteman, "A Nd: YLF laser system for the illumination of Cs_2Te photo cathodes in the TEU-FEL accelerator", accepted for publication in Nucl. Instr. and Meth. A.

2.3 R.F.X.A.M. Mols and G.J. Ernst, "Parametric study of the behaviour of group velocity dispersion in optical pulse compression", Opt. Comm. **94** (1992) pp509 – 514.

2.4 A.E. Siegman, *Lasers*, University Science Books, Mill Valley (1986), ISBN 0-935702-11-5.

2.5 L. M. Frantz and J.S. Nodvik, "Theory of pulse propagation in a laser amplifier", J. Appl. Phys. **34,** 8 (1963) pp2346 - 2349.

2.6 A.Y. Cabezas, G.L. McAllister W.K. Ng, "Gain saturation in Neodinium:Glass laser amplifiers", J. Appl. Phys **38**, 9 (1967) pp3487 – 3491.

2.7 B.M. van Oerle, D. Bisero, G.J. Ernst, J.W.J. Verschuur and W.J. Witteman, "Optimization of the power and control of the shape of amplified trains of laser pulses", accepted for publication in Appl. Opt.

2.8 R.W. Boyd, *Nonlinear Optics*, Academic Press Inc, San Diego (1992), ISBN 0-12-12680-2.

2.9 M. Born and E. Wolf, *Principles of Optics*, Pergamon Press, Oxford (1980), ISBN 0-08-026481-6.

2.10 C. Huygens, *Traité de la Lumière* , Van der Aa, Leiden (1690). The original French version has been reprinted together with the Dutch translation, as *Verhandeling over het licht*, Epsilon Uitgaven, Utrecht (1990), ISBN 90-5041-022-7.

2.11 B.M. van Oerle, D. Bisero, G.J. Ernst, J.W.J. Verschuur and W.J. Witteman, "High efficient harmonic generation in two BBO crystals by means of walk-off compensation", Proc. IEEE/LEOS Symp. Benelux Chapter, (1996) pp25 – 27.

2.12 B.M. van Oerle and G.J. Ernst, "Autocorrelation measurements of bursts of picosecond pulses", Appl. Opt. **35,** 25 (1996) pp5177 – 5179.

2.13 R. Wyatt and E.E. Marinaro, "Versatile single-shot background-free pulse duration measurement technique for pulses of subnanosecond to picosecond duration", Appl. Phys. **25** (1981) pp297 – 301.

3. Semiconducting Photo Cathode Materials

Several aspects of the three step model of photoemission are explained, as it is applied to photoemission from semiconductors. A number of semiconducting photo cathode materials have been used in the TEU-FEL linear accelerator. A survey of the properties of the alkali-antimonide and alkali-telluride photo cathodes is given.

3.1 Three-step model of photoemission

The photoelectric effect was first observed in 1887 by Heinrich Hertz [3.1], who noted that a spark between two electrodes would occur more easily if the negative electrode was illuminated by ultraviolet light[†] . After the discovery of the electron in 1897 this effect was attributed to the emission of electrons from the metal under illumination. The pioneers in the field (notably Thomson and Lenard) noted also that the photo current was directly proportional to the illumination intensity, and that the energy of the emitted electrons did not depend on this intensity; two effects that could not be explained by classical electromagnetic theory.

It was not until 1905, that Albert Einstein described photoemission as a quantum-mechanical phenomenon. This established the foundations of the quantum theory of radiation. Photoemission could be described as the absorption of a single photon with

[†] In fact, Hertz' discovery was accidental. He was studying the propagation of electromagnetic waves in dielectrics, for which purpose he had two oscillating circuits containing spark gaps. The first circuit generated the waves, the second detected them. Because the spark in the second circuit was very weak, Hertz shielded the electrode from the surrounding light to make his observations easier. He was very annoyed to find that this made it more difficult to produce the spark

energy $h\nu$ by an electron that consequently escaped from the material. The number of emitted electrons is proportional to the number of incident photons, and the energy absorbed by the photoelectrons depends linearly on the frequency of the incident photon; thus explaining the effects noted by Thomson and Lenard.

Having established the origin of the photoelectric effect, physicists set out to determine whether the effect originated on the surface of the photoemissive material, or whether it was an effect occurring in the material volume. This debate continued for the first half of the twentieth century, until Spicer [3.2] suggested a model for photoemission in metals and semiconductors, that has come to be known as the three-step model.

Central to this model is the realisation that photoemission in these materials is a volume process, which means that it is determined by the properties of the bulk material, rather than by surface effects. As we shall see, the term "volume" should be taken broadly, since most photoactive materials are used as thin films with a thickness of less than 100 nm. The three steps in the model are:

1. Excitation of electrons by the photons.
2. Transport of the electrons through the bulk material to the surface.
3. Escape of the electrons to the vacuum.

Consider for example the energy band scheme of Cs_3Sb in Figure 3.1. A photon with an energy higher than the band gap E_G can excite an electron from the valence band to the conduction band. This electron will migrate through the material, gradually losing energy in collisions. It will only escape from the material if, by the time it reaches the surface, it has enough energy left to overcome the potential barrier E_A. In this model, photons with an energy smaller than the cut-off energy $E_C = E_A + E_G$ will not be able to extract electrons from the material, since they will not excite electrons above the vacuum level. Practical photo cathodes will emit electrons at photon energies below the cut-off energy, due to band bending at the surface of the cathode.

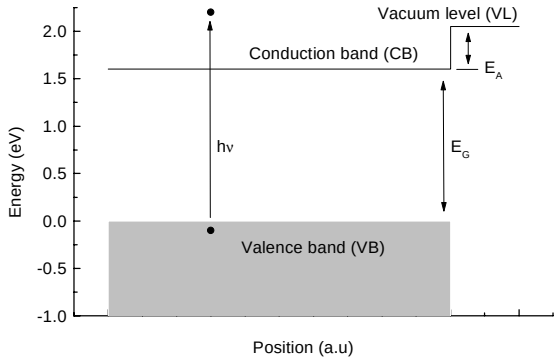

Figure 3.1: The energy band scheme of Cs_3Sb. Band gap energy E_G = 1.6 eV; electron affinity E_A = 0.45 eV.

If the photon current density in the photo cathode is given by $P(h\nu, z)$, then the number of excited electrons will be equal to $-dP/dz$. Only a fraction $T(h\nu, z)$ of the excited

electrons will reach the surface of the cathode, and of this fraction only a fraction $D(E)$ will have sufficient energy to escape to the vacuum. The general expression for the photo current is therefore

$$I_c(h\nu) = \int_0^{\delta} \int_{E_C}^{h\nu} \frac{dP}{dz}(h\nu, z)\, T(h\nu, z)\, D(E)\, dE\, dz \tag{3.1}$$

The integration is over the electron energy E and over the co-ordinate z, where δ is the thickness of the photoemissive layer. E_C and $h\nu$ are respectively the lowest and highest possible energy for an electron in the vacuum. The important parameter in photo cathodes is the quantum efficiency (QE), that is defined as the ratio of the number of emitted electrons to the number of incident photons:

$$QE = \frac{h\nu}{e} \frac{I_c}{P} \tag{3.2}$$

where I_c is the photo current and P the power of the incident radiation. In general, the quantum efficiency depends on the wavelength of the light. In the next three sections the steps of the three-step model will be examined more carefully, and the theory will be applied to photoemission from semiconductors.

3.1.1 Photoexcitation of electrons

The amplitude of an electromagnetic wave travelling in a metal or semiconductor will decrease as a result of the interaction with the material. If all absorbed photons excite electrons from the valence band to the conduction band, the density of electrons in the conduction band is proportional to the co-ordinate derivative of the photon density. The photon density is proportional to the time-averaged energy density in the electromagnetic wave. We will proceed to calculate this quantity, starting with the boundary conditions at the interfaces between the vacuum, the photoactive layer and the substrate, as they follow from Maxwell's equations.

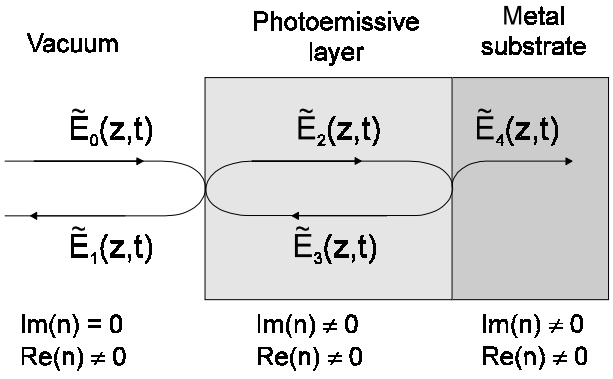

Figure 3.2: Reflection, absorption and transmission of a monochromatic wave in a thin, absorbing film deposited on a metal substrate.

The following discussion is similar to that found in [3.3] on the reflection coefficient of thin layers, but it is different in the aspect that we continue to calculate the electric fields inside the thin layer. Consider a monochromatic, plane-polarised electromagnetic wave at normal incidence on a layer with thickness δ on a metal substrate (Figure 3.2). The electric field component of the incident wave is given by

$$\tilde{E}_0(z,t) = E_0\, e^{i(\omega t + k_1 z)} \tag{3.3}$$

The electric field in the layer is

$$\tilde{E}_2(z,t) + \tilde{E}_3(z,t) = E_2\, e^{i(\omega t + k_2 z)} + E_3\, e^{i(\omega t - k_2 z)} \tag{3.4}$$

Similar definitions hold for the reflected wave E_1 and the transmitted wave E_4. At the boundaries of the media, the tangential components of E and H fields must be continuous, as must the normal components of D and B. Since the wave is at normal incidence, the latter are all zero. At the first interface the co-ordinate $z = 0$ and we find:

$$E_0 + E_1 = E_2 + E_3 \tag{3.5}$$

for the continuity of the electric field E . Using the relation $H = dE/dz$ we find

$$\frac{E_0 - E_1}{Z_1} = \frac{E_2 - E_3}{Z_2} \tag{3.6}$$

for the continuity of the magnetic field H. Likewise, at the second interface:

$$E_2\, e^{ik_2\delta} + E_3\, e^{-ik_2\delta} = E_4 \tag{3.7}$$

$$\frac{E_2\, e^{ik_2\delta} - E_3\, e^{-ik_2\delta}}{Z_2} = \frac{E_4}{Z_3} \tag{3.8}$$

The parameters k and Z are respectively the wave vector and the complex characteristic impedance in the medium. They are related by

$$Z = \frac{\omega\mu}{k} \tag{3.9}$$

The characteristic impedance of the vacuum is real and equal to $Z_{vac} = 377\ \Omega$. In general, the impedance will have a real and an imaginary part. In an absorbing

medium, the imaginary part of Z is negative. The characteristic impedance is related to the – more frequently used – complex index of refraction $n = \eta + i\kappa$ by:

$$Z = \frac{Z_{vac}}{n} \tag{3.10}$$

Evaluating the boundary conditions (3.5 – 3.8) yields the complex Fresnel reflectance r:

$$r = \frac{E_1}{E_0} = \frac{(Z_2 - Z_1)(Z_2 + Z_3) + (Z_1 + Z_2)(Z_3 - Z_2)e^{2ik_2\delta}}{(Z_1 + Z_2)(Z_2 + Z_3) + (Z_2 - Z_1)(Z_3 - Z_2)e^{2ik_2\delta}} \tag{3.11}$$

In the special case of a thick layer $\delta \cdot \left|\mathrm{Im}(k_2)\right| >> 1$ the exponential approaches zero and this is reduced to:

$$r_{thick} = \frac{Z_2 - Z_1}{Z_1 + Z_2} \tag{3.12}$$

Using the relation (3.11) the equations (3.5 – 3.6) are written as:

$$E_2 = \tfrac{1}{2} E_0 \left(\frac{Z_1 + Z_2 + r(Z_1 - Z_2)}{Z_1} \right) \tag{3.13}$$

$$E_3 = \tfrac{1}{2} E_0 \left(\frac{Z_1 - Z_2 + r(Z_1 + Z_2)}{Z_1} \right) \tag{3.14}$$

Given these fields, the time average of the Poynting vector can be calculated:

$$P = \tfrac{1}{2} \mathrm{Re}\left((\tilde{E}_2 + \tilde{E}_3) \times (\tilde{H}_2 + \tilde{H}_3)^* \right) \tag{3.15}$$

where the asterix denotes the complex conjugate. Expressing H in terms of E and expanding the vector product yields:

$$\frac{1}{Z_2^*} \left(E_2 E_2^* e^{i(k_2 - k_2^*)z} - E_2 E_3^* e^{i(k_2 + k_2^*)z} + E_3 E_2^* e^{-i(k_2 + k_2^*)z} - E_3 E_3^* e^{-i(k_2 - k_2^*)z} \right) \tag{3.16}$$

Recall that the wave vector k_2 is complex and related to Z_2 by $Z_2 = \omega\mu / (k_r + ik_i)$. Substituting this into the above expression leads to:

$$E \times H^* = \frac{k_r - ik_i}{\omega\mu}\left(E_2 E_2^* e^{-2k_i z} - E_2 E_3^* e^{2ik_r z} + E_3 E_2^* e^{-2ik_r z} - E_3 E_3^* e^{-2k_i z}\right) \quad (3.17)$$

The first and last terms between the brackets of (3.17) are real. The second and third term are complex conjugates; therefore their difference is wholly imaginary. We can temporarily rewrite these four terms as $A + iB$ and rewrite the Poynting vector as:

$$\begin{aligned} \tfrac{1}{2}\mathrm{Re}\left(E \times H^*\right) &= \mathrm{Re}\left(\frac{k_r - ik_i}{2\omega\mu}\left(A + iB\right)\right) \\ &= \frac{1}{2\omega\mu}\mathrm{Re}\left(k_r A + ik_r B - ik_i A + k_i B\right) \\ &= \frac{1}{2\omega\mu}\left(k_r A + k_i B\right) \end{aligned} \quad (3.18)$$

Substituting the original expressions for A and B, we arrive at

$$P = \frac{1}{2\omega\mu}\left[k_r\left(E_2 E_2^* e^{-2k_i z} - E_3 E_3^* e^{2k_i z}\right) + 2k_i\,\mathrm{Im}\left(E_3 E_2^* e^{-2ik_r z}\right)\right] \quad (3.19)$$

for the energy flow in the photoemissive layer towards the metal substrate. There are three terms contributing to the Poynting vector. The first term corresponds with the incoming electromagnetic wave E_2, travelling from left to right in Figure 3.2. Likewise, the second term corresponds with the wave E_3, which is the reflection of E_2 on the cathode surface. The third term accounts for the interference between E_2 and E_3.

In the limit $\delta \cdot \left|\mathrm{Im}\left(k_2\right)\right| >> 1$ the energy $(E_3)^2 \to 0$, as can be seen by substituting relation (3.12) into (3.14). So if the thickness of the layer is sufficiently large, the effect of the reflected wave E_3 on the Poynting vector can be neglected. For example, in a 55 nm thick Cs_2Te layer on a molybdenum substrate the energy of the reflected wave E_3 is less than 1 % of the incident wave E_0. This means that in thick photo cathode layers, the intensity of the incident radiation will decrease exponentially as a function of the distance.

In Figure 3.3b the magnitude of the Poynting vector is plotted as a function of distance, for several thicknesses of a Cs_3Sb photo cathode. The graphs have been normalised to the same initial value. The graphs shows that in a thin layer, the intensity of the radiation drops faster as a function of distance than is the case in a thick layer. This means that in a thin photoemissive layer, a larger fraction of the electrons is excited near the vacuum surface, than is the case in a thick photoemissive layer.

Going back to (3.5 – 3.8), we can also solve for the complex Fresnel transmission t:

$$t = \frac{E_4}{E_0} = \frac{4Z_2 Z_3 e^{ik_2\delta}}{\left(Z_1 + Z_2\right)\left(Z_2 + Z_3\right) + \left(Z_2 - Z_1\right)\left(Z_3 - Z_2\right)e^{ik_2\delta}} \quad (3.20)$$

The transmission yields the magnitude of the electromagnetic wave that propagates into the metal substrate. For thin films (less than 100 nm of Cs_3Sb) a substantial fraction of the energy of the incoming wave is absorbed in the metal substrate.

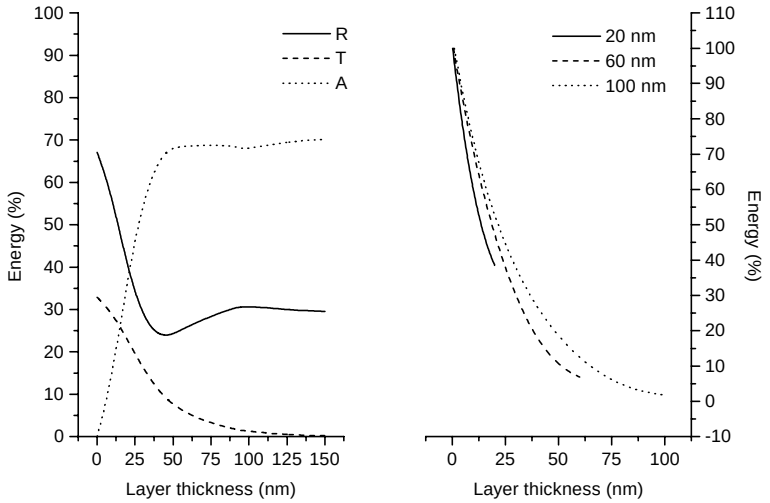

Figure 3.3: Left: reflection, absorption and transmission of a Cs_3Sb film on a metal substrate as a function of the film thickness. Right: the energy density flux in the film as a function of position, given for layer thicknesses of 20, 60 and 100 nm.

Figure 3.3a shows the transmission $T = t^2$, reflection $R = r^2$ and total absorption $A = 1 - T - R$ of a Cs_3Sb film on a molybdenum substrate, as a function of the film thickness. The uncoated substrate ($\delta = 0$ nm) reflects 68 % of the incident light. The remaining 32 % is absorbed in the substrate. As the thickness of the Cs_3Sb film increases, the magnitude of the transmitted wave drops quickly. For a 100 nm thick film, its energy is only 1 % of the incoming wave.

3.1.2 Transport of electrons in semiconductors

A very thorough description of the physics of the transport of conduction band electrons through semiconductors is given in [3.4]. A full model of the transport must include electron-photon, electron-electron and electron-phonon interaction, as well as scattering of electrons on semiconductor impurities and the effect of band bending around these impurities and near the bopundaries with the vacuum and the substrate. In this section, a simplified model will be presented, in which only the electron-phonon interaction is taken into account.

At low photo current, the density of electrons in the conduction band is small compared to the electron density in the valence band. The incoming photons will interact mainly with the valence band electrons and the interaction of conduction band electrons with the photons can be neglected. Also, due to the low conduction band electron density, the effect of electron-electron interactions on the transport will be

negligible. These assumptions may be invalid in metals, since the electron density in metals is much larger than in semiconductors. A photoexcited electron in a metal may loose a large fraction of its energy in collision with another electron. This, together with the large reflectivity of the surface, explains the low quantum efficiency of metals.

To measure the photo current, a small negative voltage is applied to the cathode. This leads to an electric field on the cathode surface that removes the emitted electrons from the vicinity of the cathode. The field is usually in the order of 100 V/m. An electron transversing a 100 nm thick photoactive layer will gain an energy of 10 μeV, which is substantially less than the average energy of electrons in the conduction band. Therefore, the effect of the external electric field on the electron transport can be safely neglected.

The energy distribution of electrons in a semiconductor is given by the Fermi-Dirac distribution:

$$f(E) = \frac{1}{e^{(E-\mu)/k_b T} - 1} \tag{3.21}$$

where μ is the Fermi level of the material and k_b is Boltzmann's constant. In intrinsic semiconductors, the Fermi level is exactly in the middle of the band gap,. i.e. $\mu = \frac{1}{2} E_{gap}$. The distribution of photoexcited electrons in the conduction band is hence given by $f(E - h\nu)$. Since phonons obey Bose-Einstein statistics, the average energy of a phonon around room temperature will be $E = \frac{1}{2} k_b T$, which is approximately 10 meV. This is substantially smaller than the average energy of a photoexcited electron, and we can thus expect a net energy transport from the electrons to the crystal lattice. To simplify the model even further, only electron-phonon collisions in which the electron looses energy to the lattice will be considered.

A word must be said on the validity of the above approximations under operating conditions of the photo cathode. When a photo cathode is used in a linear accelerator, the accelerating field on the cathode can be as high as 20 MV/m. The energy of an electron migrating from the substrate to the surface of a 30 nm thick cathode will increase by 0.6 eV, which is a substantial fraction of the initial energy. Thus the influence of the external electric field can not be neglected in this case. Furthermore, the number of photoexcited electrons will be much larger under operating conditions (peak currents of 100 A compared to 1 μA under preparation conditions) which indicates that electron-electron interaction might become important.

It is important to realise that the electron dynamics in (and consequently the quantum efficiency of) photo cathodes under operating conditions in the linear accelerator will differ from those under preparation conditions in the preparation chamber. The experimental data that will be presented in this chapter were mainly gathered under preparation conditions, and then any electron-electron interactions and any effects of an external electric field can be safely neglected.

Also, the effect of electron-hole recombination can be neglected since this occurs on a far larger timescale than the electron transport through the photoactive layer. In semiconductors, the transport time is typically on the order of picoseconds, whereas the decay time of an electron-hole pair can be as long as microseconds.

An electron will thus migrate at random through the photoactive layer, occasionally colliding with phonons. Eventually it will either reach the metal substrate or the cathode surface, or it will loose energy in collisions until it drops back into the valence band. Due to the scattering of photo-electrons the probability that an electron will reach the surface decreases with the depth of the electron in the material. The mean path between collisions $L(h\nu)$ is a function of the electron energy and is approximately $L \approx 1$ nm for low-energetic electrons.

3.1.3 Escape of electrons to the vacuum

If an electron reaches the cathode substrate, it is submerged in the electron sea of the metal and consequently lost for the photoemission. An electron reaching the surface will escape to the vacuum, only if the kinetic energy component normal to the surface is large enough to overcome the potential barrier. Assuming the electrons to be plane-wave-like with energy $E \propto k^2$, this condition defines an escape cone for electrons [3.5]:

$$\cos(\theta) = \sqrt{\left(\frac{E_A + E_G}{E}\right)} \tag{3.22}$$

If an electron is outside the escape cone, it will reflect specular on the surface without losing energy. The existence of the escape cone leads to an angular distribution of the emitted electrons. For an isotropic distribution of electrons inside the layer, the fraction $D(E)$ which escapes is given by

$$D(E) = \tfrac{1}{2}\left(1 - \sqrt{\frac{E_A + E_G}{E}}\right) \tag{3.23}$$

Using Monte Carlo simulations based on the three step model, we can calculate the QE as a function of the thickness of a photo active layer. To this end, the behaviour of a large number ($N_e \approx 5000$) electrons in a photoemissive layer is simulated. The initial electron distribution is found using the derivative of the Poynting vector (3.19). The electrons are then allowed to migrate through the material. After having migrated a distance L in a random direction, the energy of the electron is decreased by an amount equal to the mean phonon energy. This process is repeated until all the electrons had either dropped back into the valence band, or have reached the substrate or the vacuum surface. The ratio of the number electrons that reaches the vacuum surface to the number of incident photons then yields the QE.

Figure 3.4 shows the calculated quantum efficiency of Cs_2Te and Cs_3Sb films at respectively 265 nm and 527 nm, as a function of the film thickness. The Cs_3Sb film has an optimum thickness at 40 nm. The optimum thickness of the Cs_2Te film is 70 nm. These values relate to experimentally determined thicknesses: Sommer [3.6] cites a thickness of 26 nm to 35 nm for Cs_3Sb cathodes, and Johnson [3.7] finds an optimum thickness of 68 nm for Cs_2Te cathodes.

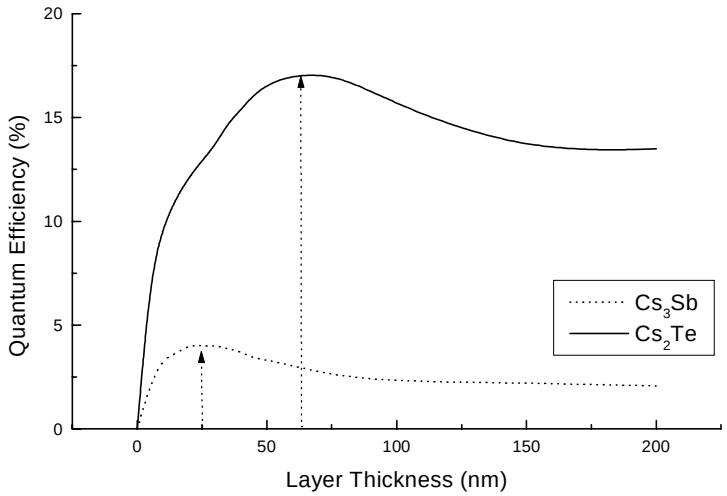

Figure 3.4: QE of Cs_3Sb and Cs_2Te photo cathodes, versus the layer thickness. The data is calculated using a Monte Carlo method.

At first, it may seem surprising that the curve of QE versus layer thickness δ shows an optimum value. One might expect that since the number of absorbed photons increases with increasing δ (as is shown in Figure 3.3a), also the QE should increase monotomically with δ. However, we saw in Figure 3.3b that in a thick photo cathode, the photoexcited electrons are generated deeper inside the photoactive layer, thus decreasing the possibility that they will reach the vacuum surface with sufficient energy to escape. This limits the QE of thick photo cathodes and causes the curve in Figure 3.4 to show a maximum value.

3.2 Set-up of the photo cathode preparation chamber

Photo cathodes are very sensitive to contamination. This is especially the case during preparation, and therefore the preparation chamber is kept at an ultra high vacuum pressure. The pressure in the chamber is typically in the order of 10^{-8} Pa. A schematic of the preparation chamber interior is given in Figure 3.5.

The photo cathode material is deposited on a molybdenum substrate, that is mounted on an actuator. The substrate is insulated thermally and electrically from the rest of the preparation chamber. A heater spiral is mounted behind the cathode substrate, and a chromel-constantan thermocouple is used to measure the substrate temperature. This material is used because it is not magnetic, and can therefore not influence the

measurement of the photo current. Because of the relatively low melting point of the thermocouple, the substrate temperature is limited to 600 °C.

The chemicals that are used to prepare the cathode are stored in four containers (these containers are usually referred to as “boats”), that are mounted on a second actuator, perpendicular to the first. The boats can be heated individually. A chromel-alumel thermocouple is connected to the rear end of each boat to measure the evaporation temperature of the chemical. The deposition of a chemical is started by heating the boat and moving it in front of the cathode surface. In our set-up, we cannot deposit more than one chemical at a time, but we have the advantage of being able to control the deposition time. The deposition of a chemical is stopped immediately by moving the boat away from the cathode.

Antimony (Sb) and tellurium[†] (Te) are stored as elements. Since cesium (Cs) and potassium (K) react violently with oxygen, it is not very convenient to store them as elements. They are stored as chromates that need to be activated, i.e. the chromates must be heated to a temperature where they dissociate into the elements. A few parts zirconium (Zr) have been mixed with the chromates; this elements is a catalyst for the dissociation. A few parts tungsten (W) act as a moderator. The cesium chromate dissociates around 500 °C, the potassium chromate needs to be heated up to 700 °C before it dissociates.

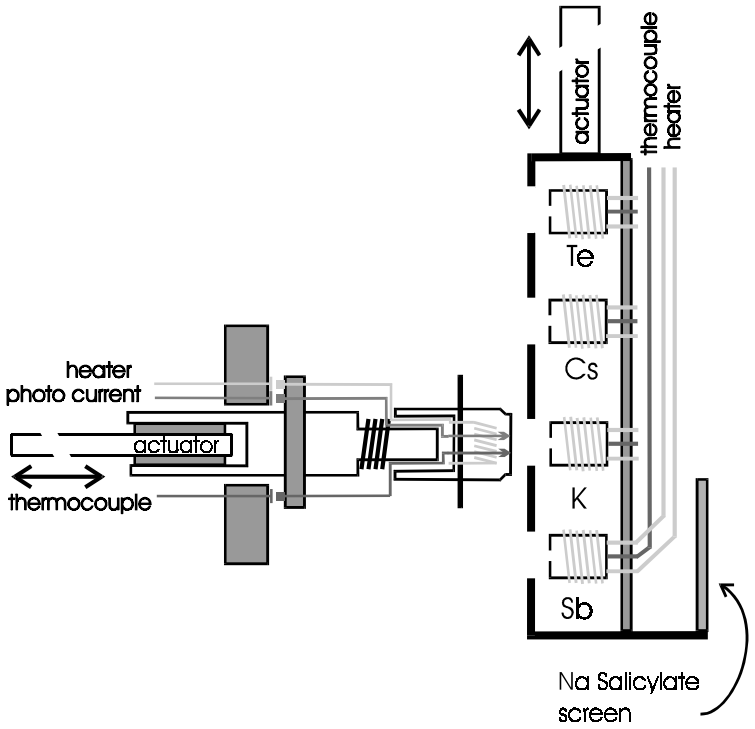

Figure 3.5: The interior of the TEU-FEL photo cathode preparation chamber.

[†] Tellurium is a poisonous material. Workers exposed to as little as 0.01 mg/m^3 of air develop “tellurium breath”, which has a sharp and very distinctive garlic-like odour. This smell can linger for months. There is a piece of garlic attached above the door of our office, to alert the experimentalists to this effect.

During photo cathode formation, the temperature of the antimony boat is 395 °C; the potassium and cesium are heated up to respectively 525 °C and 565 °C. The tellurium is heated up to 300 °C. In this set-up there is no method to determine the thickness of the deposited layers, and therefore we will refer to the evaporation times when we give information about the preparation procedure.

The cathode is illuminated through a window in the preparation chamber. When preparing an alkaline photo cathode, a green He-Ne laser at 541 nm is used for illumination; to illuminate the telluride cathodes, light from a mercury arc lamp is filtered through a band pass interference filter at 259 nm. This arc lamp is also used to determine the spectral sensitivity of the cathodes. The photo current is monitored continuously on a recorder.

After the photo cathode has been prepared, both the boats and the cathode substrate are allowed to cool down to room temperature. Then the valve between the accelerator and the preparation chamber is opened and the photo cathode is inserted into the first cell of the linear accelerator.

3.3 Alkali-antimonide photo cathodes

The alkali-antimonide photo cathodes have been studied since their discovery in the 1960s [3.6]. They have a relatively high QE in the visible part of the spectrum. This property is exploited in photo-injectors, where they are usually illuminated by the second harmonic of a Nd:YLF or Nd:YAG laser. A disadvantage of the alkali-antimonide cathodes is that they are very sensitive to contamination. This necessitates the use of an ultra-high vacuum environment to reduce the effects of oxidation and the speed of formation of monolayers on the cathode surface. Despite these precautions, the QE of a cathode will steadily decrease when it is used in a linear accelerator. A useful parameter to characterise this behaviour is the half lifetime of the cathode, defined as the time in which the quantum efficiency drops to half its initial value.

3.3.1 Cesium antimonide (Cs_3Sb)

Cs_3Sb was the first alkali-antimonide photo cathode to be used as an electron source in radio-frequent accelerators [3.8]. It is prepared by letting a pre-deposited antimony film react with cesium vapour:

$$Sb_{(s)} + 3Cs_{(g)} \rightarrow Cs_3Sb_{(s)} \tag{3.24}$$

This is a reversible reaction. During operation in the accelerator, the material dissociates in antimony and cesium, after which the cesium sublimates on the walls of the accelerator. The cesium on the walls lowers the work function of the metal, thus allowing electrons to escape into the vacuum. These discharges substantially degrade the performance of the accelerator.

Because of the above mentioned effects, the material Cs_3Sb has not been used in our accelerator, but it has been produced in the preparation chamber. The recipe to produce a Cs_3Sb cathode is as follows:

1. During 10 minutes, deposit a layer of Sb on a Mo substrate at room temperature.
2. Expose the heated layer to Cs vapour, until a maximum in photo current is observed.
3. Stop the Cs deposition.

If the substrate is heated to 120 °C, multiple layers of cesium and antimony can be added, thus allowing a determination of the optimum thickness of the cathode. If the substrate is at room temperature, it is only possible to add one layer of cesium to one layer of antimony. This does not influence the final QE provided that the layer thicknesses are chosen at their optimum values. The QE of Cs_3Sb as a function of the photon energy has been plotted in Figure 3.6. Some material parameters of Cs_3Sb are given in Table 3.1.

	Cs_3Sb	*K_3Sb (cubic)*	*CsK_2Sb*
QE (527 nm) (%)	1 – 2	< 1	≈ 4
E_G (eV) [3.5]	1.6	1.4	1.0
E_A (eV) [3.6]	0.45	0.9	1.1
δ (nm) [3.6]	25	25 – 35	?
η [3.10]	2.4	2.0	?
κ [3.10]	1.45	0.6	?

Table 3.1: Some material parameters of antimony-based photo cathodes.

3.3.2 Potassium antimonide (K_3Sb)

A potassium-antimonide photo cathode is prepared by letting a layer of antimony react with a potassium vapour:

$$Sb_{(s)} + 3K_{(g)} \rightarrow K_3Sb_{(s)} \tag{3.25}$$

K_3Sb exists in two crystal configurations: a hexagonal modification which has a purple colour, and a cubic modification which has a brown colour. The hexagonal K_3Sb can be produced if the cathode is prepared at 180 °C, the cubic K_3Sb is obtained if the preparation is carried out at room temperature. A bake at 180 °C will transform a cubic type K_3Sb in a hexagonal type. The spectral sensitivity of both types of cathode is given in Figure 3.6.

In the visible region of the spectrum, we measure a lower quantum efficiency for the hexagonal K_3Sb compared to the cubic K_3Sb. This is confirmed by other studies [3.6] and it is attributed to the more dense packing of atoms in the cubic crystal configuration. Due to its limited quantum efficiency at 527 nm, the K_3Sb cathode is not very useful as an electron source in the accelerator. It is used as the main ingredient for the bi-alkali-antimonide cathode, that will be treated in the next section.

3.3.3 Cesium potassium antimonide (CsK_2Sb)

A CsK_2Sb cathode is fabricated by exposing a K_3Sb cathode to a cesium vapour:

$$K_3Sb_{(s)} + Cs_{(g)} \rightarrow CsK_2Sb_{(s)} + K_{(g)} \uparrow \tag{3.26}$$

This substitution occurs first near the surface of the cathode; the Cs atoms next diffuse into the bulk material, trading places with K atoms that have not yet been substituted. If the arrival rate of Cs atoms at the surface is larger than their diffusion rate into the bulk material, there will occur multiple substitutions of K at the surface. This will decrease the QE of the cathode before a stoichiometric amount of Cs has been reached in the bulk material. To ensure proper diffusion of Cs to the bulk material, it is essential to use a high substrate temperature (≈ 120 °C) to produce a CsK_2Sb cathode. To prepare the CsK_2Sb cathodes, we use the following recipe:

1. Heat the cathode surface to 120 °C. During 10 minutes, deposit a layer of Sb.
2. Deposit K until a maximum in QE has been reached.
3. Add a surplus amount of K until the total evaporation time is twice the time required to obtain the maximum QE.
4. Add Cs until the photo current no longer increases in time.
5. Cool down the cathode to room temperature.

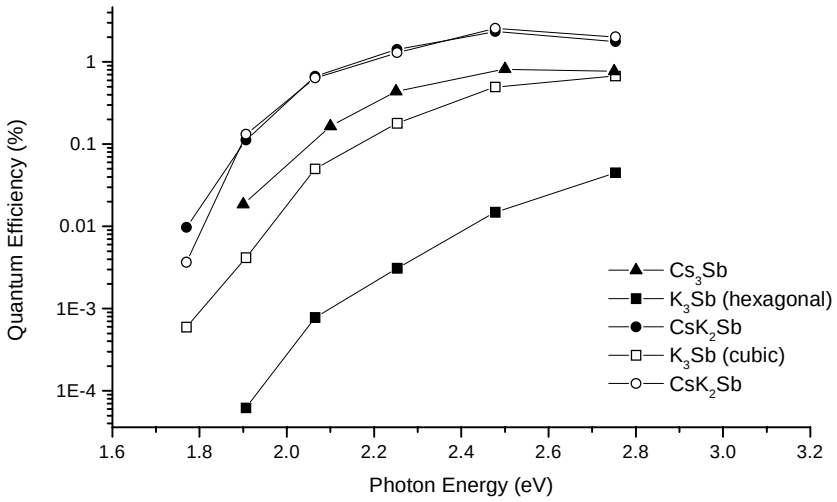

Figure 3.6: Quantum efficiency of antimony-based photo cathodes, as measured in the TEU-FEL preparation chamber.

Figure 3.7 shows the QE during the formation of a CsK_2Sb cathode. Prior to the recording of this data, Sb was deposited on the substrate during 17 min, after which K was added to the cathode. After 9 min of K evaporation, a maximum QE = 0.45 % was observed. A secondary maximum (QE = 0.3 %) appears after 17 min. The K deposition is stopped after 35 min, after which Cs is added for 30 min. The QE then saturates at

3.4 %, a value that increases to 3.8 % when the boats are moved away from the cathode.

In our experience, there is little correlation between the QE of the initially formed K_3Sb cathode, and the QE of the final CsK_2Sb cathode [3.11]. In fact, we have observed (Figure 3.6) that the spectral sensitivity of the CsK_2Sb cathode does not even depend on the crystal configuration of the K_3Sb cathode: the spectral sensitivity of a CsK_2Sb cathode grown of a cubic K_3Sb cathode is almost identical to that of a cathode grown on a hexagonal K_3Sb cathode.

To learn about the decay of the CsK_2Sb cathodes while using them in the accelerator, the spectral sensitivity of a cathode was measured on 4 occasions: immediately after preparation, after a 60 hour rest period in the preparation chamber, after 2 hours of use in the accelerator and after it had been regenerated by adding a layer of Cs. These data are displayed in Figure 3.8.

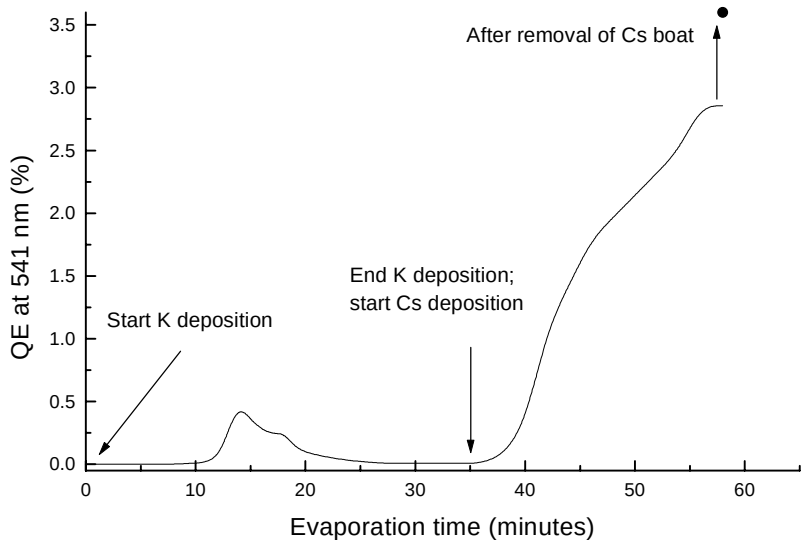

Figure 3.7: The quantum efficiency of a CsK_2Sb photo cathode during formation. Prior to this data, antimony was deposited on the substrate during 18 minutes.

During operation, the QE of the cathode dropped significantly. The decrease in quantum yield is most dramatic in the red part of the spectrum. This suggests the use of shorter wavelength radiation to illuminate the cathode. By replenishing the amount of Cs in the cathode, the efficiency can be restored to half its initial value. These regenerated cathodes tend to have shorter lifetimes than the original ones. This leads to the conclusion that the evaporation of Cs from the cathode plays an important part in the decay of the cathode, but that it is also affected by other factors (for instance oxidation and pollution with trace elements).

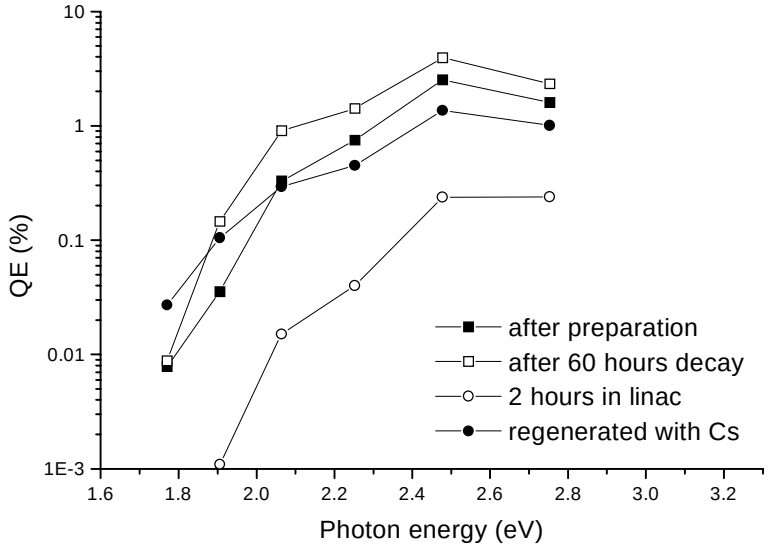

Figure 3.8: The decay and regeneration of a CsK_2Sb cathode, used in the linear accelerator.

3.4 Alkali-telluride photo cathodes

In contrast with their antimony-based counterparts, the tellurium-based photo cathodes are solar-blind, which means that they are not sensitive to visible radiation. The band gap of the best known tellurium-compound, (Cs_2Te) is 3.2 eV and its electron affinity is 0.3 eV [3.7] which means that it is only sensitive to radiation with a wavelength shorter than 350 nm. When they are used as electron source in a linear accelerator, these cathodes are usually illuminated by the fourth harmonic of either Nd:YAG or Nd:YLF laser.

The behaviour of tellurium-based cathodes under operating conditions in the accelerator differs somewhat from the behaviour of the alkali-antimonide cathodes. In the first hours the quantum efficiency drops with a speed significantly lower than that of the antimonide cathodes. After a while this decay slows down substantially and the quantum efficiency remains stable for a long time. In our experiments, the cathode can be used until it reaches a quantum efficiency of 1 %.

3.4.1 Cesium telluride (Cs_2Te)

The fabrication process for a Cs_2Te cathode is similar to that of a Cs_3Sb cathode. First, a layer of Te is deposited on the substrate, and this layer is exposed to a Cs vapour:

$$Te_{(s)} + 2\,Cs_{(g)} \rightarrow Cs_2\,Te_{(s)} \tag{3.27}$$

In our set-up, the deposition of Cs is continued until a maximum in QE is observed, at which point the deposition is stopped immediately. Kong *et al* [3.12] report a

procedure in which Cs is added to the compound until the QE has dropped to 20 % of the peak value. After stopping the deposition at this point, the QE slowly recovers to almost the original value. Although this behaviour has also been observed in the TEU-FEL preparation chamber, we find it is not a necessary step in the formation process. The quantum yield as a function of photon energy is shown in Figure 3.12. It shows a quantum yield of 12 % at 259 nm (4.8 eV).

The ruggedness of this material is illustrated by the difficulties that we have experienced in removing it from the substrate. After an hour bake at 300 °C, the cathode still has a QE of 4 %. This high stability is probably caused by the diffusion of Cs and Te into the molybdenum substrate, as was suggested by Di Bona *et al* [3.13]. It is possible to remove the photoemissive layer by cleaning the substrate with soap, water and acetone, but since such a procedure involves breaking the vacuum of the preparation chamber this is not a preferred method. In practice, the cathode substrate is cleaned by heating the substrate to 600 °C for several hours. After such a bake-out the cathode usually has a residual QE ≈ 1 %. A new cathode is formed on top of this residue; the new cathode has a QE comparable to that of the old one.

Figure 3.13 shows the decay of the QE of a Cs_2Te cathode as it is used in the linear accelerator. In about 10 hours, the QE has dropped to half its initial value. After 15 hours of use, the QE stabilises at ≈ 4 %, at which QE the cathode can be used for a long time. This is in agreement with results found by other groups (e.g. [3.12]). A Cs_2Te photo cathode degraded by use in the accelerator can be regenerated to about 60 % of the initial QE by heating it to a temperature of 200 °C .

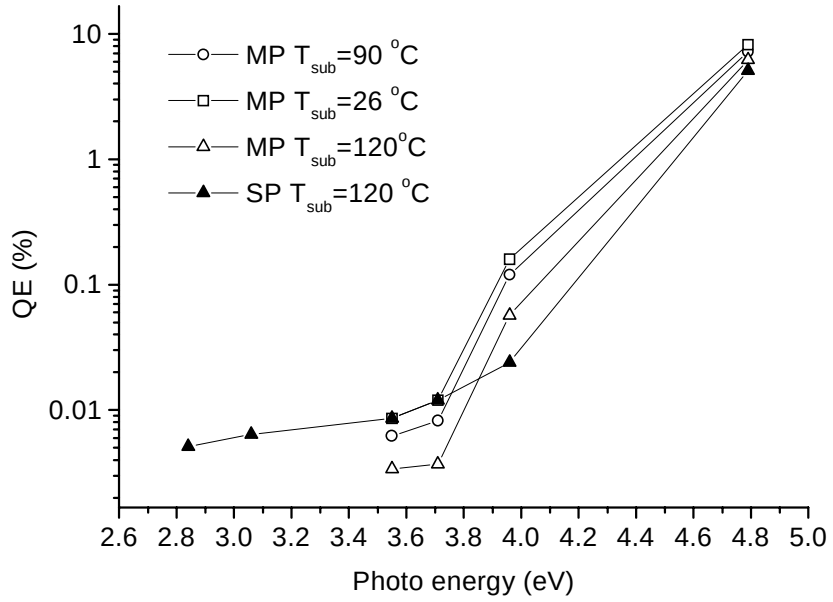

Figure 3.9: Quantum yield as a function of wavelength for potassium telluride cathodes, fabricated according to several recipes.

3.4.2 Potassium telluride (K-Te)

A K-Te cathode is formed by exposing a layer of tellurium to a potassium vapour [3.14]. Figure 3.11 shows the QE at 259 nm of a K-Te cathode as a function of the potassium evaporation time. During the preparation procedure the substrate temperature was kept at 120 °C. After about 15 minutes of evaporation a very quick increase of the QE up to a 7.5 % maximum value was observed; it was followed by an equally quick decrease to about 6.5 %, after which the QE slowly decreased to a saturation value of about 6 %. This shape of the QE as a function of the K evaporation time is a typical feature of the K-Te cathodes and is about the same when the evaporation process is performed keeping the substrate at 90 °C and 26 °C. For the latter temperature, the QE saturation value after the peak is very low (about 0.1 %), probably because of the presence of an excess of K at the surface, due to inefficient diffusion at room temperature of K through the already formed K-Te layer.

The shape of QE versus potassium evaporation time could be tentatively ascribed to a change of the film composition during the evaporation process itself. In fact, it has been demonstrated [3.15, 3.16] that the K-Te phase changes as a function of increasing K concentration, first from K_2Te_3 to K_2Te_2, then from K_2Te_2 to a compound that is most probably KTe and finally from KTe to K_2Te. The compounds K_2Te_3, K_2Te_2 and KTe have broad UV-absorption bands, whereas K_2Te has no absorption in the spectral region 220-700 nm [3.16] and therefore can not be the photoemissive material we are investigating. We believe it is reasonable to expect that K_2Te_3, K_2Te_2 and KTe have different photoemissive efficiencies at 259 nm; this circumstance could account for the change of the QE at 259 nm with potassium evaporation time.

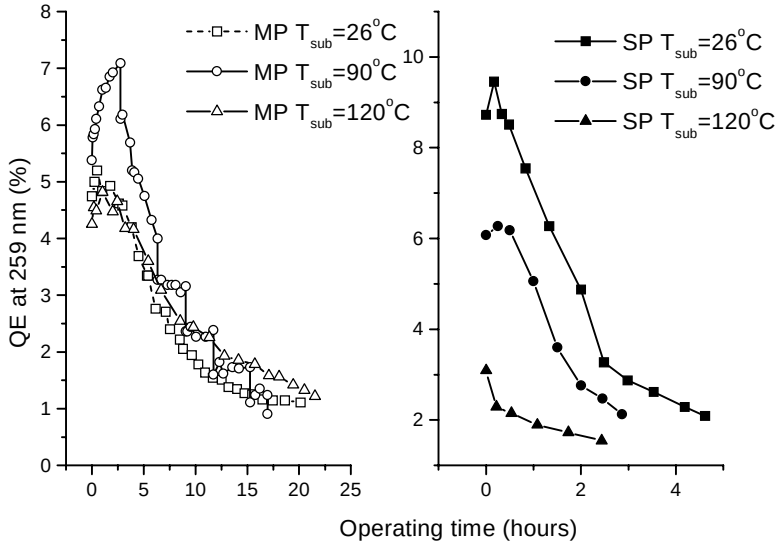

Figure 3.10: Decrease of the quantum efficiency of several potassium-telluride photo cathodes, due to their use in the linear accelerator.

Different optical properties of the material can be obtained by stopping the K evaporation either when the QE is at its maximum (preparation procedure called MP in the following) or when QE reaches the saturation value (preparation procedure called SP in the following). In Figure 3.9 the spectral response of K-Te in the photon energy range 2.84-4.79 eV is shown for MP cathodes evaporated at different temperatures. The spectral response of an SP cathode evaporated at T_{sub}=120 °C is also shown for comparison. As can be seen the QE at 4.79 eV (259 nm) of the MP cathode evaporated at 120 °C (6.2 %) is higher than the SP cathode's one (5.1 %). For low energies the situation is reversed; in particular, at 2.84 and 3.06 eV no photo current can be measured from an MP cathode, whereas a very low QE is still present for an SP cathode. It can also be seen that the QE for MP cathodes is highest if the substrate is kept at room temperature during the fabrication process.

In order to investigate the lifetime of the K-Te cathodes, QE measurements were performed as a function of operating time [3.17]. To this purpose, the accelerator operation was stopped for a few minutes and the photo cathodes were moved under UHV conditions to the preparation chamber, where the photo current produced by the Hg lamp was measured. Every operating session lasted on the average 3 hours; during the time between successive sessions the photo cathodes were kept in the preparation chamber. The cathodes have been used in these experiments until their QE dropped to a value lower than half the initial one.

Figure 3.10 shows the QE as a function of operation time for the K-Te cathodes, evaporated at three different substrate temperatures (26, 90 and 120 °C). From this figure the half-life of the cathodes has been determined and reported in Table 3.2. In fact, it was shown that different behaviours of the K-Te films can be obtained, once the Te evaporation has been accomplished, either by stopping the potassium evaporation when the QE is at its maximum or by continuing potassium evaporation after the QE maximum. It must be noticed that after an MP evaporation the QE of a K-Te cathode undergoes an exponential decay, with a characteristic time of the order of minutes, after which a stable QE value is reached. In the lifetime experiments involving the MP cathodes reported in this paper, the initial QE refers to the stable value reached a few hours after the evaporation process has been accomplished.

T_{sub}	*MP*	*SP*
120 °C	11.9	2.4
90 °C	9	1.83
26 °C	7.7	2.2

Table 3.2: Half life of several potassium telluride cathodes under operating conditions in the accelerator. The values are in hours.

The half-life values reported in Table 3.2 clearly show how the type of procedure (MP or SP) strongly affects the lifetime of the K-Te films. Photo cathodes evaporated at a certain substrate temperature with a MP procedure have much longer half-lives than photo cathodes evaporated at the same temperature with a SP procedure. We believe that this result is in agreement with the hypothesis that during the additional K

evaporation time necessary to go from a MP to a SP K-Te film the layer's chemical composition changes (for example from K_2Te_3 to K_2Te_2).

3.4.3 Cesium potassium telluride (Cs-K-Te)

The fabrication of a Cs-K-Te cathode is carried out by first evaporating a film of Te on the surface of the substrate, then exposing it to K and finally evaporating Cs [3.18]. During the whole process the photo current at 259 nm is monitored. It is also possible to fabricate a Cs-K-Te cathode by evaporating Cs immediately after Te, and before K, thus inverting the last two steps of the procedure described above. Although the final QE at 259 nm of the Cs-K-Te layer obtained with the latter sequence (Te→Cs→K) is much higher than that of the Cs-Te layer alone, the first mentioned sequence (Te→K→Cs) gives the best QE. Therefore, we will describe in this section only the results of Cs-K-Te layers fabricated with the first sequence (Te→K→Cs). The pressure in the preparation chamber rises during the evaporation process from the low 10^{-8} Pa range up to the high 10^{-8} Pa range. A 30 min Te evaporation time has been used to fabricate all the photo cathodes.

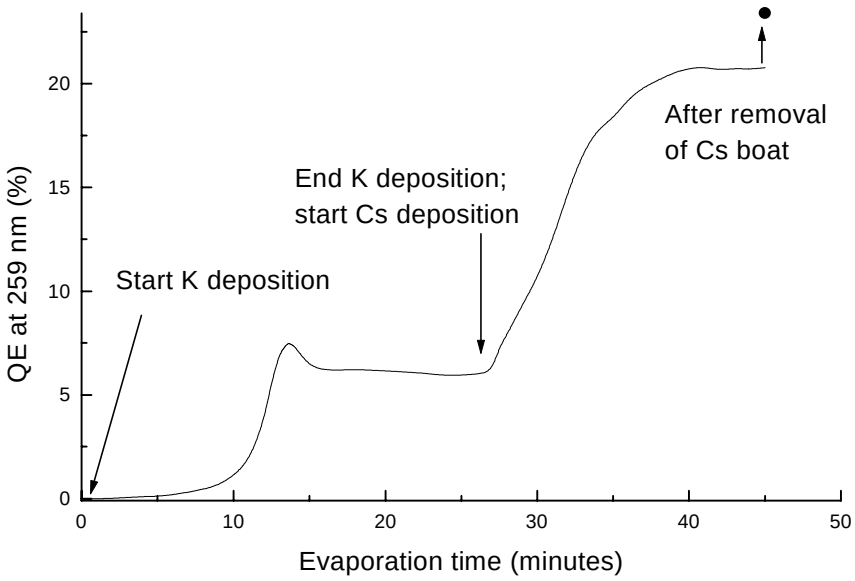

Figure 3.11: The quantum efficiency of a Cs-K-Te photo cathode during preparation. Prior to the recording of this data, a layer of tellurium was deposited on the substrate during 30 minutes.

Figure 3.11 shows the QE at 259 nm measured during the evaporation of K and Cs on a Te layer. The substrate temperature was kept at 120 °C during the Te and K evaporation, and at 150 °C during the Cs evaporation. The QE dependence on the K evaporation time is a typical feature of K-Te. It shows in this case a peak value of 7.5%, followed by a decrease and a final saturation at 6% QE. When Cs evaporation is started, a steep increase of the QE occurs, giving in about 15 minutes a value of 20.8%,

which remains constant with time until the end of the evaporation process. After removal of the Cs boat a 23.4% QE is measured. The difference between the QE saturation value and the final QE measured after boat removal must be ascribed to a partial shielding of the mercury lamp light during evaporation, due to the presence of the boat in front of the cathode.

The dependence of the final QE at 259 nm of Cs-K-Te photo cathodes on the K evaporation time has been investigated. For a given K evaporation time, the corresponding Cs evaporation time has been taken as long as required to reach the QE saturation. To this purpose, a Cs evaporation time which is roughly half the K evaporation time is required. It has been found that the QE of the Cs-K-Te photo cathodes does not change significantly by changing the K evaporation time in the range 13 to 27 min. The limits of the range correspond to a K evaporation process stopped at the QE maximum (13 min) or at the QE saturation (27 min, as shown in Figure 3.11).

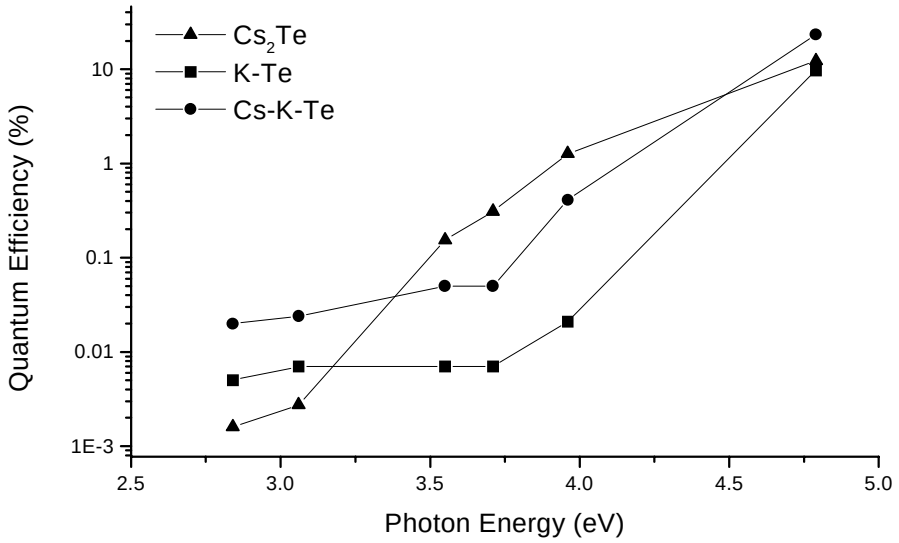

Figure 3.12: The quantum efficiency of the tellurium-based photo cathodes as a function of photon energy.

The spectral response of a Cs-K-Te photo cathode in the energy range 2.84-4.79 eV is shown in Figure 3.12, where also the typical spectral responses of K-Te and Cs_2Te photo cathodes have been reported for comparison. As could be reasonably expected, the shape of the spectral response for Cs-K-Te is somewhere in between the Cs_2Te and K-Te ones. Moreover, Cs-K-Te displays the highest QE at low energies (2.84, 3.06 eV) and at 4.79 eV (259 nm), whereas Cs_2Te has the best QE in the energy range 3.55-3.96 eV.

The behaviour of Cs-K-Te under operating conditions was also investigated. Figure 3.13 shows the quantum yield at 259 nm for a Cs-K-Te cathode. For comparison,

similar curves are included for Cs_2Te and K-Te (MP at 120 °C). Initially, the efficiency of the Cs-K-Te cathode is seen to drop rapidly. After a few hours, the speed decreases and the decay curve approaches that of K-Te. The decay of the QE of a Cs-K-Te cathode can be best described by a second-order exponential decay. The fast decay has a half life of 0.5 hours; the slow decay a half life of 5.3 hours.

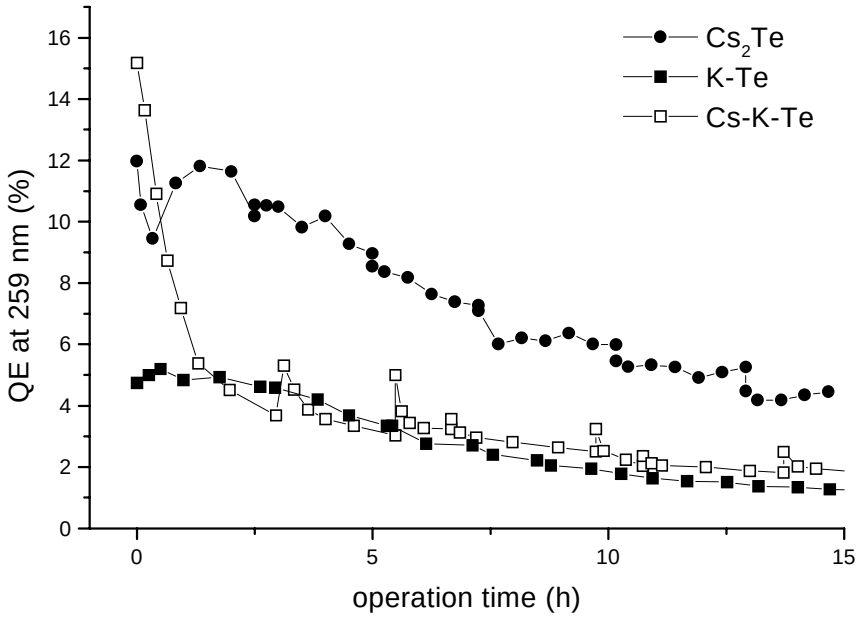

Figure 3.13: Decay of the quantum efficiency of tellurium-based photo cathodes as they are used in the linear accelerator.

3.5 Conclusions

The three step model of photoemission has been reviewed, and has been applied to photoemission in semiconductors. Using Monte Carlo simulation, the quantum yield of Cs_2Te and Cs_3Sb as a function of active layer thickness has been calculated. These calculations show that there is thickness at which the quantum yield is at a maximum. The calculated optimal thicknesses are in good agreement with the values found experimentally.

The properties of alkali-antimonide and alkali-telluride photo cathodes have been investigated. CsK_2Sb, Cs_2Te, K-Te and Cs-K-Te cathode have been prepared in the preparation chamber and used as electron sources in the accelerator. To our knowledge, the photoemissive properties of K-Te and Cs-K-Te have not been reported before. The long lifetime and high initial quantum yield of these materials allow to consider them as promising photo cathodes for electron photo-injectors.

A summary of the operational parameters of the cathodes is given in Table 3.3. In general, we can state that the tellurium-based cathode have a larger QE and a longer

lifetime under operating conditions than their antimony-based counterparts. From the data, it is clear that in terms of the operating lifetime the K-Te cathode is the superior cathode. However, this cathode has a relatively low QE at the illuminating wavelength. The maximum QE is obtained by using a Cs-K-Te cathode, but this cathode does not perform well under operating conditions.

	CsK_2Sb	*Cs_2Te*	*K-Te*	*Cs-K-Te*
Photon energy (eV)	2.35	4.7	4.7	4.7
QE (%)	3.8	12.0	8.1	23.4
lifetime (hours)	2	11	11.9	0.5 / 5.3
$E_G + E_A$ (eV)	2.1	3.8	4.5 – 5.0	4.0 – 4.5

Table 3.3: Operating parameters of photo cathodes used in the accelerator.

The cut-off energy $E_C = E_G + E_A$ for Cs_2Te is known from literature [3.7] and equals $E_C = 3.8$ eV. For K-Te and Cs-K-Te, no reliable measurements of this parameter are known. However, we can make estimates of E_C based on Figure 3.12. The QE of Cs_2Te at the cut-off energy is about 1 %. The QE of K-Te reaches that value between $E = 4.5$ eV and $E = 5.0$ eV; the QE of Cs-K-Te reaches that value between $E = 4.0$ eV and $E = 4.5$ eV. These values are used for estimates of E_C and they are given in Table 3.3. Note that the energy of the drive laser photons is close to the cut-off energy of the K-Te and Cs-K-Te compounds.

We have seen that, under operating conditions in the linear accelerator, the QE of the CsK_2Sb cathodes decreases most in the red part of the spectrum. Analogous to this case, one can expect the QE of the telluride cathodes to decrease most in the soft UV part of the spectrum. This means that the QE of the K-Te and Cs-K-Te cathode would decrease most at the wavelength of the drive laser. A possible method to improve the performance of these materials in the accelerator, is to illuminate them not with the fourth, but with the fifth harmonic (5.9 eV) of the Nd:YLF laser.

3.6 References

3.1 The original reference is H. Hertz, Ann. Physik **31**, 98 (1887). A more recent printing is in H. Hertz, *Electric Waves*, Dover Publications Inc, New York (1962), Chapter 4: "On an effect of ultra-violet light upon the electric discharge", pp63 – 79.

3.2 W.E. Spicer, "Photoemissive, photoconductive and optical absorption studies of alkali-antimony compounds", Phys. Rev. **112** (1958) pp114 – 122.

3.3 E. Hecht, *Optics*, Addison-Wesley Publishing Company, Reading (1987), Chapter 9: "Interference" pp333 – 391.

3.4 C. Jacoboni and L. Reggiani, "The Monte Carlo method for the solution of charge transport in semiconductors with applications to covalent materials", Rev. Mod. Phys. **55**, 3 (1983) pp645 – 705.

3.5 M. Cardona, L. Ley, *Photoemission in solids I: General principles*, Chapter 1, *Introduction*, Springer Verlag , Berlin (1978) ISBN 3-540-08685-4.

3.6 A.H. Sommer, *Photoemissive Materials*, J. Wiley and Sons Inc, New York, Sydney, Toronto (1968).

3.7 S.M. Johnson, “Ultraviolet angular response of cesium-telluride photo cathodes”, Appl. Opt. **31**, 13 (1992) pp2332 – 2342.
3.8 R.L. Sheffield, E.R. Gray and J.S. Fraser, “The Los Alamos photoinjector program”, Nucl. Instr. and Meth. A **272** (1988) pp222 –226.
3.9 E. Kansky, “Some physico-chemical aspects of the synthesis of alkali-antimonide photo-cathodes”, Adv. EEP **33 A** (1972) pp357 – 368.
3.10 P. Dolizy, “Optical method for investigating alkali-antimonide photo cathodes”, Vacuum **30**, 11-12 (1980) pp489 – 495.
3.11 B.M. van Oerle and G.J. Ernst, “On the use of CsK_2Sb photo cathodes in RF linacs”, Nucl. Instr. and Meth. A **358** (1995) pp287 – 290.
3.12 S.H. Kong, J. Kinross-Wright, D.C. Nguyen, R.L. Sheffield, “Cesium telluride photo cathodes”, J. Appl. Phys. **77**, 11 (1995) pp6031 – 6038.
3.13 A. Di Bona, F. Sabary, S. Valeri, P. Michelato, D. Sertore, G. Suberlucq, “Auger and X-ray photoemission spectroscopy study on Cs_2Te photo cathodes”, J. Appl. Phys. **80**, 5 (1996) pp3024 – 3030.
3.14 D. Bisero, B.M. van Oerle, G.J. Ernst, J.W.J. Verschuur, W.J. Witteman, “Photoemission from K-Te cathodes”, Appl. Phys. Lett. **69**, 24 (1996) pp3641 – 3643
3.15 A. Petric and A. D. Pelton, “The potassium-tellurium system”, Bull. Alloy Phase Diagrams **11**, 443 (1990)
3.16 L. D. Schultz, “Synthesis and characterisation of potassium polytellurides in liquid ammonia solution”, Inorganica Chimica Acta **176**, 271 (1990).
3.17 D. Bisero, B.M. van Oerle, G.J. Ernst, J.W.J. Verschuur, W.J. Witteman, “K-Te photocathodes: a new electron source for photoinjectors”, accepted for publication in J. Appl. Phys.
3.18 D. Bisero, B.M. van Oerle, G.J. Ernst, J.W.J. Verschuur, W.J. Witteman, “Photoemission from Cs-K-Te cathodes”, Appl. Phys. Lett. **70**, 12 (1997) pp1491 – 1493.

4. Characterisation of the Electron Beam

Classical beam optics is reviewed and the quantity emittance is defined. It is a measure of the quality of the electron beam, analogous to the M^2-number used in Gaussian optics. Several methods exist to measure this beam quality number. The pepper pot method, quadrupole scan, several multiple-screen techniques and phase space tomography will be explained and demonstrated. The duration of the electron bunch is determined using longitudinal phase space tomography and streak camera measurements. These measurements are combined with the emittance measurements to yield a value for the brightness of the beam.

4.1 Electron distribution transport theory

The motion of an ensemble of free electrons can be described completely in a six-dimensional space, spanned by the three co-ordinates and the three momentum components of the particles. This space is called phase space. Under most circumstances, it is not necessary to examine the equations of motion of the particles in six-dimensional phase space, but it is sufficient to use a two-dimensional model. Specifically, this is the case when a co-ordinate system exists in which there is no interaction between the x, y and z directions. Then the transport of the ensemble can be described in the two-dimensional space spanned by the transverse co-ordinate *x* and the inclination of the velocity vector:

$$x' \equiv p_x / p_z \tag{4.1}$$

p_z is the relativistic momentum in the longitudinal direction of the centre of mass of the distribution. Three examples of two-dimensional phase space plots with the corresponding beam envelope are given in Figure 4.1.

The distribution of the electrons in phase space is described by the distribution function $f(x,x')$. The mean value of an arbitrary quantity A over this distribution is defined as:

$$\langle A \rangle = \iint f(x,x')\, A \, \mathrm{d}x \, \mathrm{d}x' \tag{4.2}$$

The quantity A may be a function of x and x'. The distribution function is normalised such that the integral of $f(x,x')$ over phase space yields the number of electrons in the distribution.

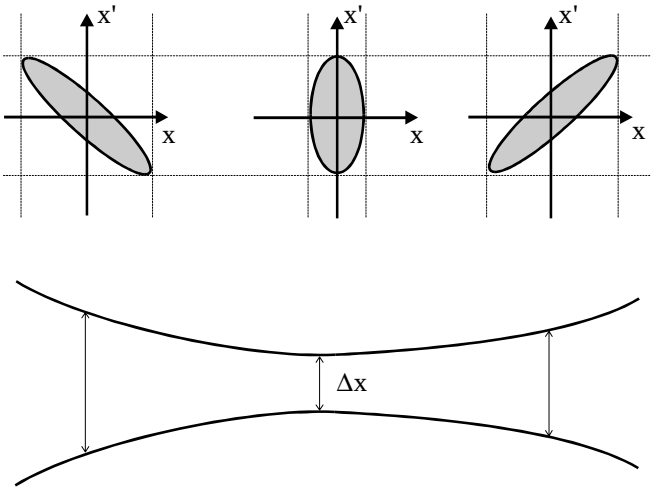

Figure 4.1: The electron distribution in phase space as the electron beam moves through a focus.

The root mean square width of a distribution is defined as $x_{\mathrm{rms}} \equiv \sqrt{\langle x^2 \rangle}$. In the special case of a Gaussian distribution, the root mean square width equals the standard deviation. It is related to the full width at half maximum by $\Gamma_{FWHM} = 2\sqrt{2\ln 2}\, x_{\mathrm{rms}}$.

Consider the *i*-th particle in the distribution. There will be two forces acting on the particle: an external force F_e, and a force F_s which is the force due to the interaction with the other particles. This results in the equation of motion:

$$m\frac{d^2 x^i}{dt^2} = \sum_{i \neq j} F_s^{i,j} + F_e^i \tag{4.3}$$

In order to describe the evolution of the particle beam through phase space, the evolution of the second moments $\langle xx' \rangle$, $\langle x'x' \rangle$ and $\langle xx \rangle$ is needed. Differentiating $\langle xx' \rangle$ with respect to t yields:

$$\frac{d}{dt}\langle xx' \rangle = \int\int \frac{\partial f(x,x')}{\partial t} xx'\, dx\, dx' + \left\langle x \frac{dx'}{dt} \right\rangle + \left\langle \frac{dx}{dt} x' \right\rangle \tag{4.4}$$

If we assume that the distibution function f does not explicitly depend on time, so $\partial f / \partial t = 0$, then the first term in the integral equals zero. Likewise, the time derivatives of the other second moments are:

$$\frac{d}{dt}\langle x'^2 \rangle = 2\left\langle x' \frac{d}{dt} x' \right\rangle \tag{4.5}$$

$$\frac{d}{dt}\langle x^2 \rangle = 2\left\langle x \frac{d}{dt} x \right\rangle \tag{4.6}$$

Substituting the equation of motion (4.3) into these equations yields:

$$\frac{d}{dt}\langle xx' \rangle = \frac{1}{p_z}\langle x(F_s + F_e) \rangle + \frac{p_z}{m}\langle x'^2 \rangle \tag{4.7}$$

$$\frac{d}{dt}\langle x'^2 \rangle = \frac{2}{p_z}\langle x'(F_s + F_e) \rangle \tag{4.8}$$

$$\frac{d}{dt}\langle x^2 \rangle = \frac{2p_z}{m}\langle xx' \rangle \tag{4.9}$$

Now some simplifications will be made regarding the forces on the particles. First, the external force will be allowed to be time-dependent, but it will be assumed to be linear in x: $F_e(t) = -k(t)\,x$. Second, it will be assumed that the self force of the particles is also only linear dependent on x. Then $\langle xF_s \rangle = \alpha \langle x^2 \rangle$ holds, and the above derivatives can be written as the transformation of the matrix

$$\sigma \equiv \begin{pmatrix} \langle x^2 \rangle & \langle xx' \rangle \\ \langle xx' \rangle & \langle x'^2 \rangle \end{pmatrix} \tag{4.10}$$

The σ-matrix is real and symmetric. It will transform according to:

$$\frac{d}{dt}\sigma = F \cdot \sigma + \sigma \cdot F^{\mathrm{T}} \tag{4.11}$$

The matrix F is given by:

$$F = \begin{pmatrix} 0 & p_z/m \\ (-k+\alpha)/p_z & 0 \end{pmatrix} \tag{4.12}$$

For convenience, the matrix transform (4.11) is rewritten as

$$\sigma(t+dt) = M(t) \cdot \sigma(t) \cdot M(t)^{\mathrm{T}} \tag{4.13}$$

where $M(t) = I + F(t)dt$ and I is the identity matrix.

In general, it is not easy to integrate equation (4.13). This is because the self-force of the electrons depends on the electron distribution function f, and consequently the parameter α depends on the elements of the σ-matrix. A special case arises when the influence of the self-force on the beam can be neglected. Then $\alpha = 0$ and (4.13) can be integrated over t to yield:

$$\sigma_{\mathrm{final}} = R \cdot \sigma_{\mathrm{initial}} \cdot R^{\mathrm{T}} \tag{4.14}$$

The matrix R is called the transport matrix and it is equal to:

$$R = I + \int_{t_i}^{t_f} F(t)\, dt \tag{4.15}$$

Likewise, the first moments of the distribution transform according to:

$$\begin{pmatrix} \langle x_2 \rangle \\ \langle x_2' \rangle \end{pmatrix} = R \cdot \begin{pmatrix} \langle x_1 \rangle \\ \langle x_1' \rangle \end{pmatrix} \tag{4.16}$$

If the matrix R does not change the longitudinal velocity of the particles, it depends only on the external force F_{e} and hence only on the transport elements in the beam line. In this case, the determinant of the transport matrix is always unity. For instance, the matrix representing a drift over a length L is given by

$$R_{drift} = \begin{pmatrix} 1 & L \\ 0 & 1 \end{pmatrix} \tag{4.17}$$

and the matrix representing a quadrupole with focal length f and negligible width is given by:

$$R_{quad} = \begin{pmatrix} 1 & 0 \\ -\frac{1}{f} & 1 \end{pmatrix} \tag{4.18}$$

Note that to derive (4.13), no special assumptions regarding the electron distribution in phase space were made. Hence, the matrix formalism applies to any arbitrary beam shape in phase space.

4.1.1 Definition of R.M.S. emittance

The emittance is defined as the area of the electron distribution in phase space. It is a measure of the divergence of the electron beam. It is equal to the square root of the determinant of the σ-matrix (4.10):

$$\varepsilon_x = \sqrt{|\sigma|} = \sqrt{\langle x^2 \rangle \langle x'^2 \rangle - \langle xx' \rangle^2} \tag{4.19}$$

The suffix *x* denotes that the emittance is to be measured in the *x*-*x*' plane. The emittance ε_y in the *y*-*y*' plane is defined similarly. Often, only rotation-symmetric distributions are considered and the suffices *x* and *y* are dropped.

Note that the above definition applies only to electron beams in two-dimensional phase space. In six-dimensional phase space, the emittance is defined as the determinant of a six-by-six beam matrix. To distinguish this definition from (4.19), the 6D-emittance is called the hyperemittance. It is equal to the volume of six-dimensional space that is occupied by the electrons. The hyperemittance is conserved in the absence of self-force in the beam. This is because the determinant of the six-dimensional transport matrices is always unity. Likewise, the determinant of the two-dimensional transport matrices is unity when there is no interaction between the *x*, *y* and *z* directions; this lead to the conservation of the two-dimensional emittance.

In calculating the emittance of a relativistic electron beam, an extra factor $\beta\gamma$ is taken into account. This factor assures that the emittance of the beam is conserved upon velocity changes of the centre of mass of the electron bunch. The normalised emittance is defined as:

$$\varepsilon_{norm} = \beta\gamma\varepsilon \tag{4.20}$$

Another interpretation of the σ-matrix is given by the expansion of

$$\begin{pmatrix} x & x' \end{pmatrix} \cdot \sigma^{-1} \cdot \begin{pmatrix} x \\ x' \end{pmatrix} = 1 \tag{4.21}$$

This is just the equation of an ellipse in phase space. It is useful to rewrite the σ-matrix as:

$$\sigma = \varepsilon \begin{pmatrix} \beta' & -\alpha' \\ -\alpha' & \gamma' \end{pmatrix} \tag{4.22}$$

The α', β' and γ' are called Twiss or Courant-Snyder parameters, and they obey the Courant-Snyder equality $\beta'\gamma' - \alpha'^2 = 1$. In terms of the Twiss parameters, the ellipse in phase space has the equation:

$$\gamma' x^2 + 2\alpha' x x' + \beta' x'^2 = \varepsilon \tag{4.23}$$

The area of this ellipse in phase space is equal to the emittance of the electron beam. The relationship of the Twiss parameters to the ellipse geometry is shown in Figure 4.2.

Hence, the evolution of the r.m.s. width of an arbitrary beam can be described by the evolution of an ellipse in phase space, the equation of which is given by (4.23). It should be stressed that this is only an interpretation of the σ-matrix, and that this interpretation in no way limits the applications of the matrix formalism.

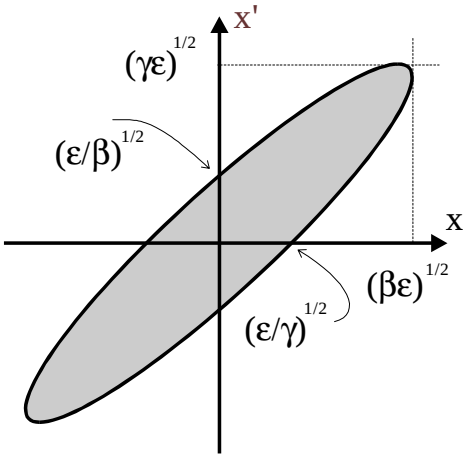

Figure 4.2: The geometrical significance of the Twiss parameters.

It is interesting to note the similarities between the distribution transport theory for electron beams and the matrix transport theory used in geometrical optics. In geometrical optics, a ray at an angle θ with the horizontal, and at a distance r from the optical axis is transported according to:

$$\begin{pmatrix} r_2 \\ \theta_2 \end{pmatrix} = \begin{pmatrix} A & B \\ C & D \end{pmatrix} \cdot \begin{pmatrix} r_1 \\ \theta_1 \end{pmatrix} \tag{4.24}$$

In the same way that an electron beam consists of an ensemble of individually moving electrons, an Hermite-Gaussian optical beam can be considered as an ensemble of geometrical rays [4.1]. The first moments $\langle r \rangle$ and $\langle \theta \rangle$ are defined as in (4.2) and they

transform according to (4.24). One can derive expressions for the transformation of the second order moments $\langle r^2 \rangle$, $\langle \theta^2 \rangle$ and $\langle r\theta \rangle$:

$$\begin{pmatrix} \langle r_2{}^2 \rangle & \langle r_2\theta_2 \rangle \\ \langle r_2\theta_2 \rangle & \langle \theta_2{}^2 \rangle \end{pmatrix} = \begin{pmatrix} A & B \\ C & D \end{pmatrix} \cdot \begin{pmatrix} \langle r_1{}^2 \rangle & \langle r_1\theta_1 \rangle \\ \langle r_1\theta_2 \rangle & \langle \theta_1{}^2 \rangle \end{pmatrix} \cdot \begin{pmatrix} A & B \\ C & D \end{pmatrix}^{\mathrm{T}} \tag{4.25}$$

This is analogous to the matrix transform used in the transport theory of electron beams, as given in (4.14). Furthermore, the M^2-number is defined as:

$$M^2 = \frac{4\pi}{\lambda} \sqrt{\langle r^2 \rangle \langle \theta^2 \rangle - \langle r\theta \rangle^2} \tag{4.26}$$

which is analogous to the emittance of an electron beam, defined in (4.19). The emittance and the M^2-number are analogous, but not identical: one important difference is that the M^2-number is always larger than or equal to unity, whereas the emittance is always larger than zero.

The M^2-number is a measure of the optical beam quality, and it is unity for a diffraction limited first order Hermite-Gaussian mode. It is conserved throughout the beam. The emittance is a measure of the divergence of the electron beam, and is only conserved in the absence of self-force in the beam.

4.2 Emittance measurement techniques

The TEU-FEL beamline transports the electron beam from the linear accelerator to the wiggler. It is shown schematically in Figure 4.3.

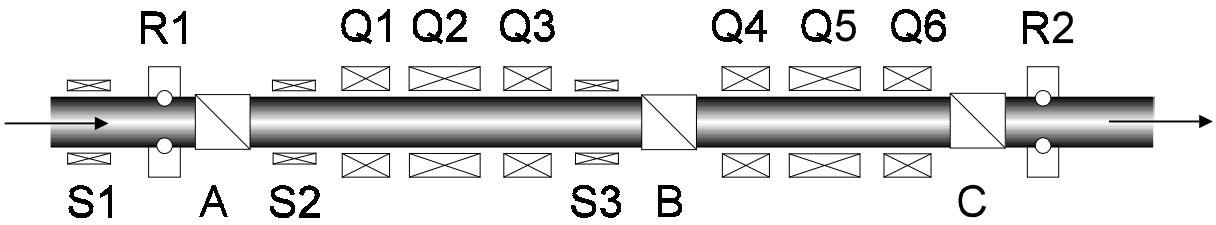

Figure 4.3: A schematic of the TEU-FEL beam line. S - steering coils; R - current monitors; A, B, C - insertion screens; Q - quadrupoles.

Electromagnetic quadrupoles Q are used to focus the electron beam. Such a quadrupole has the property of focusing the electron beam in one direction, and defocusing it in the orthogonal direction. The focal length of the quadrupole can be varied by changing the current through the electromagnets. One can look at a quadrupole as being an astigmatic, variable lens for electron beams.

Sets of steering coils are inserted at the positions S1, S2, S3. These coils can steer the electron beam in both horizontal and vertical directions. The average current of the

beam can be measured at the positions R1 and R2, using a Rogowski coil. To monitor the position and quality of the electron beam, screens can be inserted at the positions A, B and C. These are destructive profile monitors, in the sense that they block the electron beam such that its profile can only be monitored at one position at a time. At the position of screen A, a pepper pot can be inserted into the beam line.

A commonly used insertion screen is a quartz screen, on which the size of the beam is measured by looking at the Cherenkov radiation, generated by the passage of the beam through the screen. Since the Cherenkov light is generated along the path of the electron beam in the medium, the observed beam size is determined by both the actual beam size and the thickness of the quartz screen. Besides this, the scattering of electrons in the medium causes a further broadening of the observed profile. This can be a problem when monitoring small beam profiles.

Another method to measure the beam profile is by means of a scintillating foil. When the beam passes through the foil, the electrons will excite dopant atoms in the foil, which will emit radiation as they decay to their ground states. The method is very sensitive, but since the scintillating foil lacks a good heat transfer it is easily destroyed by large beam peak currents.

A very simple and rugged profile monitor consists of a thin metal foil. If a charged particle passes the boundary between the vacuum and the metal, optical transition radiation (OTR) is generated [4.2]. The moving field of the electron induces a time-dependent polarisation in the medium, that emits radiation. Near the surface, this radiation adds coherently, giving rise to transition radiation. Since it is a surface effect, there is no widening of the observed beam size due to thickness of the screen, as was the case with the quartz screens. However, it is advantageous to choose a thin metal foil to minimise the scattering of electrons in the medium. The X-rays generated by this scattering show up as background noise in the beam profile.

In the TEUFEL beam line, quartz screens, scintillating foils and OTR screens have been used. Unless otherwise stated, OTR screens were used in the experiments described in this chapter. The emittance measurement methods that are described in this chapter are based on the matrix formalism that was derived above. In this matrix formalism, the effect of internal forces was not taken into account; therefore the methods described hereafter are only valid when electon-electron interactions in the beam can be neglected.

4.2.1 Multiple screen methods

The emittance of an electron beam can be determined by measuring the size of the electron beam at several positions along its path. Two methods exist; they are called the two-screen method and the three-screen method. In the beam line, three screens (A, B and C) are present, as can be seen in Figure 4.3. The beam sizes at these positions are denoted by r_A, r_B and r_C respectively. The distance between screens A and B and between screens B and C is L_{AB} and L_{BC}, respectively. In order to do a two-screen emittance measurement, the apparatus is adjusted until the beam size at the screen A is at a minimum. The beam at screen A can be represented by the matrix:

$$\sigma^{\mathrm{A}} = \begin{pmatrix} \sigma_{11}^{\mathrm{A}} & 0 \\ 0 & \sigma_{22}^{\mathrm{A}} \end{pmatrix} \tag{4.27}$$

which is the matrix representing an electron beam in the beam waist[†] . The beam matrix at screen B is:

$$\sigma^{B} = \begin{pmatrix} \sigma_{11}^{A} + L_{AB}{}^{2}\sigma_{22}^{A} & L_{AB}\sigma_{22}^{A} \\ L_{AB}\sigma_{22}^{A} & \sigma_{22}^{A} \end{pmatrix} \tag{4.28}$$

according to (4.14). The only direct measurable quantities in these matrices are the electron beam sizes at the screens: $r_{\mathrm{A}}{}^{2} = \sigma_{11}^{A}$ and $r_{\mathrm{B}}{}^{2} = \sigma_{11}^{\mathrm{A}} + L_{\mathrm{AB}}{}^{2}\sigma_{22}^{\mathrm{A}}$. Substituting the first in the latter expression and solving for σ_{22}^{A} yields:

$$\sigma_{22}^{A} = \frac{r_{\mathrm{B}}{}^{2} - r_{\mathrm{A}}{}^{2}}{L_{\mathrm{AB}}{}^{2}} \tag{4.29}$$

and hence, the emittance ε is, according to (4.19) [4.3]:

$$\varepsilon = \left|\sigma^{\mathrm{A}}\right| = \tfrac{1}{L_{AB}}\sqrt{r_{\mathrm{A}}{}^{2}(r_{\mathrm{B}}{}^{2} - r_{\mathrm{A}}{}^{2})} \tag{4.30}$$

where we have used the property that the off-diagonal elements of the beam matrix are zero in the waist.

In a similar way, one can obtain an expression for the emittance of the beam as a function of the beam size at three positions. In that case, it is no longer necessary to assume a beam waist at one of the screens. The beam matrix at screen A is

$$\sigma^{A} = \begin{pmatrix} \sigma_{11} & \sigma_{12} \\ \sigma_{12} & \sigma_{22} \end{pmatrix} \tag{4.31}$$

The matrices at screens B and C are calculated by transforming this matrix according to (4.14). We find:

$$\sigma^{B} = \begin{pmatrix} 1 & L_{AB} \\ 0 & 1 \end{pmatrix}\begin{pmatrix} \sigma_{11} & \sigma_{12} \\ \sigma_{12} & \sigma_{22} \end{pmatrix}\begin{pmatrix} 1 & L_{AB} \\ 0 & 1 \end{pmatrix}^{T} \tag{4.32}$$

[†] In our experiment, it is not possbile to move the screen into the waist of the electron beam. In stead, the focal length of the quadrupole is adjusted until a minimum spot size on the screen is measured. This introduces a small systematic error since the waist of the beam will not be *on* the screen, but a little bit *before* the screen. This error can be neglected compared to the accuracy of the method.

for the beam matrix at screen B and

$$\sigma^{C} = \begin{pmatrix} 1 & L_{BC} \\ 0 & 1 \end{pmatrix} \begin{pmatrix} 1 & L_{AB} \\ 0 & 1 \end{pmatrix} \begin{pmatrix} \sigma_{11} & \sigma_{12} \\ \sigma_{12} & \sigma_{22} \end{pmatrix} \begin{pmatrix} 1 & L_{AB} \\ 0 & 1 \end{pmatrix}^{T} \begin{pmatrix} 1 & L_{BC} \\ 0 & 1 \end{pmatrix}^{T} \tag{4.33}$$

for the beam matrix at screen C. By realising that $r_{\mathrm{A}}{}^{2} = \sigma_{11}^{A}$, $r_{\mathrm{B}}{}^{2} = \sigma_{11}^{B}$ and $r_{\mathrm{C}}{}^{2} = \sigma_{11}^{C}$, we obtain three equations in three unknowns that can be solved for σ_{11}, σ_{12}, and σ_{22}. The definition (4.19) then yields the emittance:

$$\varepsilon^{2} = -\prod_{i=0}^{1}\prod_{j=0}^{1} \frac{(L_{\mathrm{AB}} r_{\mathrm{C}} + (-1)^{i}(L_{\mathrm{AB}} + L_{\mathrm{BC}}) r_{\mathrm{B}} + (-1)^{j} L_{\mathrm{BC}} r_{A})}{4 L_{\mathrm{AB}}{}^{2} L_{\mathrm{BC}}{}^{2} (L_{\mathrm{AB}} + L_{\mathrm{BC}})^{2}} \tag{4.34}$$

When choosing a method to measure the emittance of an electron beam, one should bear in mind that although the multiple screen methods are easier to do than a quadrupole scan, they yield less accurate results due do the limited amount of acquired data.

4.2.2 Quadrupole scan

In a quadrupole scan, the position of the waist of the electron beam is varied by changing the focal length of a quadrupole. The size of the beam in the focusing direction is measured on a screen A at a fixed distance *L* from the quadrupole, and plotted versus the focal length of the quadrupole. This plot can be used to determine the emittance of the particle beam in the focusing direction of the quad. By changing the direction of the current through the quadrupole, it can be made to focus in the orthogonal direction and hence also the electron phase space area in this direction can be measured.

Since it requires only very simple diagnostic elements, the quadrupole scan technique is a frequently used method to measure the emittance. Usually quadrupoles and screens are already inserted into the beam line for focusing of the beam and observation of the electron beam profile, and therefore it is relatively simple to do a quadrupole scan.

However, a quadrupole scan does not produce an electron phase space plot. This is widely seen as a disadvantage of the method: it only yields the area of the electron in beam phase space, and does not give any information on the exact electron distribution. However, it is also a widespread misunderstanding that the quadrupole scan implicitly assumes an ellipsoid distribution in phase space. In the following, it will be shown that this is not the case.

The basic arrangement for a quadrupole scan consists of a single quadrupole and a screen at the position B, a distance *L* from the quadrupole (Figure 4.3). The electron beam at the quadrupole and at the screen can be described by the matrices σ_{Q} and σ_{B} respectively. The transport of the beam down the line can be described by the matrix transformation:

$$\sigma^{B} = R_{drift} \cdot R_{quad} \cdot \sigma^{Q} \cdot R_{quad}^{T} \cdot R_{drift}^{T} \tag{4.35}$$

The R_{drift} and R_{quad} matrices are as given in (4.17) and (4.18). The size of the beam at the target is given by $x = \sqrt{\sigma_{11}^{\mathrm{B}}}$, where

$$\sigma_{11}^{\mathrm{B}}(f) = 2 \cdot \left(L - \frac{1}{f} L^2 \right) \sigma_{21}^{\mathrm{Q}} + \left(1 - \frac{2}{f} L + \frac{1}{f^2} L^2 \right) \sigma_{11}^{\mathrm{Q}} + L^2 \sigma_{22}^{\mathrm{Q}} \tag{4.36}$$

Differentiating to f yields

$$\frac{d}{df} \sigma_{11}^{\mathrm{B}}(f) = \frac{2L^2}{f^2} \sigma_{21}^{\mathrm{Q}} + \left(\frac{2}{f^2} L - \frac{2}{f^3} L^2 \right) \sigma_{11}^{\mathrm{Q}} \tag{4.37}$$

From now on, the suffix Q will be omitted. Setting $\mathrm{d}\sigma_{11}^{B} / \mathrm{d}f = 0$ and solving for f:

$$f_w = \frac{\sigma_{11} \cdot L}{\sigma_{21} \cdot L + \sigma_{11}} \tag{4.38}$$

This is the focal length of the quadrupole at which the spot size on the screen is a minimum. Note that this does not mean that the focus of the beam is on the screen, in fact, it is somewhat closer to the quadrupole. The minimum spot size during a quadrupole scan is given by:

$$x_{\min}^{2} \equiv \sigma_{11}^{\mathrm{B}}(f_w) = \frac{L^2 \cdot \left(\sigma_{22} \cdot \sigma_{11} - \sigma_{21}^{2} \right)}{\sigma_{11}} = \frac{L^2 \cdot |\sigma|}{\sigma_{11}} \tag{4.39}$$

The expression for $\sigma_{11}^{\mathrm{B}}(f_w)$ can now be rewritten in terms of $x_{\min}$, f_w and ε:

$$x_{\mathrm{target}} \equiv \sqrt{\sigma_{11}^{\mathrm{B}}} = x_{\min} \cdot \sqrt{1 + \left(\frac{L}{x_{\min}} \right)^4 \cdot \left(\frac{\varepsilon}{f_w} \right)^2 \cdot \left(1 - \frac{f_w}{f} \right)^2} \tag{4.40}$$

Using $x_{\min}$, ε, and f_w as fit parameters, this formula can be fitted to the quadrupole scan data to yield the r.m.s. emittance of the electron beam [4.4]. Given equations (4.39) and (4.38) and the definition of ε, the matrix elements σ_{11}, σ_{22} and σ_{12} can be calculated from the fit parameters. The beam phase space ellipse can be constructed from these matrix elements, that describe the electron beam at the position of the quadrupole.

The formula (4.40) follows directly from the electron distribution transport theory, derived earlier in this chapter. Since this theory did not put any constraints on the shape of the electron distribution in phase space, neither does (4.40). This means that in principle, the quadrupole scan technique can be applied to any arbitrary beam shape in phase space. However, since the effect of self-force in the beam was not included in the transport theory, the quadrupole scan is only a valid technique when the electron space charge effects can be neglected.

Figure 4.4 shows the results of a quadrupole scan in which the electron beam was focused in the vertical direction; therefore this scan measures the emittance in the vertical direction. The scan was performed with a bunch charge of 1.5 nC and yields an unnormalised emittance of $1.22\,\pi$ mm mrad. The normalised emittance is $15.5\,\pi$ mm mrad.

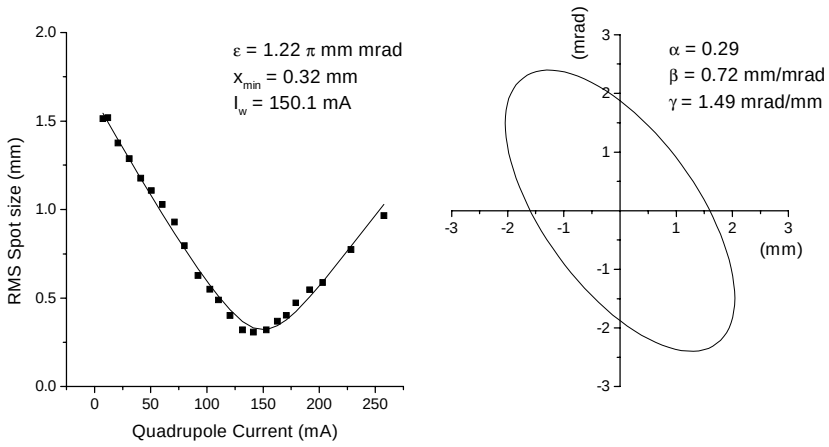

Figure 4.4: Left: The size of the electron beam at position B as a function of the current through quadrupole Q2. The Twiss parameters determined by this scan are used to construct the phase space ellipse in the right graph.

4.2.3 Pepper pot method

When one wishes to determine the phase space distribution of an electron beam, one must measure both the spatial and angular distribution of the electrons. The spatial distribution can be measured directly. The angular distribution can be obtained by looking at the spatial distribution of the electrons after the beam has passed through a known aperture.

A frequently used aperture is the pepper pot, which is a two-dimensional array of holes, drilled into a metal plate. When inserted into the beam, the pepper pot stops most of the beam and allows only small beamlets to pass. The position and size of the beamlets are measured at a screen, some distance downstream of the pepper pot (see Figure 4.5). The size of the beamlets and their mutual distance at the screen is used to calculate the width of the angular distribution of the electrons at the pepper pot.

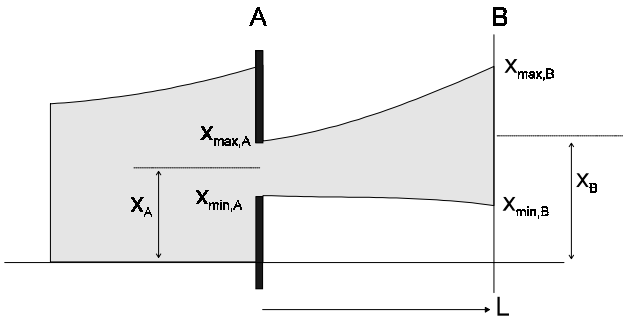

Figure 4.5: The operating principle of the pepper pot. The electron beam (grey) is incident on an aperture that cuts a small part out of phase space.

The pepper pot method will be explained following the arguments of Yamazaki et. al. [4.5]. Consider a beamlet cut out of phase space at the position A in the beamline. The transverse co-ordinate of this beamlet is denoted by x_A, its width is $\delta x_A = x_{\max,A} - x_{\min,A}$ (see Figure 4.6). If the width of the hole is sufficiently small, the shape of this beamlet in phase space can be approximated by a quadrangle. The downleft and upright corners of the area will be denoted as $\left(x_{\min,A}, x'_{\min,A}\right)$ and $\left(x_{\max,A}, x'_{\max,A}\right)$ respectively. This beamlet is transported downstream over a distance L to a screen at position B, where its transverse co-ordinate x_B and width δx_B can be measured on a screen.

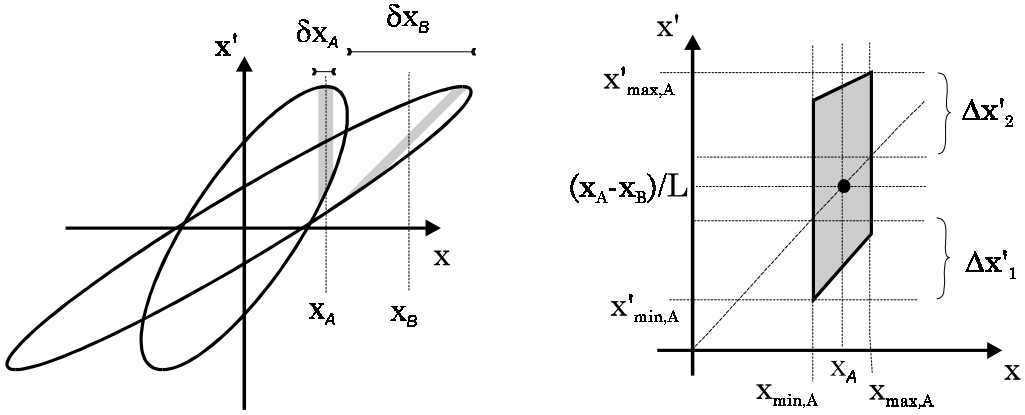

Figure 4.6: The pepper pot slices a small part out of the electron phase space distribution. This part is magnified on the right.

The average of the angular distribution of the beamlet is equal to the inclination of the beamlet path in the beamline, and it is given by $\langle x' \rangle = (x_B - x_A)/L$. The average of the spatial distribution at the pepper pot is given by $\langle x \rangle = x_A$. A line through the origin of phase space and the centre of the beamlet at the pepper pot therefore has the inclination:

$$incl = \frac{\langle x' \rangle}{\langle x \rangle} = \frac{(x_B - x_A)}{L x_A} \tag{4.41}$$

This line is used to determine the positions of the lower and upper limit of the angular distribution:

$$x'_{\min,A} = \frac{(x_B - x_A)}{Lx_A} x_{\min,A} - \Delta x'_1 \tag{4.42}$$

$$x'_{\max,A} = \frac{(x_B - x_A)}{Lx_A} x_{\max,A} + \Delta x'_2 \tag{4.43}$$

The variables $\Delta x'_1$ and $\Delta x'_2$ are as defined in Figure 4.6. The point $(x_{\min,A}, x'_{\min,A})$ is according to the electron distribution transport theory, transferred to

$$\begin{pmatrix} x_{\min,B} \\ x'_{\min,B} \end{pmatrix} = \begin{pmatrix} x_{\min,A} + Lx'_{\min,A} \\ x'_{\min,A} \end{pmatrix} \tag{4.44}$$

A similar relation holds for the point $(x_{\max,A}, x'_{\max,A})$, which is transferred to $(x_{\max,B}, x'_{\max,B})$. The width of the beamlet on the screen at position B is then given by:

$$\delta x_B = x_{\max,B} - x_{\min,B} = \delta x_A \frac{x_B}{x_A} + L(\Delta x'_1 + \Delta x'_2) \tag{4.45}$$

For a sufficient small beamlet, the width of the angular distribution is $\Delta x' = \Delta x'_1 + \Delta x'_2$. If the position and the width of the beamlet at both the pepper pot and the screen are known, the width $\Delta x'$ can be calculated using the above expression. This width will be dependent on x_A, and the plot of $\Delta x'$ versus x_A will yield the electron phase space distribution.

Let us denote the distance between the holes in the pepper pot by *a*. The phase space distribution can be approximated as a number of rectangles with width *a* and height $\Delta x'$. The emittance is calculated by adding the surfaces of these rectangles:

$$\varepsilon = \frac{1}{L} \sum_i a \left(\delta x_{B,i} - \delta x_A \frac{x_{B,i}}{x_{A,i}} \right) \tag{4.46}$$

where the suffix *i* denotes the *i*-th beamlet.

Because it does not make any preliminary assumptions on the shape of the distribution in phase space, the pepper pot method can be used to measure any arbitrary electron phase space distribution. However, for some pathological distributions (for instance, a

C-shaped or an O-shaped distribution) the interpretation of the results might become troublesome.

The size of the pepper pot holes and their mutual distance must be chosen such that the beamlets do not overlap at the screen. This limits the density of holes in the pepper pot, and thus the accuracy of the reconstructed phase space distribution. Furthermore, the pepper pot method cannot always be used for emittance measurements on high energetic electron beams. In order to stop a high-energetic electron beam, the plate in which the pepper pot holes are drilled must be sufficiently thick. However, a hole drilled into a thick plate acts as an emittance filter because only the part of the beam with sufficient low divergence can pass through the hole. This poses an upper limit to the emittance that can be measured with a pepper pot.

For ease of construction, we have chosen to use a pepper pot that does not consist of an matrix of holes, but of an array of slits. The slits are sawed into a 2 mm thick tungsten plate, which is sufficient to stop a 6 MeV electron beam. There are 9 slits in the pepper pot, they are spaced 1 mm apart and they are 80 μm wide. With this type of pepper pot it is possible to measure the emittance in only one direction. If the size of the electron beam at the pepper pot is 10 mm (such that all the slits are illuminated) then the maximum measurable emittance is 590 π mm mrad. The results of the pepper pot technique are displayed in Figure 4.7. The unnormalised emittance here is ε = 1.48 π mm mrad, at a bunch charge of 1.4 nC. The normalised emittance is 18.8 π mm mrad.

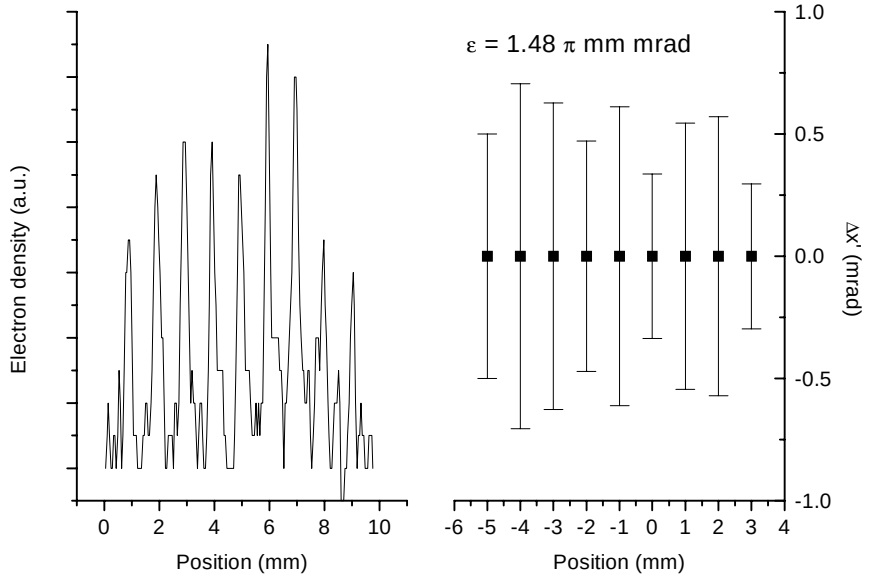

Figure 4.7: An emittance measurement using the pepper pot. The left graph displays the transverse electron distribution on a scintillating foil. The right graph represents the calculated phase space distribution.

4.2.4 Phase space tomography

In 1917 the Austrian mathematician Radon theoretically demonstrated the reconstruction of a distribution from the infinite set of its projections. Tomographic imaging exploits this theorem to reconstruct two-dimensional distributions from a finite set of one-dimensional projections. This technique is used widely in medicine (Nuclear Magnetic Resonance imaging and Positron Emission Tomography scans), oceanography and geology. Recently, tomographic techniques were used to reconstruct the interior of a 2,500 year old Egyptian mummy [4.6].

Conceptually, tomography can be understood as follows. Think of holding in your hand a non-transparent object. You can determine what the object looks like from the outside by looking at it, and then rotating it over 180 degrees to get a look at the back side. If the object were transparent you could also determine the internal structure of the object. However, if you want to get a good image of the interior of the object, it is not sufficient to just look at the front and back sides of the object; you required several points of view to see what the internal structure is like.

This is the basis of computerised tomography: An object is viewed in transmission at several angles, and the images are combined to reconstruct the interior structure of the object. For instance, when the Egyptian mummy was studied, it was photographed from all sides using an X-ray camera. The consecutive photographs yielded the projection of the interior of the mummy, and they were used to calculate a 3D image of the interior. The infinite set of projections of an image is called the Radon transform of an image. Several computational methods exist to reconstruct the original image from its Radon transform.

The set-up for a phase space tomography experiment is identical to that for a quadrupole scan (see Figure 4.3) The position of the electron beam waist is varied by changing the focal length of the quadrupole Q. By looking at the spot profile on the screen B, the projection of the transverse phase space distribution can be measured directly. In the remainder of this section, it will be shown that varying the focal length of the quadrupole has the effect of rotating the beam in phase space over some angle θ, followed by a multiplication by a factor s. If the spot profile at the screen is recorded as a function of the quadrupole focal length, it is possible to reconstruct the original phase space distribution from the collection of images [4.7, 4.9].

Consider an electron distribution $f(x,x')$ at a position z in the beam line. The projection of this distribution on the spatial co-ordinate can be expressed as a two-dimensional integral over phase space:

$$g(x_0) = \int\int f(x,x')\,\delta(x_0 - x)\,\mathrm{d}x\,\mathrm{d}x' \tag{4.47}$$

Here δ is the Dirac delta-function. This electron distribution will be transported down the beam line to a screen B, and the matrix describing this transport will be denoted by

R. In the phase space tomography experiment, the transport matrix *R* consisted of a drift section L_1, a quadrupole with power $P = 1/f$, followed by another drift section L_2:

$$R = \begin{pmatrix} 1 - PL_2 & L_1 + L_2 - PL_1L_2 \\ -P & 1 - PL_1 \end{pmatrix} \tag{4.48}$$

The vectors $\vec{\zeta}$ and $\vec{X}$ are defined as:

$$\vec{\zeta} = \begin{pmatrix} R_{11} \\ R_{12} \end{pmatrix};\ \vec{X} = \begin{pmatrix} x \\ x' \end{pmatrix} \tag{4.49}$$

Using these definitions, the projection (4.47) can be rewritten as a one-dimensional integral over vector space:

$$g(x_0) = \int f(\vec{X})\,\delta\left(x_0 - \vec{X}\cdot\hat{x}\right)d\vec{X} \tag{4.50}$$

where $\hat{x}$ is the unit vector in the *x*-direction. The above expression gives the projection of the electron distribution at one point in the beam line. But because we wish to determine the internal structure of the electron distribution, one projection is not enough. We can calculate the projection of the distribution at another point in the beam line by transporting the electron distribution using the transport matrix *R*. This yields:

$$\breve{f}(x_0, \vec{\zeta}) = \int f(R\cdot\vec{X})\,\delta\left(x_0 - \vec{\zeta}\cdot\vec{X}\right)d\vec{X} \tag{4.51}$$

Equation (4.51) is the Radon transform of the electron distribution under an arbitrary rotation in phase space. There are standard imaging programs available that can calculate the original distribution from the Radon transform, but these programs assume that the Radon transform was performed under a Cartesian rotation. So it will be advantageous to relate (4.51) to the Radon transform under a Cartesian rotation.

It is possible to rewrite the matrix *R* as the product of a multiplication matrix and a Cartesian rotation matrix:

$$R = \frac{1}{s}\begin{pmatrix} s^2 & 0 \\ t^2 & 1 \end{pmatrix}\cdot\begin{pmatrix} \cos(\theta) & \sin(\theta) \\ -\sin(\theta) & \cos(\theta) \end{pmatrix} \tag{4.52}$$

In terms of the transport matrix *R*, the scaling factors *s* and *t* and the rotation angle θ are given by:

$$\tan(\theta) = R_{12}/R_{11} \tag{4.53}$$

$$s^2 = R_{11}^2 + R_{12}^2 \tag{4.54}$$

$$t^2 = R_{11}R_{21} + R_{22}R_{12} \tag{4.55}$$

The Cartesian rotation vector is given by $\vec{\xi} = (\cos(\theta), \sin(\theta))$. The relation between an arbitrary rotation vector $\vec{\zeta}$ and the Cartesian rotation vector $\vec{\xi}$ is $\vec{\zeta} = s\vec{\xi}$. Substituting this in (4.51) yields:

$$\begin{aligned} \int f(R\cdot\vec{X})\,\delta(x_0 - \vec{\zeta}\cdot\vec{X})\,d\vec{X} &= \int f(R\cdot\vec{X})\,\delta\left(x_0 - s\vec{\xi}\cdot\vec{X}\right)d\vec{X} \\ &= \frac{1}{s}\int f(R\cdot\vec{X})\,\delta\left({}^{x_0}\!/_{s} - \vec{\xi}\cdot\vec{X}\right)d\vec{X} \end{aligned} \tag{4.56}$$

where the identity $\delta(ax) = \delta(x)/|a|$ has been used. This can be written as:

$$\breve{f}(x_0, \vec{\zeta}) = \frac{1}{s}\,\breve{f}\left({}^{x_0}\!/_{s}, \vec{\xi}\right) \tag{4.57}$$

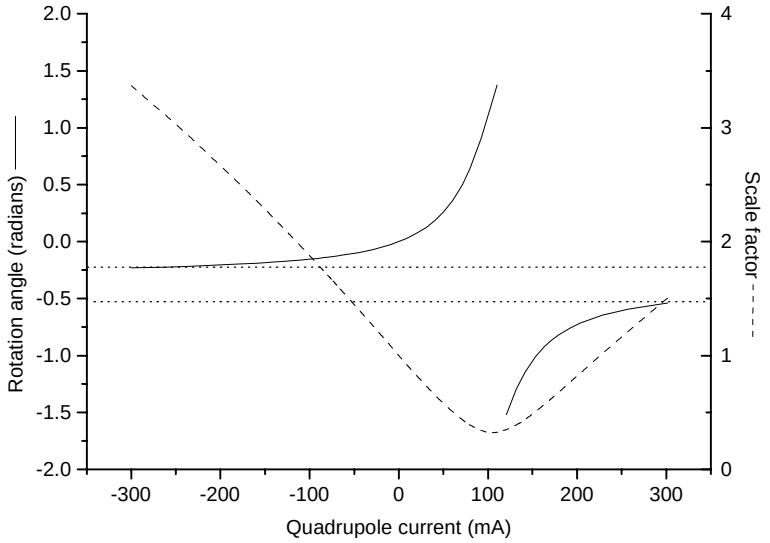

Figure 4.8: The scaling factor and rotation angle as a function of quadrupole current in a PST scan.

Equation (4.57) is called the Radon transform scaling law, and it relates the Radon transform by an arbitrary rotation to the transform by a Cartesian rotation. The inverse of the Radon transform under a Cartesian rotation is [4.7, 4.9]:

$$f\left(\vec{X}\right) = \frac{1}{2}\int\int\int |k|\, e^{-2\pi i k\left(p - \vec{\xi}\cdot\vec{X}\right)} \breve{f}\left(p, \vec{\xi}\right) dk\, dp\, d\vec{\xi} \tag{4.58}$$

The elements of the transport matrix R depend on the focal length of (and hence on the current through) the quadrupole, and so do the rotation angle θ and scaling factor s. It is preferred to choose the quadrupole current settings such that the angle θ rotates a full π radians, thus obtaining images from every angle. Due to the limited current through the quadrupole and the finite length of the beamline this is not always possible, as can be seen in Figure 4.8. In this special case, there is a "blind spot" between θ = -0.23 rad and θ = -0.53 rad. The occurrence of such a blind spot in the acquired data leads to distortions in the reconstructed image.

When doing a phase space tomography experiment, one must record the beam profiles at the screen A as a function of the quadrupole focal length. Then, the rotation angle θ and the scaling factor s can be calculated according to (4.53) and (4.54), respectively. Using the scaling factor, the measured beam profiles can be converted into the Radon transform of the electron distribution under a Cartesian rotation. This is done using the scaling law (4.57). The phase space distribution can then be reconstructed using standard tomographic programs.

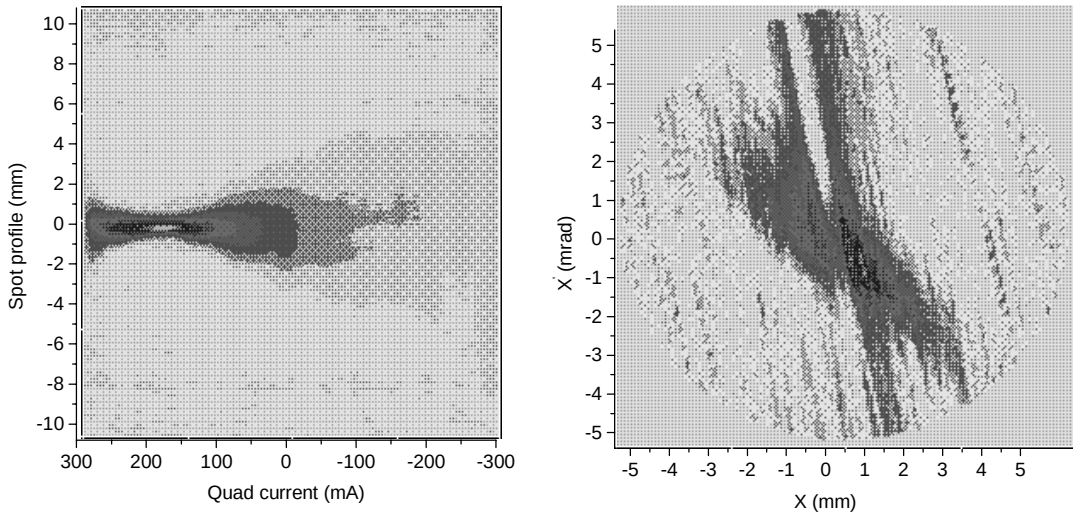

Figure 4.9: Phase space tomography on a relativistic electron beam. The left image represents the beam profile at position B as a function of the current through quadrupole Q2. In the right image the reconstructed phase space distribution is presented.

Figure 4.9 shows the result of such an experiment. The unnormalised emittance of this distribution is $3.8\,\pi$ mm mrad, which yields a normalised emittance of $48.1\,\pi$ mm mrad. The bunch charge during this experiment was 1.5 nC. The "disc" around the central spot is an artefact, created by background noise in the initial data. The reconstructed phase space distribution can be compared with the phase space ellipse that was determined using the quadrupole scan in Figure 4.4. On the top left and bottom right part of the distribution there are two dark patches: These are the distortions that are caused by the incomplete range of the rotation angle. They are at right angles to the blind spot between θ = -0.23 rad and θ = -0.53 rad.

4.3 Electron bunch length

In the previous sections, the attention has been focused on the transversal phase space. A transverse phase space plot yields information on the transverse dimensions and divergence of the electron beam; likewise a longitudinal phase space plot gives information on the longitudinal co-ordinate and velocity of the bunch. The longitudinal co-ordinate is frequently measured in either time or radio-frequency phase φ; the longitudinal momentum is measured in units of energy with respect to the centre of the bunch.

The energy spread of an electron bunch can be determined by using a spectrometer positioned at the end of the beam line. In contrast, it is not so easy to measure the duration of a bunch. This is because this duration is of the same order of magnitude as the drive laser pulse duration, which is between 15 - 30 ps. The Rogowski coils that are used to measure the electron bunch charge have a bandwidth of ≈ 1 GHz, which is an order of magnitude too low to resolve the shape of the bunch. The duration of the pulse also poses problems to the measurement of the signal on an oscilloscope.

We must therefore find alternative methods to measure the electron bunch length. In this section, it will be measured using two independent methods: a tomographic method applied to longitudinal phase space, and streak camera measurements of the OTR.

4.3.1 Streak camera measurements

The electron bunch length can be determined more easily by measuring the duration of the light pulse produced at one of the OTR screens. This is possible because the OTR is produced instantaneously. The electron beam is directed to the OTR screen at position B using two sets of steering coils and the quadrupole triplet. The light produced at the screen is imaged onto the entrance slit of the streak camera using two lenses.

The OTR has a very wide spectral range (extending from the deep infrared to far into the ultraviolet region of the spectrum). Consequently the OTR pulse duration can be substantially increased due to dispersion in the imaging optics. Since the sensitivity of the streak camera extends from the visible to the infrared part of this spectrum, the dispersion leads to an error in the pulse duration measurement. By using a band pass

filter to decrease the spectral width of the incident OTR, and comparing the resulting pulse duration with the duration of the unfiltered pulse, the magnitude of the dispersion can be estimated.

The dispersion broadening is measured to be 23 ps. This number is used to deconvolve the measured pulse width into the actual pulse width and the dispersion broadening. The convolution function is assumed to be Gaussian; for example a 30 ps electron pulse will be dispersion broadened to 38 ps, which is an increase of 20 %. Furthermore, the measured pulse length is increased by the finite width of the entrance slit and the trigger noise; these increments are respectively 10 ps and 5 ps. The actual measurements presented in this section were performed without the use of filters, to ensure a good signal to noise ratio. The numbers given have been corrected for dispersion broadening, time resolution broadening and trigger noise.

The electron bunch length has been measured as a function of the total bunch charge, and as a function of the transverse charge density. If the electron bunch is injected into the accelerator at the optimum phase, the bunch duration τ obeys the phenomenological equation [4.8]:

$$\tau = \tau_0 + a_1 \left(\frac{q}{A} \right)^{3/4} \tag{4.59}$$

Here τ_0 is the duration of the ultraviolet drive laser pulse; q the charge in an electron bunch, A the area of the drive laser on the photo cathode surface and a_1 a fit parameter.

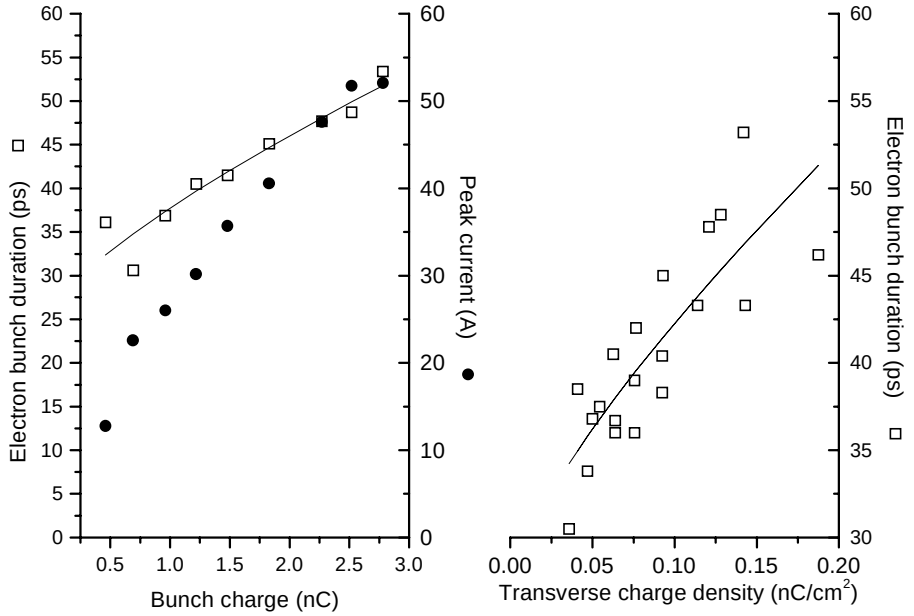

Figure 4.10: The electron bunch length and the peak current as a function of bunch charge (left) and transverse charge density (right).

In the left graph of Figure 4.10 the electron bunch length is given as a function of the charge of the bunch. During this measurement, the ultraviolet laser pulse duration was 29 ps. The injection phase and the transverse current density were kept constant. The data are fitted to (4.59), which yields an interception of 26 ps. The average lengthening of the electron bunch is 8.3 ps/nC. Also plotted in this graph is the peak current, which calculated by dividing the bunch charge by the bunch duration. The maximum current in this experiment is 50 A. The right graph shows the electron bunch length as a function of transverse current density. These data are also fitted to (4.59), which yields a value τ_0 = 27 ps.

4.3.2 Longitudinal phase space tomography

In a radio-frequency linear accelerator, a bunch of electrons is accelerated using a standing electromagnetic wave. This electromagnetic wave can be described as

$$E(t,z) = E_0 f(z) \sin(\omega t) \tag{4.60}$$

Since the accelerating field is time-dependent, the ultimate energy of an electron will depend on the moment at which it was injected into the accelerator. This moment is called the injection phase φ of the electron. Experimentally, the injection phase is varied by changing the phase of the RF field in the accelerator with respect to the phase of the mode locked laser pulse. The dependence of the electron energy U_e on the injection phase is given by

$$U_e = U_{\max} \cos(\varphi - \varphi_0) \tag{4.61}$$

where in our case is U_{max} = 6 MeV. The electron energy will be at a maximum if the electron is injected at the optimum phase φ_0. If, in stead of a single electron, an electron bunch with width $\delta\varphi$ is injected into the accelerator, then the spread in injection phase will give rise to a variation in electron energy. When the injection phase φ is varied, the orientation of the electron distribution in (U, φ) space will change. Near the centre of mass of the bunch, the electrons will be distributed along a line with inclination:

$$\tan\theta \equiv \frac{dU_e}{d\varphi} = -U_{\max} \sin(\varphi - \varphi_0) \tag{4.62}$$

The angle θ can be interpreted as a rotation angle: by changing the injection phase of the electron bunch, the electron density distribution is rotated in longitudinal phase space. A tomographic experiment in longitudinal phase space is performed by rotating the electron distribution in (U, φ) space and measuring the projection of the distribution on the U-axis using a spectrometer. The energy distribution is measured as a function of the injection phase, after which tomographic techniques are applied to the data to find the original longitudinal phase space distribution [4.10].

The injection phase can only be varied over a small angle around φ_0, typically $\Delta\varphi = 0.30$ radians. If the injection phase is tuned beyond this span, the electron beam current drops significantly due to the loss of electrons in the accelerator. Since the value of θ depends on the value of U_{max}, the span of the rotation angle can be selected by suitably choosing the units of U_{max}. However, as was the case with the transverse phase space tomography experiments, it is not possible to obtain a full π radians rotation. There is always a blind spot in the acquired data, that leads to distortions in the reconstruction of the phase space distribution. The size of this blind spot depends on the units of U_{max}.

Figure 4.11 shows the result of a longitudinal phase space tomography experiment. The left graph shows the electron energy spectrum as a function of injection phase. For the phase $\varphi = \varphi_0$ degrees, the energy spread is a minimum and equal to $\Delta U / U = 0.4$ %. In the right graph, the sinusoidal electron distribution is clearly recognisable. The duration of the electron bunch in this distribution is 38 ps.

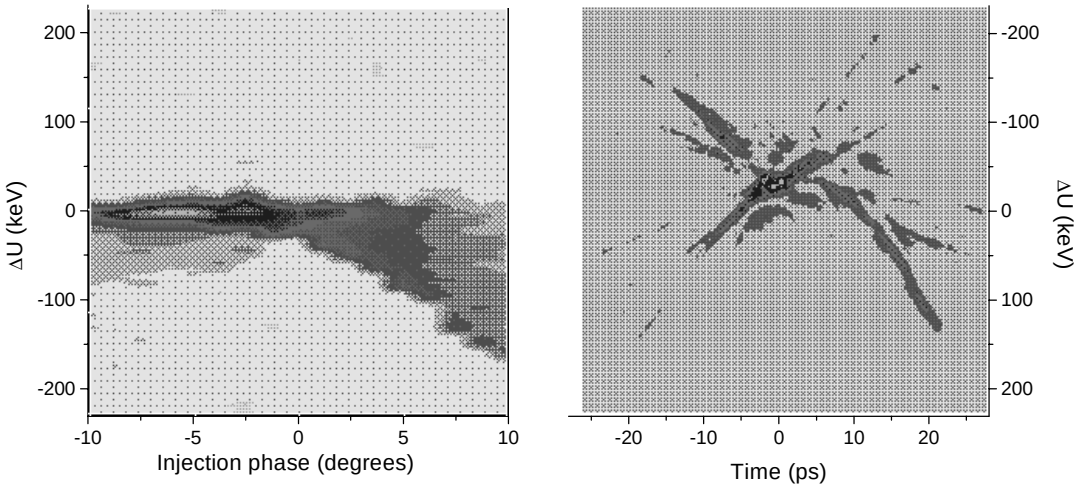

Figure 4.11: Longitudinal phase space tomography. On the left, the energy spectrum of the electron bunch is shown as a function of the injection phase. The right picture represents the reconstructed distribution in (U,t) space. The projection of this distribution on the time axis has a full width half maximum of 38 ps.

4.4 Brightness of the electron beam

The bunch charge during the emittance measurements is approximately 1.5 nC, which means according to Figure 4.10 that the peak current was approximately 40 A. Hence, the brightness of the electron beam is calculated as $B = 53.7\ A/\pi^2\ mm^2\ mrad^2$. In Table 4.1, the characteristic parameters of the TEUFEL electron beam are compared with parameters of other, existing radio-frequency accelerators.

	CEA	*Boeing*	*AFEL*	*CERN*	*TEUFEL*
Energy (MeV)	1.4	5	13	4.1	6
Energy spread (%)	1.9	0.8	0.3	0.1	0.4
Emittance (π mm mrad)	25	9	2.1	52	1.22
Peak current (A)	19	91	95	760	40
Brightness (A/π^2 mm^2 $mrad^2$)	0.06	2.2	43	0.6	53.7

Table 4.1: Electron beam parameters of some existing radio-frequency accelerators (after [4.11]).

4.5 Conclusions

The emittance of the electron beam has been measured using three different techniques: the pepper pot, the quadrupole scan and phase space tomography. There are discrepancies between the results obtained with these various techniques. The emittances measured with the pepper pot and the quadrupole scan (respectively 1.48 π mm mrad and 1.22 π mm mrad) differ by 20 %. This difference is probably caused by changes in the experimental condition, e.g. alignment of the drive laser beam on the cathode. The emittance determined using phase space tomography is a factor 3 larger than that determined with the quadrupole scan. Since the data used in these techniques was recorded simultaneously, this difference can not be attributed to changes in the experimental condition.

We therefore conclude that the reconstruction process does not yield an accurate representation of the transverse electron phase space distribution. The distortions in this distribution are in all likelihood caused by the blind spot in the rotation angle, as was demonstrated in Figure 4.8. With the present equipment, it is not possible to eliminate this blind spot. It is, however, rewarding to see that the shape and orientation of the electron distribution in Figure 4.9 matches that of the phase space ellipse measured by the quadrupole scan in Figure 4.4.

Both the quadrupole scan and the multi-screen methods only give an indication of the electron phase space distribution. Although in theory they are applicable to any arbitrary phase space distribution, they are best fit for Gaussian-like distributions. If large irregularities are present in the distribution, then these methods will yield too large an emittance. In these cases, the distribution is best determined with a pepper pot, but as mentioned before, the interpretation of the pepper pot measurements might cause problems.

Finally, we should mention that all methods are based on the beam matrix transport theory, derived at the beginning of this chapter. In this theory, the result of self-force in the beam was neglected. Therefore, the results of all methods can be influenced by self-forces in the electron beam. The pepper pot is least influenced by the electron space charge since it slices out small beamlets that have relatively low charge. However, at high current densities also the pepper pot method will yield inaccurate results due to the interaction between the electrons in the bunch.

The electron bunch length was determined using streak camera measurements of the OTR. It was found that the bunch length increases with bunch charge, an effect caused by the self-interaction of the bunch. The increase in bunch length is shown to scale as the ¾-power of the transverse charge density. The result of the longitudinal phase space tomography experiment is in reasonable agreement with the streak camera measurements.

4.6 References

4.1 A.E. Siegman; "New developments in laser resonators", SPIE **1224** (1990) p2 – 14.

4.2 J.D. Jackson, *Classical Electrodynamics*, 2nd Ed., J. Wiley & Sons, Inc., New York (1975), ISBN 0-471-43132-X.

4.3 B.E. Carlsten, "HIBAF two screen emittance measurements and the effect of magnetic field on the cathode", LANL research memorandum (1990).

4.4 B.E. Carlsten, J.C. Goldstein, P.G. O'Shea and E.J. Pitcher "Measuring emittance of nonthermalized electron beams from photo injectors", Nucl. Instr. & Meth. in Phys. Res. A **331** (1993) p791 – 796.

4.5 Y. Yamazaki, T. Kurihara, H.Kobayashi, I. Sato and A. Asami, "High-precision pepper-pot technique for a low-emittance electron beam", Nucl. Instr. & Meth. in Phys. Res. A **322** (1992) p139 – 145.

4.6 C. Baldock, S. Hughes, D. Whitaker, R. Davi, J. Taylor, A.J. Spencer, A. Sofat and K. Tonge, "3D reconstruction of ancient Egyptian mummy using X-ray computer tomography" , Scope **3**, 2 (1994) p21 – 24.

4.7 C.B. McKee, P.G. O'Shea and J.M.J. Madey; "Phase space tomography of relativistic electron beams", Nucl. Instr. & Meth. in Phys. Res. A **358** (1995) p264 – 267.

4.8 D.C. Nguyen; private communication.

4.9 C.B. McKee, *Creation, transport and measurement of bright relativistic electron beams*, thesis (1994) Duke University.

4.10 E.R. Crosson, K.W. Berryman, B.A. Richman, T.I. Smith, R.L. Swent; "The determination of an electron beam's longitudinal phase space distribution through the use of phase-energy measurements", Nucl. Instr. & Meth. in Phys. Res. A **375** (1996) p87 – 90.

4.11 C. Travier; "An introduction to photo-injector design", Nucl. Instr. & Meth. in Phys. Res. A **340** (1994) p26 – 39.

5. Experiments with a Compton FEL

The experimental set-up used in the first stage of the TEU-FEL project is described. The first lasing experiments are described, including the effects of the de-tuning of the laser cavity. The effect of the transverse mode structure inside the resonator is explained, and it is demonstrated experimentally by measuring the wavelength spectrum of the free electron laser radiation.

5.1 First stage of the TEU-FEL project

In the first stage of the TEU-FEL project [5.1], a 6 MeV electron beam is injected into a planar wiggler that is placed inside an optical resonator. The wiggler has 50 periods with a period length of 25 mm [5.2]. It has a gap of 8 mm and a peak magnetic field of 0.7 T, which means a K-value of about unity. The beamline inside the wiggler has an inner diameter of 6 mm so that it will act as an overmoded waveguide for the FEL radiation. After the wiggler there is a tapered section in the vacuum tube which is 40 cm long and brings the 6 mm diameter to 25 mm. A schematic of the last end of the beamline is shown in Figure 5.1.

The optical cavity has a plane mirror just upstream the wiggler. It has a diameter of 6 mm with a 2 mm hole in it through which the electron beam can enter the wiggler section. The downstream mirror is also a plane one and has a diameter of 25 mm with a 12 mm hole in it. This hole is used by the electron beam to leave the resonator, and for outcoupling of the radiation. The downstream mirror can be moved over a distance of about 1 cm to allow for cavity length tuning.

The FEL can be switched on and off by changing the length of the optical cavity. The required distance between the two mirrors L_{cav} is given by the repetition frequency of the electron bunches f_{eb} and the group velocity of the radiation v_{gr}:

$$L_{cav} = v_{gr} / 2 f_{eb} \tag{5.1}$$

If the above condition is fulfilled, the FEL radiation pulse arrives at the front mirror at the moment that the next electron bunch arrives. Then there is maximum overlap between the electron pulses and the radiation pulse, a situation that gives rise to maximum gain and consequently maximum FEL output. If the cavity is sufficiently detuned, i.e. the radiation and electron micropulses do not overlap on consecutive round trips, there is not sufficient gain and no FEL output.

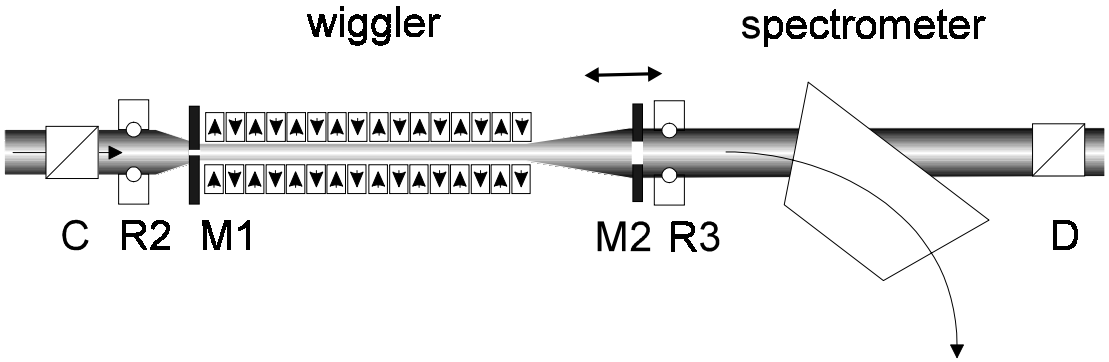

Figure 5.1: The end part of the TEU-FEL beamline, consisting of the wiggler inside an optical cavity and the electron spectrometer. C and D: insertion screens, R: Rogowski coils, M: mirrors.

After leaving the cavity, the electron and radiation pulses co-propagate until they are separated by a 90^o spectrometer, that is used to measure the electron energy spectrum. After the spectrometer, the FEL radiation is coupled out of the vacuum tube using a metal foil mirror (identical to the insertion screens used in the emittance measurements in Chapter 4) and a poly-ethylene window. This set-up allows simultaneous measurement of optical output and the kinetic energy spectrum of the electron beam.

5.2 First lasing experiments

The TEU-FEL experiment achieved lasing for the first time on August 23, 1995 [5.3]. Lasing was confirmed by examining the energy spectrum of the electrons. If the FEL is operating, the electron energy spectrum is affected in two ways: the width of the energy spectrum is increased, and the mean electron energy decreases. These effects will be clarified and demonstrated in this section.

As was mentioned in Chapter 1, the interaction between the electrons and the ponderomotive potential causes some electrons to decelerate and others to accelerate, dependent on their position in the ponderomotive potential. The FEL interaction effectively increases the energy spread of the electron beam, an effect that has been observed experimentally. For this purpose, the tuning of the cavity length has been used to switch our free electron laser on and off.

Figure 5.2 shows the energy spread of the electrons at two different settings of the cavity length. The left graph shows the energy spectrum when no FEL output was observed. In the right graph, the length of the cavity is tuned to fulfil condition (5.1). Under these circumstances, FEL output was observed at screen D and there is a noticeable increase in the energy spread of the electrons.

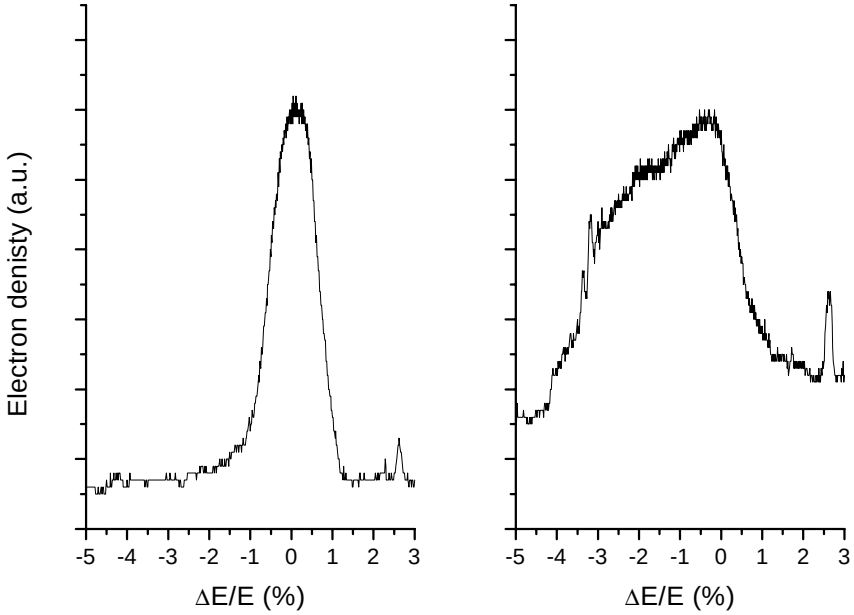

Figure 5.2: Typical energy spectra of the electron beam when there is no lasing (on the left) and when there is maximum output (on the right).

As the electrons interact with the ponderomotive potential, they transfer energy to the radiation wave. The maximum efficiency of this energy transfer is inversely proportional to the number of wiggler periods N_w [5.4]:

$$\eta = \frac{1}{2N_w} \tag{5.2}$$

In the case of a 50-period wiggler, the maximum FEL efficiency is approximately 1 %. In Figure 5.3 the mean electron energy is plotted as a function of the length of the optical cavity. For comparison, also the FEL output power is plotted in this graph. By comparing the two graphs in Figure 5.3, we see that an increase in the FEL output is accompanied by a decrease in the mean electron energy. The downward shift in mean electron energy is 1.2 %, which is approximately equal to the FEL saturation level as given by (5.2). Together with the increase in energy spread observed in Figure 5.2, this confirms the lasing of TEU-FEL.

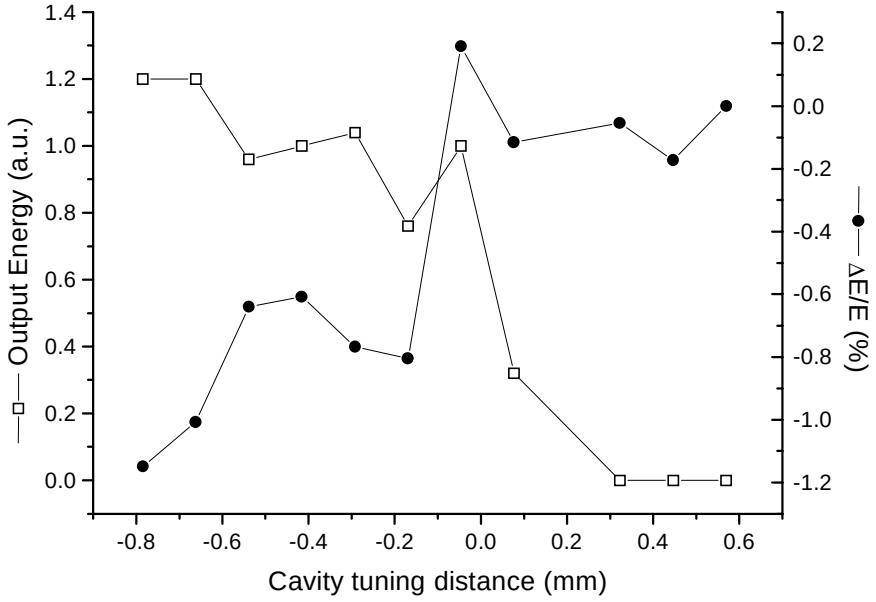

Figure 5.3: The shift in mean electron energy as a function of the cavity tuning distance, compared with the output energy as a function of the same.

5.3 Slippage and lethargy

When an electron pulse travels through the wiggler, it generates an optical pulse that co-propagates with the electrons. Usually, the radiation pulse will travel at a higher velocity that the electron pulse. This causes the radiation at the front of the pulse to move into a region where no electrons are present. This effect is known as slippage. The FEL resonance condition shows that the radiation pulse will slip a length

$$L_s = N_w \lambda_r \tag{5.3}$$

When the slippage length L_s is comparable to the electron pulse length L_e, the slippage will have an important effect on the evolution of the radiation pulse. In the case of TEU-FEL, the radiation wavelength can be tuned between $\lambda_r = 200\ \mu m$ and $\lambda_r = 500\ \mu m$, which means a slippage length between 10 mm and 25 mm. The duration of the electron pulse varies between 20 ps and 60 ps, corresponding to a bunch length between $L_e = 6$ mm and $L_e = 18$ mm.

In an FEL, the gain depends on the position of the electron pulse in the wiggler. This is because at the entrance of the wiggler, the electron distribution in the ponderomotive potential is random, which means zero gain. As the electrons travel towards the end of the wiggler, they bunch at a ponderomotive phase $\zeta < \pi$, and the gain increases. However, at the rear end of the wiggler the optical pulse has slipped ahead of the electron pulse by a length L_s, and consequently only the rear part of the optical pulse is amplified. This results in a shift of the centre of the radiation pulse to the rear end,

which effectively reduces the velocity of the pulse. This effect is known as laser lethargy.

In an oscillator configuration the optical pulses interact with fresh electron pulses on each successive pass through the cavity. Thus the effects at the end of the radiation pulse accumulate, and the slippage effects become measurable for electron pulses that are large compared to the slippage length. The main effect of slippage and lethargy is the sensitivity of the FEL output to a de-tuning of the cavity from synchronism. This effect will be demonstrated by means of numerical calculations and some experiments.

5.3.1 Dimensionless equations of motion

To describe the equations of motion of the electrons in the ponderomotive potential, and the evolution of the radiation field, it is useful to use the dimensionless co-ordinates [5.4, 5.5]:

$$\tau = ct/L_w \tag{5.4}$$

$$\vartheta = (z - ct)/N_w\lambda_r \tag{5.5}$$

$$\mu = 4\pi N_w (\gamma - \gamma_{res})/\gamma_{res} \tag{5.6}$$

$$\varepsilon = 4\pi \frac{KeL_w N_w}{\gamma_{res}^2 mc^2} \left(J_0(\xi) - J_1(\xi)\right) E \tag{5.7}$$

$$j_e = 2\pi \frac{K^2 eL_w^2 N_w}{\varepsilon_0 \gamma_{res}^3 mc3} \left(J_0(\xi) - J_1(\xi)\right)^2 J_e \tag{5.8}$$

Here L_w, N_w, λ_r, K, J_e, E and γ are as defined in Chapter 1. The parameter ξ depends only on the wiggler parameter K and is defined in (1.14). The variable τ is the dimensionless variable of time, which is normalised to the time required by the radiation pulse to travel through the wiggler. ϑ is the position in the electron bunch, measured relative to the centre of mass of the bunch and normalised to the slippage length L_s. The energy μ is measured relative to the resonance energy γ_{res} and normalised to the bandwidth of the FEL. The parameters ε and j_e correspond respectively to the normalised optical electric field and the normalised current density.

Consider an ensemble of N_e electrons. The equations of motion of the n-th electron can be written in terms of the dimensionless variables:

$$\frac{d\mu_n}{d\tau} = \mathrm{Re}\left(i\varepsilon\, e^{i\zeta_n}\right) \tag{5.9}$$

$$\frac{d\zeta_n}{d\tau} = \mu_n \tag{5.10}$$

$$\frac{d\vartheta_n}{d\tau} = -1 \tag{5.11}$$

where ζ_n is the ponderomotive phase of the *n*-th electron, defined in (1.11). The evolution of the radiation field is governed by Maxwell's equations, which yield [5.4, 5.5]:

$$\frac{\partial \varepsilon}{\partial \tau} = i\, j_e \left\langle e^{-i\zeta_n} \right\rangle \tag{5.12}$$

for the evolution of the dimensionless optical field. The brackets denote an average over the ensemble of electrons. By combining (5.9) and (5.10), we arrive at the equation:

$$\frac{d^2\zeta_n}{d\tau^2} = \mathrm{Re}\left(i\,\varepsilon\, e^{i\zeta_n}\right) \tag{5.13}$$

This is the equation governing the behaviour of a simple pendulum in a gravitational field. It is therefore known as the *pendulum equation.*

5.3.2 Cavity de-tuning

The behaviour of each electron is found by numerically integrating the equations of motion (5.9), (5.10) and (5.11) together with the equation for the optical field (5.12). The sum of these solutions describes the behaviour of a bunch of electrons. Typically, the number of electrons in a bunch is on the order of $N_e \approx 10^8$. Due to limited computer time and memory, we cannot calculate the behaviour of each single electron. As a practical approach, the total charge in the bunch is divided over a limited number ($N_e \approx 1000$) of pseudo-electrons. Since this number does not compare to the actual number of electrons in an electron pulse, the result of the integration will be suffer from bad statistics. In particular, the initial distribution of electrons in the ponderomotive potential is not uniform but shows clusters of electrons at random positions. Due to the existence of these clusters, the spontaneous emission will be exaggerated. Brau [5.4] has solved this problem by introducing an artificial symmetry in the electron distribution, which causes the spontaneous emission to vanish.

In the present discussion, the electron pulse will be modelled as a square pulse. Since normal electron pulses are Gaussian-like and have relatively few electrons at the leading and rear edge, a square pulse will exaggerate the effects of slippage. No attempts were made to suppress the exaggerated spontaneous emission.

The equations of motion are thus integrated from $\tau = 0$ to $\tau = 1$, during which the radiation pulse slips a distance $\Delta\vartheta = 1$ over the electron pulse. The optical cavity is simulated by using the output of the first pass as input for the second pass. If the cavity is de-tuned a distance ΔL_c from exact synchronism, the optical field is shifted over a distance

$$\Delta\vartheta = -2\Delta L_c / L_s \tag{5.14}$$

The factor two accounts for the fact that a change in round-trip time equals twice the change in cavity length. The total number of passes is $N_{pass} = 10$. For the simulation an electron pulse length of $\Delta\vartheta = 1.5$, an energy spread $\Delta\mu = 1.25$ and a current density $j = 1$ were used.

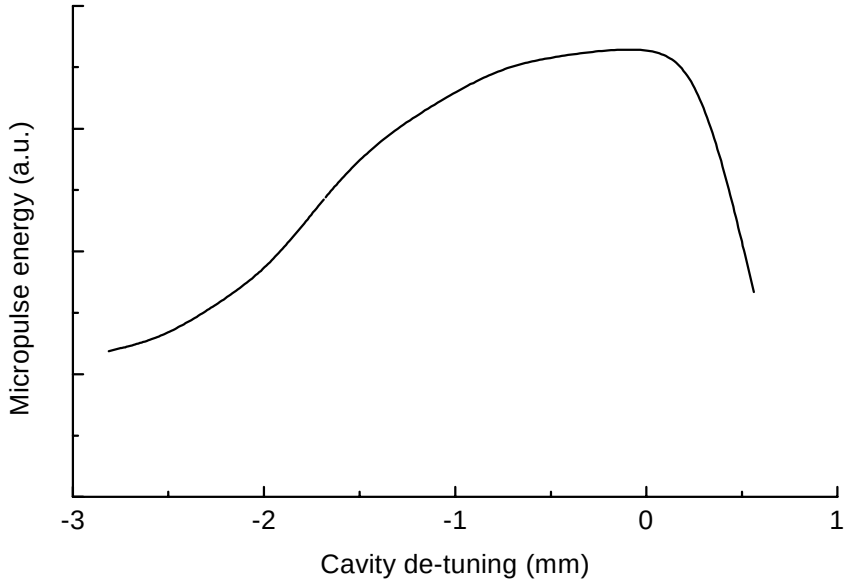

Figure 5.4: Calculation of the micropulse energy as a function of the cavity de-tuning length.

Figure 5.4 shows the result of this calculation. The desynchronism curve is clearly asymmetric, an effect that is attributed to laser lethargy. Because the centre of the radiation pulse is retarded, the FEL can be operated at a cavity length shorter than expected from (5.1). However, if the cavity length is chosen slightly longer than at exact synchronism, the radiation pulse arrives at the downstream mirror after the next electron pulse. The electrons ahead of the optical pulse are not yet bunched, and hence contribute near to nothing to the amplitude of the pulse. This means that the output power of the laser drops sharply as the cavity is de-tuned to longer lengths [5.4, 5.6].

The effect of the cavity de-tuning has been verified experimentally. Figure 5.5 shows the energy in the FEL macropulse as a function of the cavity de-tuning length. The qualitative agreement between the numerical simulation and the experiment is very

good. Note that for the higher current (I = 60 A) the maximum in the desynchronism curve is shifted to the shorter cavity lengths, with respect to the lower current (I = 30 A). For the higher current, the gain at the end of the wiggler is larger and consequently the rear part of the optical pulse is amplified more. The retardation of the optical pulse thus increases with increasing electron beam current, and the maximum of the desynchronism curve shifts to shorter cavity lengths.

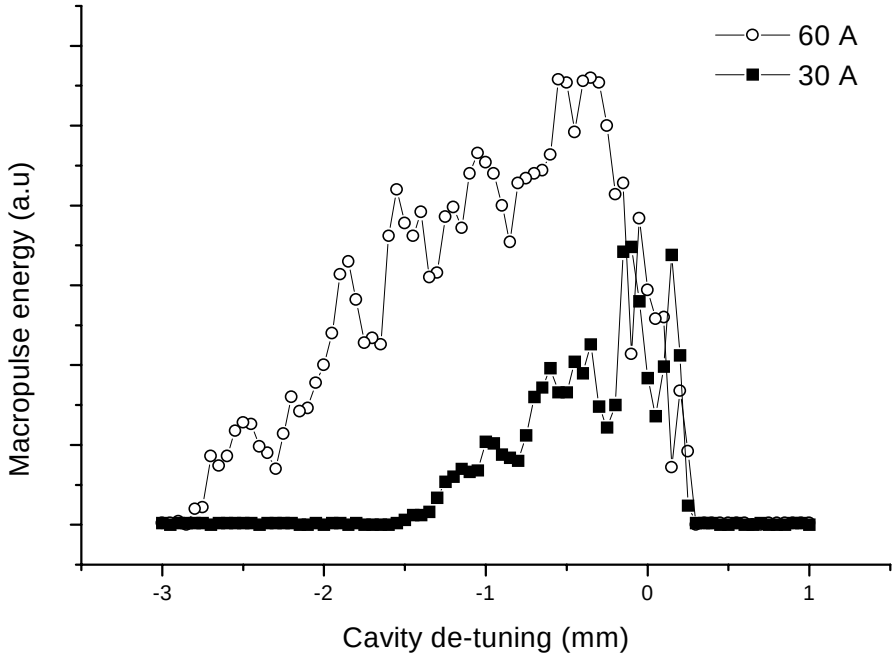

Figure 5.5: Experimental verification of the de-tuning curve.

5.4 Waveguide modes

In previous discussions in this thesis, the FEL interaction was considered to take place in an unbounded region, and the radiation was allowed to propagate freely in space. However, in our set-up the FEL radiation travels through a vacuum tube inside the wiggler. This vacuum tube acts as a waveguide for the radiation, which has implications for the mode structure of the laser beam. The mode structure in the waveguide will be determined by solving the homogeneous vector Helmholtz equations [5.7]:

$$\nabla^2 \vec{E} + k^2 \vec{E} = 0 \tag{5.15}$$

for the electric field $\vec{E}$ and

$$\nabla^2 \vec{H} + k^2 \vec{H} = 0 \tag{5.16}$$

for the magnetic field $\vec{H}$. Here k is the magnitude of the wave vector in free space. The electric field component consists of a transverse and a longitudinal part, each of which can be separated into transverse (x, y) and longitudinal z co-ordinates:

$$\begin{aligned}\vec{E}(x,y,z) &= \vec{E}_t(x,y,z) + \vec{E}_z(x,y,z) \\ &= \vec{e}(x,y)e^{-i\beta z} + \vec{e}_z(x,y)e^{-i\beta z}\end{aligned} \tag{5.17}$$

Here, the time-dependence of the electric field has been suppressed. By substituting this expression into the Helmholtz equation, we find for the longitudinal part:

$$\nabla_t^2 e_z + k_c^2 e_z = 0 \tag{5.18}$$

where ∇_t is the transverse part of the Laplacian and

$$k_c^2 = \beta^2 - k^2 \tag{5.19}$$

k_c is called the cut-off wave vector and it corresponds to a cut-off frequency ω_c. It is not possible for waves with frequencies below the cut-off frequency to propagate through the waveguide. There exist three classes of solutions for the equation (5.18):

1. Transverse electromagnetic modes (TEM) have $E_z = H_z = 0$.
2. Transverse electric modes (TE or H) have $E_z = 0$, but $H_z \neq 0$.
3. Transverse magnetic modes (TM or E) have $H_z = 0$, but $E_z \neq 0$.

TEM modes are not supported by a hollow waveguide. This is because in such a waveguide a transverse electric field can only exists if a time-varying axial magnetic field is present; and similarly a transverse magnetic field can only exist in the presence of a axial displacement current or an axial conduction current. Since the axial magnetic and electric field components are zero in a TEM mode, and there is no conductor in the centre of the waveguide that can support a conduction current, only the TM and TE modes can propagate in a hollow waveguide.

Let us first consider a TM mode in a circular waveguide. The radius of the waveguide is denoted by a and the waveguide wall is perfectly conducting, such that there are no transport losses. For convenience, equation (5.18) is written in cylindrical co-ordinates (r, ϕ):

$$\frac{\partial^2 e_z}{\partial r^2} + \frac{1}{r}\frac{\partial e_z}{\partial r} + \frac{1}{r^2}\frac{\partial^2 e_z}{\partial \phi^2} + k_c^2 e_z = 0 \tag{5.20}$$

Assuming that the solutions of this equation can be written as $e_z(r,\phi) = f(r)g(\phi)$, the equation is readily separated into r and ϕ, yielding:

$$\frac{d^2 f}{dr^2} + \frac{1}{r}\frac{df}{dr} + \left(k_c^2 - \frac{n^2}{r^2}\right) f = 0 \tag{5.21}$$

and

$$\frac{d^2 g}{d\phi^2} + n^2 g = 0 \tag{5.22}$$

Since the waveguide mode must be periodical in ϕ with period 2π, we must restrict the solutions to the integer values of *n*. Equation (5.21) is Bessel's differential equation. Its solutions are the *n*-th order Bessel functions $J_n(k_c r)$ and $Y_n(k_c r)$ of the first and second kind, respectively. Since $Y_n(k_c r)$ becomes infinite at $r = 0$, it is not a physically acceptable solution and thus only the Bessel functions of first order need to be considered. The complete solution of (5.20) is therefore:

$$e_z(r,\phi) = (A_1 \cos n\phi + A_2 \sin n\phi) J_n(k_c r) \tag{5.23}$$

Maxwell's equations require that the electric field at the waveguide boundary equals zero; this implies:

$$J_n(k_c r) = 0 \text{ at } r = a \tag{5.24}$$

This condition imposes restrictions on the value of k_c. If the roots of (5.24) are denoted by u_{nm}, the possible values for k_c are

$$k_{c,nm} = \frac{u_{nm}}{a} \tag{5.25}$$

There exists a doubly infinite number of waveguide modes (or eigenfunctions of (5.20)). Each mode TM_{nm} is characterised by the parameters *n* and *m*. The integer *n* refers to the azimuthal variations in the mode pattern, and the integer *m* refers to the radial variations. The propagation constant for the *nm*-th mode is found by substituting (5.25) in (5.19) and solving for β_{nm}:

$$\beta_{nm} = \left(k^2 - \frac{u_{nm}^2}{a^2}\right)^{1/2} \tag{5.26}$$

A similar discussion can be held for the derivation of the mode pattern of the TE modes. A proper solution for the axial magnetic field component is:

$$h_z(r,\phi) = (B_1 \cos n\phi + B_2 \sin \phi) J_n(k_c r) \tag{5.27}$$

In this case, Maxwell's equations demand that the spatial derivative of the magnetic field be zero at the waveguide wall:

$$\frac{dJ_n(k_c r)}{dr} = 0 \text{ at } r = a \tag{5.28}$$

The roots of (5.28) are denoted by u'_{nm}, so the eigenvalues of the TE_{nm} mode are given by:

$$k'_{c,nm} = \frac{u'_{nm}}{a} \tag{5.29}$$

When this is substituted into (5.19), the propagation constant of the TE_{nm} modes is found to be:

$$\beta'_{nm} = \left(k^2 - \frac{u'^2_{nm}}{a^2} \right)^{1/2} \tag{5.30}$$

The dominant mode is the mode with the lowest cut-off wave vector k_c, which is the mode with the lowest root u_{mn} or u'_{mn}. These roots are given in Table 5.1, from which it is readily seen that the dominant mode in a circular waveguide is the TE_{11} mode. Note that the roots for the TM_{11} and TE_{01} mode are identical, indicating that these modes are degenerate.

	TM			TE		
n	u_{n1}	u_{n2}	u_{n3}	u'_{n1}	u'_{n2}	u'_{n3}
0	2.405	5.520	8.654	3.832	7.016	10.174
1	3.832	7.016	10.174	1.841	5.331	8.536
2	5.135	8.417	11.620	3.054	6.706	9.970

Table 5.1: The values of the roots of the lowest order TE and TM modes in a circular waveguide.

5.4.1 Shift in the resonance wavelength

In Chapter 1, the FEL resonance condition was derived by demanding a constant ponderomotive phase for the electrons travelling through the wiggler. This condition is fulfilled when the electrons travel one wiggler period in the time that the FEL radiation travels one period plus a whole number of wavelengths. For the fundamental frequency this means:

$$\frac{\lambda_w}{v_z} = \frac{\lambda_w + \lambda}{v_{ph}} \tag{5.31}$$

where λ_w is the wiggler wavelength, λ the radiation wavelength, v_z the longitudinal electron velocity and v_{ph} the radiation phase velocity. In the plane-wave approximation, the phase velocity of the radiation wave is equal to the speed of light in the medium, which in this case is a vacuum. However, in a waveguide both the phase velocity and the group velocity depend on the mode pattern. The phase velocity is given by

$$v_{ph} = \frac{\omega}{\beta_{nm}} \tag{5.32}$$

and the group velocity is

$$v_{gr} = \left(\frac{d\beta_{nm}}{d\omega} \right)^{-1} \tag{5.33}$$

For the product of phase and group velocities the following relation holds (as can be seen by substituting either (5.30) or (5.26) in (5.32) and (5.33) and using the relation $\omega = ck$):

$$v_{gr} v_{ph} = \omega^2 \Big/ k^2 \tag{5.34}$$

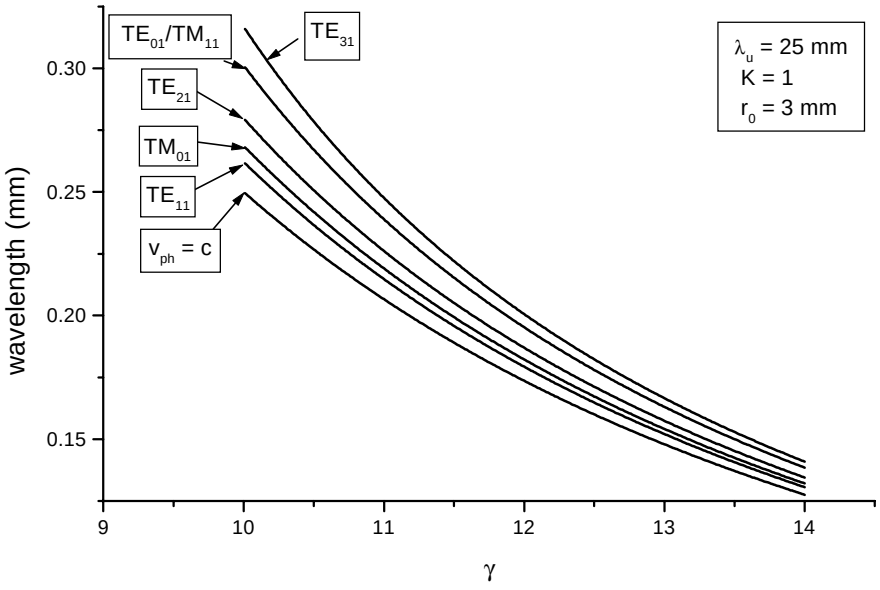

Figure 5.6: The FEL resonance condition as a function of the relativistic electron energy γ, for the lowest order TE and TM waveguide modes.

The group velocity in the waveguide is always less than the speed of light c, and consequently the phase velocity is always larger than c. The higher phase velocity in a waveguide leads to a longer FEL radiation wavelength than would be expected in the plane wave approximation. Higher order waveguide modes have longer wavelengths than lower-order ones. If, as in our case, the radiation is coupled out of the cavity by means of a central hole in the end mirror, the higher-order modes will dominate the mode pattern giving a large shift in the phase velocity and consequently in the wavelength.

This effect can be quite large, as is shown in Figure 5.6. Here, the FEL resonance wavelength is plotted as a function of the relativistic electron energy for a number of waveguide modes. The waveguide radius, wiggler parameter and wiggler wavelength were all chosen in accordance with the actual parameters in the TEU-FEL set-up.

5.4.2 Wavelength measurements

We have measured the wavelength spectrum of the FEL radiation with a Michelson interferometer. An example of such a measurement can be seen in Figure 5.7, where the intensity in arbitrary units has been plotted against the change in length δx of one arm of the interferometer. A Fourier analysis of this measurement is plotted in Figure 5.8.

In principle it is possible to calculate the resonance wavelength from a measurement of the optical cavity, which determines the group velocity according to (5.1). Then equation (5.34) yields the phase velocity of the dominant mode and the FEL resonance wavelength can be determined using the resonance condition (5.31). However, in our experimental set-up the length of the optical cavity is not only determined by the group velocity of the radiation, but also by the effect of slippage. Another complicating factor is the drastic change in mode pattern due to the outcoupling through a hole in the mirror. Especially the TE_{1m} and TM_{1m} modes will be affected by this hole, since these modes have a maximum intensity on axis. This means that each mode will have a pattern determined by a certain mixture of the unperturbed waveguide modes.

However, the *difference* in phase velocity between the various modes is influenced much less. The phase velocity difference leads to a wavelength difference that can be calculated and checked against the experimental value.

Consider for instance the four lowest order modes: TE_{11}, TM_{01}, TE_{01}/TM_{11} and TE_{31}. Assuming a radiation wavelength around 250 μm and an inner waveguide radius of a = 3 mm the propagation constant β and the phase velocity v_{ph} can be calculated using equations (5.30), (5.26) and (5.32).

This leads to the following values for $\Delta\beta/\beta$: -0.00021 between the TE_{11} and TM_{01} modes; -0.00031 between the TM_{01} and TE_{21} modes, -0.00047 between the TE_{21} and TE_{01}/TM_{11} modes and -0.00026 between the TE_{01}/TM_{11} and TE_{31} modes. Now from the FEL resonance condition (5.31) it follows for the wavelength difference between the modes: $\Delta\lambda$ = 5.3 μm, 7.8 μm, 11.8 μm and 6.5 μm. Comparing this result with the wavelength spectrum in Figure 5.8, the agreement is reasonably good.

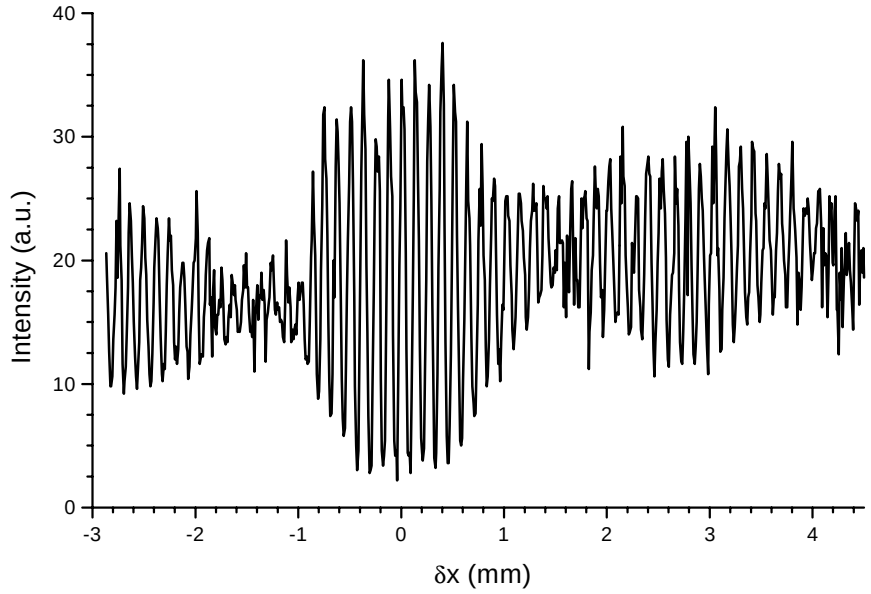

Figure 5.7: A typical scan made with our Michelson interferometer. δx stands for the change in length in one of the interferometer arms. For δx = 0 both arms have equal length.

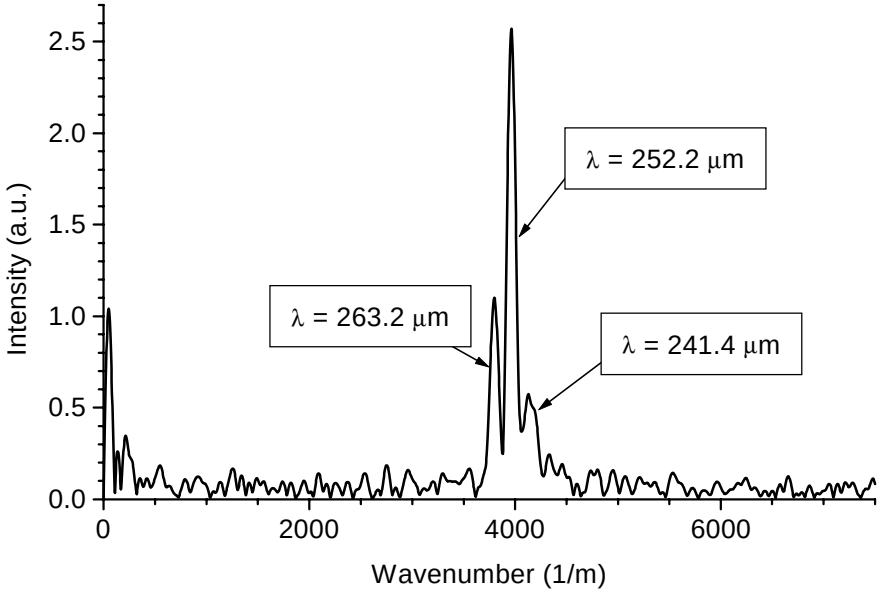

Figure 5.8: The wavelength spectrum of the FEL radiation, obtained by a Fourier transform of Figure 5.7.

5.5 Conclusions

We have demonstrated lasing in a Compton FEL at a wavelength of 250 μm. Lasing was confirmed by the energy spectrum of the electrons, which showed a marked broadening combined with a decrease in mean energy when the FEL output was measured. The output of the FEL can be varied by changing the length of the optical cavity. The desynchronism curve is asymmetric, an effect than is attributed to laser lethargy. This is confirmed by numerical integration of the dimensionless electron equations of motion.

We have found experimentally that in a Compton FEL the wavelength difference between transverse mode can be as large as 5 %, whereas in normal lasers this difference is of the order of 0.1 %. This can be explained by the fact that small changes in the phase velocity of the radiation, due to the transverse radiation profile in a waveguide, have a large influence on the resonance condition of an FEL and thus on the wavelength of the output radiation. This is especially important for high-quality electron beams, since these beams can be used in waveguide cavities with small diameters. We have found good agreement between the experimentally observed wavelength differences of successive modes and theoretical estimates.

5.6 References

5.1 G.J. Ernst, W.J. Witteman, J.W.J. Verschuur, R.F.X.A.M. Mols, B.M. van Oerle, A.F.M. Bouman, J.I.M. Botman, H.L. Hagedoorn, J.L. Delhez, W.J.G.M. Kleeven, "The TEU-FEL project", Infrared. Phys. Technol. **36**, 1 (1995) pp81 – 98.

5.2 J.W.J. Verschuur, G.J. Ernst, W.J. Witteman, "The TEU-FEL undulator", Nucl. Instr. and Meth. A **318** (1992) pp847 – 852.

5.3 G.J. Ernst, J.W.J. Verschuur, B.M. van Oerle, A.F.M. Bouman, J.I.M. Botman, H.L. Hagedoorn, W.J. Witteman, "First lasing of TEU-FEL", Nucl. Instr. and Meth. A. **375** (1996) pp26 – 27.

5.4 C.E. Brau, *Free-Electron Lasers*, Academic Press, Inc, San Diego (1990), ISBN 0-12-126000-3.

5.5 R. Bonifacio, F. Casagrande, G. Cerchioni, L. De Salvo Souza, P. Pierini, "One-dimensional theory of a free electron laser amplifier: steady state and superradiance", in *High gain, high power Free Electron Lasers*, Ed. R. Bonifacio, L. De Salvo Souza and C. Pellegrini, North Holland, Amsterdam (1989) ISBN 0-444-87395-3.

5.6 B.E. Newnam, R.W. Warren, R.L. Sheffield, J.C. Goldstein, C.A. Brau, "The Los Alamos Free Electron Laser oscillator: optical performance", Nucl. Instr. and Meth. A **237** (1985) pp187 – 198.

5.7 R.E. Collin, *Foundations for microwave engineering*, McGraw-Hill, New York (1966).

5.8 T.M. Apostol, *Calculus*, Vol. II, 2nd Ed., John Wiley & Sons, New York (1969) ISBN 0-471-00008-6.

5.9 J.W.J. Verschuur, G.J. Ernst, B.M. van Oerle, D. Bisero, “The effect of transverse modes in a wave-guide resonator on the resonance condition of a Compton FEL”, Opt. Comm. **133** (1997) pp229 – 233.

List of Publications

This thesis is based on the following publications:

1. B.M. van Oerle and G.J. Ernst, "On the use of CsK_2Sb photo cathodes in RF linacs", Nucl. Instr. and Meth. A. **358** (1995) pp287–290.
2. G.J. Ernst, W.J. Witteman, J.W.J.Verschuur, R.F.X.A.M. Mols, B.M. van Oerle, A.F.M. Bouman, J.I.M. Botman, H.L. Hagedoorn, J.L. Delhez and W.J.G.M. Kleeven, "The TEU-FEL project", Infrared Phys. Technol. **36**, 1 (1995) pp81–98.
3. B.M. van Oerle and G.J. Ernst, "Autocorrelation measurements of bursts of picosecond pulses", Appl. Opt. **35,** 25 (1996) pp5177–5179.
4. G.J. Ernst, J.W.J. Verschuur, B.M. van Oerle, A.F.M. Bouman, J.I.M. Botman, H.L. Hagedoorn, W.J. Witteman, "First lasing at TEU-FEL", Nucl. Instr. and Meth. A **375** (1996) pp26–27.
5. D. Bisero, B.M. van Oerle, G.J. Ernst, J.W.J. Verschuur and W.J. Witteman, "Photoemission from K-Te photocathodes", Appl. Phys. Lett. **69**, 25 (1996) pp3641 – 3643.
6. B.M. van Oerle, D. Bisero, G.J. Ernst, J.W.J. Verschuur and W.J. Witteman, "High efficient harmonic generation in two BBO crystals by means of walk-off compensation", Proc. IEEE/LEOS Symp. Benelux Chapter, (1996) pp25 – 27.
7. J.W.J. Verschuur, G.J. Ernst, B.M. van Oerle, D. Bisero; "The effect of transverse modes in a wave-guide resonator on the resonance condition of a Compton FEL", Opt. Comm **133**, 1 – 6 (1997) pp229 – 233.
8. D. Bisero, B.M. van Oerle, G.J. Ernst, J.W.J. Verschuur and W.J. Witteman, "High efficient photo-emission from Cs-K-Te", Appl. Phys. Lett. **70,** 12 (1997) pp1491 – 1493
9. W.J. Witteman, G.J. Ernst, J.W.J. Verschuur, B.M. van Oerle, D. Bisero, "Free electron laser with high brightness photo-injector", Laser Physics **7**, 1 (1997) pp150 – 154.
10. B.M. van Oerle, D. Bisero, G.J. Ernst, J.W.J. Verschuur and W.J. Witteman, "A Nd: YLF laser system for the illumination of Cs_2Te photo cathodes in the TEU-FEL accelerator", accepted for publication in Nucl. Instr. and Meth. A.
11. J.W.J. Verschuur, G.J.Ernst, B.M. van Oerle, D. Bisero, A.F.M. Bouman, W.J. Witteman; "Lasing experiments at TEU-FEL", accepted for publication in Nucl. Instr. and Meth. A.
12. D. Bisero, B.M. van Oerle, G.J. Ernst, J.W.J. Verschuur and W.J. Witteman, "K-Te photocathodes", accepted for publication in J. Appl. Phys.
13. B.M. van Oerle, D. Bisero, G.J. Ernst, J.W.J. Verschuur, W.J. Witteman, "Optimization of the power and control of the shape of amplified trains of laser pulses", accepted for publication in Appl. Opt.

Summary

In a free electron laser, coherent radiation is generated by letting an electron beam propagate through an alternating magnetic field. The magnetic field is created by a linear array of magnets, which is called an undulator or a wiggler. The wavelength of the laser radiation depends on the amplitude and wavelength of the magnetic field, and on the energy of the electrons. For a short-wavelength or high-power free electron laser, an electron beam with a low beam divergence, low energy spread and a high peak current is required. At the present time, the only way to generate such an electron beam is by means of a photoinjector. In such a device, an electron beam is created by illuminating a photo cathode with intense pulses of light from a drive laser system. The electron bunches that are emitted from the photoemissive material are accelerated in a radio-frequency linear accelerator.

TEU-FEL is a free electron laser operated by the Nederlands Centrum voor Laser Research in close collaboration with the University of Twente. The electron beam in TE-FEL is generated in a photoinjector. This set-up is the subject of this thesis.

One of the most critical components of a photoinjector is the drive laser system which illuminates the photo cathode. The Nd:YLF system that is used at TEU-FEL is described in Chapter 2. It emits trains of laser pulses, called macropulses, that consist of up to 1200 micropulses. The repetition rate of the macropulses is 10 Hz, the micropulses repeat at a frequency of 81.25 MHz. The research focused on the stability of the system output power during a macropulse. A feed forward loop was constructed that can optimise and stabilise the shape of the output macropulse within 1 %.

Most photo cathode materials are not sensitive to the fundamental of Nd:YLF (1053 nm). It is therefore necessary to generate the second or fourth harmonic of the Nd:YLF laser. A walk-off compensated frequency quadrupling scheme has been designed, which yields an energy conversion efficiency of 25 % from the fundamental to the fourth harmonic. The duration of the infrared and visible micropulses has been measured with autocorrelation techniques and with a streak camera.

Chapter 3 treats several aspects of photo cathode materials. A photo cathode material is characterised by its quantum efficiency (QE) which is defined as the number of emitted electrons per incident photon. Several photo cathode materials have been used in the linear accelerator, most notably alkali-antimony and alkali-tellurium compounds. The former are mainly sensitive to visible radiation and have a typical QE ≈ 1 %; the latter are sensitive in the ultraviolet region of the spectrum and have a typical QE ≈ 10 %. Two previously unknown photoemissive materials have been discovered. These materials are compounds of potassium and tellurium, and of cesium, potassium and tellurium. The latter shows a QE = 23.4 % in the ultraviolet region of the spectrum.

Due to pollution and outgassing of alkali-metals, the QE of photo cathodes steadily decreases when they are used in the linear accelerator. It was found that the alkali-

telluride-compounds have significantly larger lifetimes under operating conditions than their alkali-antimonide counterparts.

The quality of the electron beam can be characterised by the emittance, which is a measure for the angular spread of the electrons. The lower the emittance, the better the quality of the beam. Several methods exist to measure this beam quality number. In Chapter 4, a comparison is made between the quadrupole scan, the pepper pot technique and phase space tomography.

The longitudinal phase space of the electron beam is characterised by means of streak camera measurements and longitudinal phase space tomography. It is demonstrated that the duration of the electron bunch depends on the bunch charge. At a charge of 1.5 nC the bunch length is 38 ps and the energy spread is 0.4 %. These measurements are combined with the emittance measurements to yield a value for the brightness of the electron beam. A comparison of the brightness with that obtained with other accelerators shows that the electron beam that is used in the TEU-FEL experiment is one of the brightest beams in the world.

In Chapter 5, lasing of TEU-FEL is demonstrated by simultaneously measuring the electron energy spectrum and the free electron laser output power. An increase in output energy is accompanied by a decrease in mean electron energy and a profound increase in energy spread. This indicates a energy transfer from the electron beam to the laser beam, thus confirming laser operation.

The effect of de-tuning the free electron laser cavity has been investigated; the desynchronism curve is seen to be asymmetric, a result that is in agreement with that found by other workers in the field. Finally, the wavelength spectrum of the free electron laser is measured by making a Fourier transform of the results of a Michelson interferometer scan. The spectrum shows three prominent peaks (see cover) spaced approximately 9 μm apart. The occurrence of these different wavelengths is attributed to the difference in phase velocity between the modes in the resonator waveguide. There is good agreement with the theoretically predicted wavelength difference.

Samenvatting

In een vrije-elektronen laser wordt coherente straling gegenereerd door een bundel elektronen in een wisselend magnetisch veld te laten bewegen. Het magnetisch veld wordt gemaakt in een zgn. undulator of wiggler, die bestaat uit een rij magneten. De golflengte van de laserstraling hangt af van de amplitude en de golflengte van het magnetisch veld, alsmede van de energie van de elektronen. Voor de constructie van een kortgolvige of hoogvermogen vrije elektronen laser is een elektronenbundel met een lage bundeldivergentie, lage energiespreiding en hoge piekstroom vereist. In de huidige stand van de techniek kan een zo'n bundel alleen gemaakt worden met behulp van een fotoinjector. In een dergelijk apparaat wordt een elektronenbundel vrijgemaakt uit een fotokathode door deze te belichten met intense lichtpulsen uit een aandrijflaser. De elektronenbundel wordt vervolgens versneld in een radio-frekwente lineaire versneller.

TEU-FEL is een vrije-elektronenlaser gebouwd door het Nederlands Centrum voor Laser Research in samenwerking met de Universiteit Twente. De elektronenbundel in TEU-FEL wordt gemaakt met een fotoinjector. Deze opstelling is het onderwerp van dit proefschrift.

Een van de meest kritische onderdelen van een fotoinjector is de aandrijflaser waarmee de fotokathode belicht wordt. Het Nd:YLF systeem dat bij TEU-FEL gebruikt wordt staat beschreven in Hoofdstuk 2. Het systeem genereert treintjes van laserpulsen, die macropulsen genoemd worden. Zo'n treintje bestaat uit maximaal 1200 micropulsen. De herhalingsfrekwentie van de macropulsen is maximaal 10 Hz, die van de micropulsen bedraagt 81.25 MHz. Het onderzoek richtte zich voornamelijk op de stabiliteit van de micropuls energie gedurende de macropuls. Er is een systeem gebouwd dat de energie van de uitkomende macropuls optimaliseert en de vorm stabiliseert.

De meeste fotokathodematerialen zijn niet gevoelig voor de fundamentele golflengte van Nd:YLF (1053 nm). Het is daarom noodzakelijk om the tweede of vierde harmonische van de Nd:YLF laser te genereren. Hiervoor is een walk-off-gecompenseerde frequentie-verviervoudiger gebouwd. Deze verviervoudiger converteert de energie van de fundamentele golflengte naar de vierde harmonische met een efficiency van 25 %. De lengte van de infrarode en zichtbare micropulsen is gemeten met behulp van autocorrelatietechnieken en een streak camera.

In Hoofdstuk 3 worden verschillende aspecten van fotokathodematerialen behandeld. Een fotokathodemateriaal wordt gekarakteriseerd door zijn quantum efficientie (QE). Dit getal is gedefinieerd als de hoeveelheid geëmitteerde elektronen per invallend foton. Verschillende fotokathodematerialen zijn in de lineaire versneller gebruikt, waaronder alkali-antimoniden en alkali-telluriden. De eerste klasse is voornamelijk gevoelig voor straling in het zichtbare deel van het spectrum en heeft typisch een QE $\approx$ 1 %. De alkali-telluriden zijn gevoelig voor ultraviolette straling en hebben

typisch een QE ≈ 10 %. De eigenschappen van twee nieuwe fotokathodematerialen zijn onderzocht; het gaat hier om een verbinding van kalium en tellurium en een verbinding van cesium, kalium en tellurium. De laatste heeft een QE = 23.4 % in het ultraviolette deel van het spectrum.

Ten gevolge van vervuiling van de fotoaktieve laag, en als gevolg van verdamping van de alkalimetalen uit de laag, neem de QE van de fotokathodes langzaam af wanneer ze gebruikt worden in de lineaire versneller. Uit het onderzoek blijkt dat de levensduur van de op tellurium gebaseerde kathodes onder werkomstandigheden significant langer is dan die van de op antimoon gebaseerde kathodes.

De kwaliteit van de elektronenbundel wordt uitgedrukt in de emittantie, een getal dat een maat is voor de hoekspreiding van de elektronen. Hoe lager de emittantie, hoe beter de kwaliteit van de elektronenbundel. Er bestaan verschillende methoden om de emittantie te meten. In Hoofdstuk 4 worden de quadrupool scan, de peperpotmethode en faseruimtetomografie uitgelegd en met elkaar vergeleken.

De longitudinale faseruimte van de elektronenbundel is bekeken met behulp van een streak camera en longitudinale faseruimtetomografie. Uit de metingen blijkt dat de duur van de elektronenpuls afhangt van de lading in de puls. Bij een lading van 1.5 nC is de pulsduur 38 ps en de energiespreiding 0.4 %. Deze metingen zijn gecombineerd met de emittantiemetingen om een waarde te vinden voor de helderheid van de elektronenbundel. Een vergelijking van deze helderheid met waarden die bereikt zijn met andere versnellers laat zien dat deze elektronenbundel één van de helderste ter wereld genoemd mag worden.

In Hoofdstuk 5 wordt de werking van TEU-FEL aangetoond door gelijktijdig het energiespectrum van de elektronenbundel en de vrije-elektronen laser energie te meten. Wanneer het uitgangsenergie van de laser toeneemt, wordt de gemiddelde elektronenergie lager en vindt er een substantiele vergroting van de energiespreiding plaats. Dit geeft aan dat er energie overgedragen wordt van de elektronenbundel naar de laserbundel, hetgeen de werking van de laser bevestigt.

Het uitgangssvermogen van de vrije elektronen laser hangt af van de lengte van de resonator. De curve die dit effect beschrijft is asymmetrisch, een resultaat dat ook door andere experimentatoren gevonden is. Tenslotte is het golflengtespectrum van de vrije-eletronen laser bepaald door een Fourier transformatie toe te passen op de resultaten van een Michelson interferometer scan. Het spectrum laat drie duidelijke pieken zien (zie omslag), die ongeveer 9 μm van elkaar verwijderd zijn. De oorsprong van deze drie golflengten moet gezocht worden in de verschillen in fasesnelheid tussen de verschillende modi in de golfpijpresonator. De gemeten verschillen in golflengte stemmen goed overeen met de theoretische voorspelling.

Nawoord

Bij het tot stand brengen van een proefschrift is een groot aantal mensen (voor en achter de schermen) betrokken, zonder wie het betreffende onderzoek nooit begonnen, voortgezet of afgerond had kunnen worden. Ik wil, in de stellige overtuiging dat ik een aantal mensen ga vergeten, de bijdrage van enkele personen benadrukken.

Allereerst wil ik mijn promotor prof. dr. W.J. Witteman en mijn begeleider dr. G.J. Ernst bedanken. Zij maakten het voor mij mogelijk om te promoveren en maakten mij wegwijs in de vrije-elektronenlasergemeenschap. Bijzondere dank ook voor de rest van het TEU-FEL team: voor Jeroen Verschuur die tegen de groeiende werkdruk in tijd vond om mijn proefschrift door te lezen; voor Twan Bouman die uit het puin van de Quantel-versterkers nog iets moois wist op te bouwen; e per Diego Bisero che, dopo abitare in Olanda per un anno sa pronunciare senza problemi la parola “fotokathode-preparatiekamer”.

Gerard Oude Meijers en Henk Prins introduceerden mij in de wonderbaarlijk schone wereld van het ultra-hoog vacuum. Een speciale pluim ook voor Henk Tanke, die met een halve, vage en krakkemikkige bouwtekening nog de fraaiste resultaten weet te frezen. Ab Nieuwenhuis, Roy Lammerink en Jacob Couperus droegen zorg voor de elektronica: als ware elektronentemmers dwongen zij deze kleine rakkers in de juiste banen.

Binnen en buiten werktijd heb ik veel steun (grotensdeels in de vorm van opbouwende kritiek) gehad aan Bert, Frans, Hako, Louw en Herman. Ook de overige leden van de vakgroep QE en het NCLR bedank ik voor vrolijke sportdagen, uitjes, conferenties en wat dies meer zij.

Ook wil ik alle vrienden in en buiten Enschede hartelijk bedanken. Zij wisten de fakkel van het doorzettingsvermogen brandende te houden middels regelmatig terugkerende kampeerfestijnen. In het bijzonder de MPW: Frank, Wim, Henk en Henriëtte, met wie het onderhand een sport geworden is om vakantiehuisjes in onbewoonbare boeren-gehuchten nét buiten het bereik van het openbaar vervoer te vinden.

Tenslotte, omdat zij nooit getwijfeld hebben aan mij en het resultaat van mijn promotie-onderzoek: mijn moeder Bep en mijn broers Hans en Gerard. Allen hartelijk dank.

Bart van Oerle

Curriculum Vitæ

De auteur van dit proefschrift werd geboren in het Bonifaciusziekenhuis in Leeuwarden op 22 september 1969 als de derde zoon van Bart van Oerle en Bep van Oerle - Reumer. Het gezin verhuisde in 1979 naar Zwolle, waar hij de middelbare school volgde (ongedeeld Atheneum) aan de Rijksscholengemeenschap. De diploma-uitreiking vondt plaats op 4 juni 1987.

In 1987 verhuisde hij weer terug naar het Hoge Noorden, ditmaal naar Groningen waar hij begon met een studie Experimentele Natuurkunde aan de universiteit aldaar. De verleidingen van het studentenleven waren veel, en de studiebeurzen naar hedendaagse maatstaven ruim, maar na zes jaar lukte het hem toch om af te studeren in vakgroep Chemische Fysica. De titel van zijn doctoraalscriptie, die beoordeeld werd door prof. dr. H.A. Ferwerda, was “Phase-locking of femtosecond pulse pairs”. Het doctoraal-examen werd met goed gevolg afgelegd op 24 juni 1993.

Na zijn afstuderen trad hij in dienst van het Nederlands Centrum voor Laser Research in Enschede waar hij kwam te werken aan het TEU-FEL project onder leiding van prof. dr. ir. W.J. Witteman. Het onderzoek wat hij daar verrichtte is het onderwerp van dit proefschrift.